

Mohamed Khider University of Biskra

Faculty of exact sciences
Department of Matter Sciences

MASTER MEMORY

Field : Matter Sciences Sector: Chemistry Specialty: Materials Chemistry

Réf.:

Presented by: SOUDANI Selsabil

THE:02/06/2025

Influence of doping on the structural properties of a BNT-type ceramics

Jury:

Mr Abdelhek MEKLID MCA University of Biskra Chairman
Mrs Nadia NEBBACHE Prof University of Biskra Examiner

AcademicYear: 2024/2025

Acknowledgements

Praise be to Allah who prepared the beginning and facilitated the end. Praise be to Allah who drowned me in pleasure and made my path easy to complete this humble work.

All this work was done in the chemistry laboratory of the Department of Matter Sciences at the University of Biskra.

All thanks and gratitude to my honourable supervisor Mr. Abdelhek Meklid, who never spared us with his advice and guidance, and his constant keenness to motivate us, he was a role model and support with all his knowledge and experience, we will not forget your precious guidance and all thanks and appreciation for what you gave us.

I would also like to express my respectful thanks to the members of the jury: Mr. Mahmoud Omari and Mrs. Nadia Nebbache for the honor they have done us by agreeing to judge this work.

I would also like to thank all the Chemistry Laboratory Engineers in our Department for the material help and means they made available to us, to carry out this research work.

I would like to mention Mrs. Hayet Benmachiche, Head of Laboratory, Mrs. Nadia Bouzize, Mrs. Soumia Khelifa, for everything they have done for me.

I also owe a debt of gratitude to all my chemistry teachers, especially Mrs Afaf Zekri for her kind words and encouragement, as well as Mrs Faiza Lehraki, Mr Aissam Boukraa, Mrs Zelikha Necira for all their help, all thanks and gratitude.

All the love and thanks to those who helped me in the realisation of this memorandum, Ahlem Ksouri, Chaima BenBrika and Achoak Achour.

Finally, I would like to warmly thank my friends and colleagues who have always helped and encouraged me, and everyone who has helped me to realise this memorandum even with an idea.

My sincere thanks.

Selsabil Soudani

اهداء

اهدي رسالتي الى من حاكت سعادتي بخيوط منسوجة من قلبها، من ابصرت بها طريق حياتي، واستمديت منها قوتى واعتزازي بذاتى، الى القلب الذي قوتى واعتزازي بذاتى، الى القلب الذي

ينبض حبا لا يعرف شروطا، الى من تعبت لارتاح وسهرت لأحلم وضحت لأحقق، انت البداية وانت الدافع وانت النور في كل ظلام

اليك امى اهدى رسالتي وكل انجازي وكل حرف كتبته وكل جهدى وتعبى وكل خطوة خطوتها نحو النور

اهدي رسالتي الى من زرع في قلبي القوة وفي عقلي الحكمة الى من كان صمته دعما ونظرته طمأنينة

اليك ابى اهدي كل خطوة اخطوها اليوم على الطريق الذي عبدته لى يتعبك وصبرك

الى الرجل الذي لم تنحن قامته الا ليعلمني الوقوف الى من كان حضوره امانا وغيابه فراغا لا يملا...

والداى دمتما نورا في قلبي ما حييت

اهدي رسالتي الى الأمان والسند، الى النور في لحظات العتمة، الى زهرات عمري، الى الداعمات، المشجعات والحاضنات لكل احلامي، وأجمل الهدايا التي وهبني الله إياها...

الى التي وجودهن في حياتي نعمة لا تقدر بثمن، أغلى ما املك اختاي سهام وسامية

اهدي رسالتي الى من كان ظهري وقت الشدة، وابتسامتي وقت الحزن، الى من شاركني التفاصيل الصغيرة ووقف بجانبي في اللحظات الكبيرة...

اليك اخي الوحيد وحيد اهدي هذا العمل تعبيرا عن امتناني كونك قطعة من قلبي دمت لي عونا وامانا لا يزول

اليك عائلتي، تتلاشى الكلمات وتعجز الحروف عن احتواء محبتي وامتناني

اليك عائلتي اهدى رسالتي وعمرى بكم أزهر ومعكم اطمئن

اهدي رسالتي الى من كانت لي اختا لم تلدها امي، الى من لم تبخل علي يوما بنصيحة ولا ترددت في دعمي بكل ما تملك الدي رسالتي اليك يا صاحبة القلب الكبير والعقل الناضج، والروح النقية صديقة العمر ضحى قوبع.

سلسبيل سوداني

Abstract

The main objective of this work is to synthesise and characterise the structural, physical and photocatalytic properties of a new type of BNT ceramic with an ABO₃ perovskite structure in the system:

$$(Na_{0.5} Bi_{0.5})_{1-x} Sm_x (Ti_{0.8} Zr_{0.2})_{0.9} (Fe_{1/5} Zn_{1/5} In_{3/5})_{0.1}$$
, where x=0, 2%.

We sought to optimise the structural, morphological and optical properties of this material to improve its photocatalytic activity. The study was carried out using a substitution procedure at sites A and B, where the various catalysts were prepared by the molten salt method and then calcined at 900°C. Their characterisation was carried out using various techniques: X-ray diffraction (XRD), Fourier transform infrared spectroscopy (FTIR), Scanning electron microscopy (SEM) and UV-visible spectroscopy.

Structural analyses (XRD, FTIR) confirmed the formation of a tetragonal perovskite structure with space group P_{4bm} for all compositions, SEM analysis shows that the grain size 2.87 µm with a uniform distribution. UV-visible absorption measurements were used to determine the energy gaps (Eg) of the different samples (samarium undoped BNT (Sm) Eg = 2.22eV, samarium doped BNT (BNT X = 2%) Eg = 2.14eV).

Photocatalytic tests, carried out on the degradation of methylene blue under solar irradiation, showed a maximum degradation efficiency of 63.44% after 180 min. The reaction kinetics followed a pseudo-first-order model, with a maximum apparent rate constant (k_{app}) of 0.00535 min⁻¹ for the BNT X= 2% catalyst, indicating superior photocatalytic activity.

The samples were sintered at 1000, 1050, 1100 and 1150 °C, respectively, to optimise the sintering temperature at which the sample density is maximised.

These results indicate that this material may be a promising candidate for the degradation of organic pollutants in aqueous solution.

Key words: Perovskite, BNT, molten salts, catalysts, XRD, FTIR, SEM.

Résumé

L'objectif principal de ce travail est de la synthèse et la caractérisation des propriétés structurelles, physiques et photocatalytiques d'un nouveau céramique type BNT avec une structure de pérovskite ABO₃ dans le système :

$$(Na_{0.5} Bi_{0.5})_{1-x} Sm_x (Ti_{0.8} Zr_{0.2})_{0.9} (Fe_{1/5} Zn_{1/5} In_{3/5})_{0.1}, où x=0, 2\%.$$

Nous avons cherché à optimiser les propriétés structurelles, morphologiques et optiques de ce matériau pour améliorer son activité photocatalytique. L'étude a été réalisée par une procédure de substitution sur les sites A et B, où les différents catalyseurs ont été préparés par la méthode des sels fondus puis calcinés à 900 °C. Leur caractérisation a été réalisée à l'aide de différentes techniques : Diffraction des rayons X (DRX), Spectroscopie infrarouge à transformée de Fourier (IRTF), Microscopie électronique à balayage (MEB) et Spectroscopie UV-visible.

Les analyses structurales (DRX, IRTF) ont confirmé la formation d'une structure pérovskite tétragonale avec le groupe d'espace P_{4bm} pour toutes les compositions, l'analyse par MEB montre que la taille des grains 2.87 μm avec une distribution uniforme. Des mesures d'absorption UV-visible ont été utilisées pour déterminer les gaps énergétiques (Eg) des différents échantillons (BNT non dopée par samarium (Sm) Eg = 2.22eV, BNT dopée par samarium (BNT X= 2%) Eg = 2.14eV).

Les tests photocatalytiques, réalisés sur la dégradation du bleu de méthylène sous irradiation solaire, ont montré une efficacité de dégradation maximale de 63.44% après 180 min, la cinétique de la réaction a suivi un modèle de pseudo-premier ordre, avec une constante de vitesse apparente maximale (k_{app}) de 0.00535 min⁻¹ pour le catalyseur BNT X= 2%, ce qui indique une activité photocatalytique supérieure.

Les échantillons ont été frittés à 1000, 1050, 1100 et 1150 °C, respectivement, afin d'optimiser la température de frittage à laquelle la densité de l'échantillon est maximale.

Ces résultats indiquent que ce matériau peut être un candidat prometteur pour la dégradation des polluants organiques en solution aqueuse.

Mots-clés: Pérovskite, BNT, sels fondus, catalyseurs, DRX, IRTF, MEB.

الملخص

الهدف الرئيسي من هذا العمل هو تركيب وتوصيف الخصائص الهيكلية والفيزيائية والتحفيزية الضوئية لنوع جديد من سير اميك BNT مع بنية بيروفسكايت ABO₃ في النظام:

.x=0 ,0.02 جيث Na_{0.5} Bi_{0.5})_{1-x} Sm_x (Ti_{0.8} Zr_{0.2})_{0.9} (Fe_{1/5}Zn_{1/5} In_{3/5})_{0.1}

سعينا إلى تحسين الخصائص الهيكلية والمور فولوجية والبصرية لهذه المادة لتحسين نشاطها التحفيزي الضوئي. أُجريت الدراسة باستخدام إجراء استبدال في الموقعين A و B، حيث تم تحضير المحفزات المختلفة بطريقة الأملاح المنصهرة ثم تم تكليسها عند درجة حرارة 900 درجة مئوية. وقد تم إجراء توصيفها باستخدام تقنيات مختلفة: حيود الأشعة السينية (XRD)، والتحليل الطيفي بالأشعة تحت الحمراء المحولة فورييه (FTIR)، والفحص المجهري الإلكتروني الماسح (SEM)، والتحليل الطيفي بالأشعة فوق البنفسجية المرئية.

أكدت التحليلات الهيكلية (FTIR ، XRD) تكوين بنية بيروفسكايت رباعي الزوايا مع المجموعة الفضائية P_{4bm} لجميع التركيبات، ويُظهر تحليل SEM حجم الحبيبات 2.87 ميكرومتر مع توزيع منتظم. استُخدمت قياسات الامتصاص بالأشعة فوق البنفسجية المرئية لتحديد فجوات الطاقة (Eg = 2.22eV غير المطعم بالسماريوم BNT المطعمة بالسماريوم $E_{200} = 2.14eV$).

أظهرت اختبارات التحفيز الضوئي، التي أجريت على تحلل الميثيلين الأزرق تحت الإشعاع الشمسي، كفاءة تحلل قصوى بلغت 63.44 بعد 63.44 دقيقة، اتبعت حركية التفاعل نموذج الترتيب الأول الزائف، مع الحد الأقصى لثابت المعدل الظاهري البالغ 63.44 البالغ 63.00535 دقيقة للمحفز 63.44 المحفز 63.44 مما يشير إلى نشاط تحفيز ضوئي فائق.

تم تلبيد العينات عند 1000 و1050 و1100 و1150 درجة مئوية على التوالي لتحسين درجة حرارة التلبيد التي تصل عندها كثافة العينة إلى الحد الأقصى.

تشير هذه النتائج إلى أن هذه المادة قد تكون مرشحًا واعدًا لتدهور الملوثات العضوية في المحلول المائي.

الكلمات الرئيسية: البيروفسكايت، BNT، الاملاح المنصهرة، المحفزات، حيود الأشعة السينية، والتحليل الطيفي بالأشعة تحت الحمراء المحولة فورييه، والفحص المجهري الإلكتروني الماسح.



Contents

Figures List	
Tables List	
General Introduction	01
Bibliographic References	03
Chapter I: BIBLIOGRAPHY	
I.1 Introduction	04
I.2 General Information on ceramics	04
I.2.1 Classification of ceramic	05
I.3 Perovskite structure	06
I.3. 1 Crystalline structure	07
I.3. 2 Ideal perovskite structure	07
I.3. 3 Complex perovskite structure	07
I.3. 4 Stability of the structure	07
I.3. 4 .1 Tolerance factor	08
I.3. 4.2 Stoichiometric condition	09
I.3. 4 .3 Electroneutrality condition	09
I. 4 Properties of perovskites	09
I. 4.1 Electrical properties	09

I. 4.1.1 Piezoelectricity	09
I. 4.1.1.1 Symmetry and piezoelectricity	11
I. 4.1.2 Pyroelectricity	13
I. 4.1.3 Ferroelectricity	13
I. 4.1.3.1 Ferroelectric domains	14
I. 4.1.3.2 The Curie point	15
I. 4.1.4 Dielectricity	16
I. 4.2 Photocatalytic properties	17
I. 4.3 Catalytic properties	17
I. 5 Generalities on BNT perovskite-type oxide	17
I. 5.1 History	17
I. 5.2 The BNT-type structure	18
I. 5.3 The dielectric and ferroelectric properties of BNT	18
I. 5.4 Advantages and disadvantages of BNT	19
I. 6 Perovskite doping	19
I. 6. 1 Definition of doping	19
I. 6. 2 Doping purposes	20
I. 6. 3 Doping techniques	20
I. 6. 3.1 Ion implantation doping	20
I. 6. 3.2 Diffusion doping	20
I. 6. 3.3 Doping by laser technique	20
I. 6. 3.4 Doping by epitaxy	21
I. 6. 4 Classification of doping agents	21
Bibliographic References	23

Chapiter II: EXPERIMENTAL TECHNIQUES

II .1 Introduction	27
II .2 The Molten Salt method	28
II .2.1 The advantages of the molten salt synthesis MSS	28
II .2.2 The important purpose of using molten salts synthesis	30
II .2.3 The role of molten salts	30
II .3 Experimental procedure	30
II.3.1 Starting products	30
II.3.1.1 Base oxides	31
II.3.1.2 Dopants	33
II.3.1.2.1 Doping at site A	34
II.3.1.2.2 Dopings at site B	34
II.3.2 Powder preparation	36
II .3.2.1 Weighing and mixing	36
II.3.2.2 Grinding with salts	36
II.3.2.3 Heat treatment	38
II .3.2.4 Grinding and drying procedure of pellets	40
II.3.2.5 Salt washing	40
II.3.2.6 drying	41
II.3.2.7 Regrinding	42
II.3.2.8 Shaping	42
II.3.2.9 Sintering	43
II.4 Structural characterisation techniques for calcined powders and sintered	45
ceramics	

II.4.1 Study of the structure by X-ray diffraction	45
II.4.2 Measurement of density (d)	47
II.4.3 Measurement of porosity (P)	48
II.4.4 SEM analysis	49
II.4.5 FTIR analysis	50
II.5 Photocatalysis	52
II.5 .1 Introduction	52
II.5 .2 Dyes	52
II.5 .2 .1 Definition of a dye	52
II.5 .2 .2 Classification of dyes	53
II.5 .3 Photocatalysis	53
II.5 .3.1 Definition of photocatalysis	53
II.5 .3.2 Principles and mechanisms of photocatalysis	54
II.5 .3.3 Factors affecting the efficiency of the photocatalytic process	56
II.5 .4 UV-visible spectroscopy	58
Bibliographic References	65
Chapiter III: Experimental results and interpretation	
III.1 Introduction	70
III.2 Synthesis and production of ceramics	70
III. 3 Stability conditions of the perovskite structure	71
III.3.1 Electroneutrality condition	72
III.3.2 Stoichiometric condition	72
III.3.3 Geometric condition	73
III.4 Powder characterisation	74

III.4 .1Characterisation of powders by infrared spectroscopy	74
III.4.1.1. X-ray diffraction analysis	74
III.4.2. Characterisation of powders by infrared spectroscopy	80
III.4.3. Morphological study of BNT ceramics	82
III.4.3.1. Scanning electron microscopy (SEM) characterization	82
III.4.3.2. Density	84
III.4.3.3. Porosity	86
III.5. Optical characterisation by UV-Visible	89
III.5.1. Methylene blue (MB) self-degradation test	90
III.5.2. Study of the photodegradation of methylene blue	91
III.5.2.1. Experimental protocol	91
III.5.2.2. Photocatalytic activity Sm doped and undoped BNT ceramics	92
III.5.2.3. Kinetic study of MB degradation by BNT pure and BNT doped	96
III.6. Conclusion	97
Bibliographic References	98
General conclusion	101

LIST OF ABBREVIATIONS AND SYMBOLS

BNT Bismuth Sodium Titanate Bio. 5Nao. 5Ti O3

PZT Titano-zirconate du plomb Pb $(Zr_{1-x}Ti_x) O_3$

CaTiO₃ Calcium titanate

XRD X-ray diffraction

SEM Scanning electron microscopy

FTIR Fourier Transform Infrared Spectroscopy

UV-Vis UV-Visible spectrophotometry

T_C The Curie Temperature

e Pellet thickness

d DensityΦ DiameterP Porosity

d_{exp} Experimental density of composition (g/cm³)

d_{th} Theoretical density of composition (g/cm³)

MSS Molten salts synthesis

Eg Energy of the band gap

Å Angstrum

IUPAC International Union of Pure and Applied Chemistry

DE The degradation efficiency

pH Potential of Hydrogen

dhkl The characteristic reticular distance of the atomic planes (hkl)

T Transmission

A Absorbance

VB The valence band

CB The conduction band

Tables & Figures





FIGURE	CHAPTER I				
Figure I.1	Typical microstructure of a ceramic surface	05			
Figure I.2	Digital photograph showing some traditional ceramics				
Figure I.3	Digital photograph showing some technical ceramics	06			
Figure I.4	Representation of the ideal cubic perovskite structure of type ABO_3	07			
Figure I.5	Direct effect	10			
Figure I.6	Inverse effect	11			
Figure I.7	Aspect schématique de la piézoélectricité	12			
Figure I.8	Organisation of the 32 crystalline classes	13			
Figure I.9	Hysteresis cycle of a ferroelectric material	14			
Figure I.10	Orientation of ferroelectric domains under the effect of an electric	15			
	field				
Figure I.11	Evolution of the dielectric permittivity of a ferroelectric as a				
	function of temperature				
Figure I.12	(a) BNT perovskite structure; (b) three-dimensional lattice formed				
	by BO ₆ octahedra				
	CHAPTER II				
Figure II. 1	Generalizability of the Molten Salts Synthesis Method in	29			
	Nanomaterial Morphologies				
Figure II.2	Bismuth trioxide powder	31			
Figure II.3	Sodium carbonate powder	32			
Figure II.4	Titanium dioxide powder				
Figure II.5	Samarium oxide powder				
Figure II.6	Zirconium dioxide powder				
Figure II.7	Zinc oxide powder	35			
Figure II.8	Iron oxide powder	35			

Figure II.9	Indium oxide powder 3		
Figure II.10	Grinding in a glass mortar	37	
Figure II.11	Sodium chloride	37	
Figure II.12	Potassium chloride	38	
Figure II.13	Programmable furnace for calcination	39	
Figure II.14	Thermal cycle of the calcination process	39	
Figure II.15	Transformation of powder before and after heat treatment	40	
Figure II.16	Pellets before and after grinding process	40	
Figure II.17	Salt washing process for removing dissolved salts	41	
Figure II.18	Oven drying	41	
Figure II.19	Powder before and after drying	42	
Figure II.20	Regrinding of the powder in a glass mortar	42	
Figure II.21	The hydrostatic press used to prepare the pellets	43	
Figure II.22	Pellets before sintering	43	
Figure II.23	Schematic diagram of sintering cycles	44	
Figure II.24	Diagram showing the main components of an automatic	46	
	diffractometer		
Figure II.25	X-ray diffractometer: XRD, PANalytical EMPYREAN.	47	
Figure II.26	Main components of a scanning electron microscope	50	
Figure II.27	Photocatalytic mechanism for environmental remediation	55	
	applications		
Figure II.28	The chemical structure of methylene blue	57	
Figure II.29	Evolution of Methylene Blue before and after dilution	57	
Figure II.30	Electronic transition states in UV-Visible spectroscopy	59	
Figure II.31	Operating principle of the UV-Visible spectrophotometer	60	
Figure II.32	Optical absorption between the occupied valence band and the	61	
	unoccupied conduction band		
Figure II.33	Band structure of a semiconductor with (a) direct and (b) indirect	62	
	gaps		
Figure II.34	The main steps of BNT ceramics synthesis by the molten salts	64	
	method		

CHAPTER III

Figure III.1	Typical diffraction spectra of the Tetragonal (T) and Rhombohedral (R) phases	74
Figure III.2	The different shapes of the peaks characteristic of the coexistence of the (T+R) phase	75
Figure III.3	Diffractogram for composition N°1 with X =0% calcined at 900°C	76
Figure III.4	Diffractogram for composition N° 2 with X =0.02% calcined at 900°C	77
Figure III.5	Diffractogram for two compositions N°1 and 2 calcined at 900 °C .1) $x = 0\%$, 2) $x = 2\%$	77
Figure III.6	Evolution of mesh parameters as a function of samarium rate for two samples calcined at 900 $^{\circ}\mathrm{C}$	80
Figure III.7	The infrared (IR) spectra of the mixtures before calcination and after calcination at 900 $^{\circ}\mathrm{C}$	81
Figure III.8	SEM micrographs of the composition N° 2 calcined at 900°C	83
Figure III.9	Evolution of density as a function of sintering temperature	85
Figure III.10	Evolution of density as a function of Samarium content	86
Figure III.11	Variation in porosity as a function of sintering temperature	87
Figure III.12	Evolution of porosity as a function of samarium content for all samples sintered at 1050 °C	88
Figure III.13	Evolution of porosity and density as a function of samarium content for all samples sintered at 1050 $^{\circ}$ C	88
Figure III.14	Evaluations of $(\alpha h \upsilon)^{1/2}$ as a function of energy (h υ) for the two compositions studied	90
Figure III.15	photocatalysis of methylene blue under solar irradiation	92
Figure III.16	Changes in the absorbance spectra of methylene blue under light irradiation in the presence of BNT-X=0 and BNT-X=0.02 photocatalysts	93
Figure III.17	Evolution of the relative concentration Ct/C0 of MB as a function of irradiation time in the presence of BNT-X=0 and BNT-X=0.02	94

Figure III.18	Photocatalytic efficiency of MB degradation by BN1-X=0 and	95
	BNT-X=0.02 catalysts	
Figure III.19	Variation of ln(Co/C) as a function of time for the degradation of	96
	methylene blue dye in the presence of BNT-X=0 and BNT-X=0.02	
	photocatalyst	



Table	CHAPTER I	PAGE
Table I.1	Evolution of crystal structures as a function of the value of the tolerance factor	08
	CHAPTER II	
Table II.1	The main crystallochemical characteristics of Bismuth trioxide $\ensuremath{Bi_2O_3}$	32
Table II.2	Main chromophore and auxochrome groups, ranked by increasing intensity	53
Table II.3	Main physico-chemical characteristics of Methylene Blue	57
	CHAPTER III	
Table III.1	Characteristics of the starting products	70
Table III.2	Different ceramic compositions prepared	71
Table III.3	Ionic radii and Valance number of elements in prepared matrices	71
Table III.4	Results of the electroneutrality condition for the synthesized	72
	ceramic compositions	
Table III.5	Stoichiometric condition of the studied compositions	72
Table III.6	Geometric tolerance factor(t) for the studied compositions	73
Table III.7	The required masses of oxides for the different compositions	73
Table III.8	Region of coexistence of the Tetragonal-Rhombohedral phases and	76
	indexing of the corresponding planes	
Table III.9	Crystallographic phases identified after calcination at 900 °C	78
Table III.10	Estimation of the pyrochlore phase proportion based on the	79
	intensity of characteristic peaks	
Tahla III 11	Calculated crystalline parameters of the prepared RNT sample	79

Table III.12	Experimental and theoretical density, densification rate and	84
	porosity for all samples	
Table III.13	Evolution of the MB concentration (without catalyst) under	91
	different conditions for 3 hours	
Table III.14	Eg values and degradation rate (D%) for BNT-X=0 and BNT-	95
	X=0.02	
Table III.15	Rate constants (K _{app}) estimated from the Langmuir model and	97
	linear regression coefficients (R2) for BM degradation by the	
	different photocatalysts	

GENERAL INTRODUCTION

Lead-based ceramics have been widely used for electronic and microelectronic devices because of their excellent piezoelectric properties [1,2]. However, on account of the high volatilization of toxic lead oxide during sintering process, a great many countries have enacted laws to restrict their applications. In recent decades, more and more research works have been focused on searching for environment-friendly lead-free piezoelectric ceramics to replace the conventional lead-based materials [3].

Among the lead-free piezoelectric materials, sodium bismuth titanate (Bi_{0.5}Na_{0.5}TiO₃, abbreviated as BNT) and Barium titanate (BaTiO₃, abbreviated as BT) are accepted as an important material for the fabrication of lead-free piezoelectric materials. The BNT shows strong ferroelectric property along with high Curie temperature, high remnant polarization and a coercive field at room temperature [4]. However, the large coercive field and large conductivity makes pure BNT as hard to pole, which hinders its industrial application.

Researchers have used various methods to improve the structural and electrical characteristics of perovskite materials based on BNT. The ratio of sodium to bismuth (Na/Bi) is essential in defining the electrical properties of these materials. In addition, the introduction of nonstoichiometry of sodium (Na) or bismuth (Bi) at the A-site or titanium (Ti) at the B-site can modify the dielectric and electrical properties of BNT in accordance with specific requirements. However, adding a small amount of a suitable dopant element to either the A or B-site of the BNT structure has piqued interest. This method has demonstrated its capacity to be very captivating because to its ability to make substantial alterations to the characteristics of materials based on BNT [5, 6].

A partial substitution of lead-based ferroelectrics with samarium (Sm) has been demonstrated to improve their piezoelectric properties [7,8,9]. On the other hand, the Sm substitution at certain concentrations was found to reduce the thermal stability of piezoelectric constants of lead-based materials [7, 10]. These findings motivated us to study the effect of Sm, occupying different A-site positions in the BNT perovskite, on different structural, optical, and electrical properties of the lead-free BNT ceramics.

Furthermore, the act of doping at the B-site is likewise regarded as advantageous for augmenting certain characteristics of BNT perovskite materials [11].

GENERAL INTRODUCTION

Bismuth sodium titanate (BNT), is a typical perovskite oxide with a high conductivity and narrow band gap (\sim 2.8 eV) make it a promising photocatalytic material [12].

In this study, we focused on exploring new compositions of BNT-type by doping it with samarium ions at the A sites, with the aim of enhancing its photocatalytic properties. To this end, we synthesised a new matrix of the system :(Na_{0.5} Bi_{0.5})_{1-x} Sm_x (Ti_{0.8} Zr_{0.2})_{0.9}(Fe_{1/5}Zn_{1/5} In_{3/5})_{0.1}, with x successively taking the values 0.00; 0.02; 0.04; 0.06.

This study is divided into three chapters:

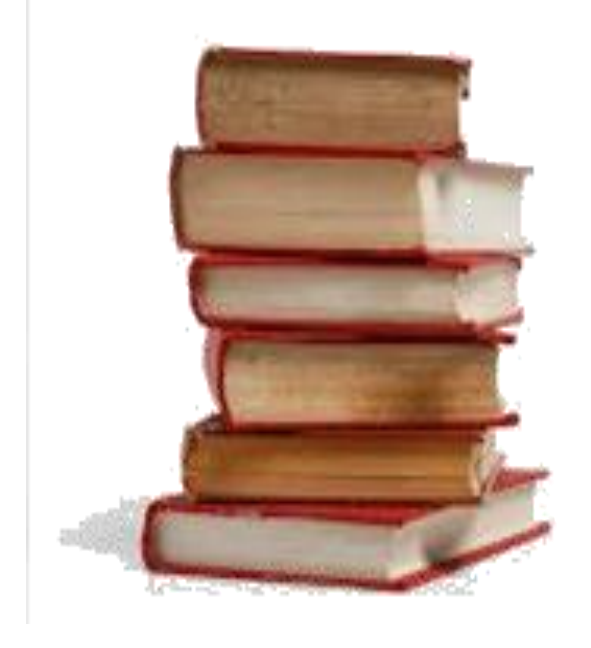
- ♣ The first chapter deals with a theoretical overview of ceramics with a focus on BNT, its properties and dopage.
- ♣ The second chapter presents the method used to produce BNT ceramics, as well as the various techniques used to characterise the materials produced.
- **The third chapter** is devoted to the discussion of empirical results.

GENERAL INTRODUCTION



- [1] **Jaffe.B et al.** The piezoelectric effect in ceramics. *Piezoelectric ceramics*, 7-21. (1971).
- Yang. Z et al. Effect of sintering process on characteristics of multilayer piezoelectric Pb (Mg_{1/3}Nb_{2/3}) O₃–Pb (Zn_{1/3}Nb_{2/3}) O₃–Pb (Zr, Ti) O₃ ceramic transformers. *Japanese Journal of Applied Physics*, 46(10R), 6746. (2007).
- **Zidi.** N et al. Impedance spectroscopy studies on (Na_{0.5} Bi_{0.5})_{0.94} Ba_{0.06} TiO₃+ 0.3 wt% Sm₂O₃+ 0.25 wt% LiF lead-free piezoelectric ceramics. *Journal of Bulletin of Materials Science*, 38, 731-737. (2015).
- **Badapanda. T et al.** Dielectric, ferroelectric and piezoelectric study of BNT-BT solid solutions around the MPB region. In *IOP Conference Series: Materials Science and Engineering*, 178(1), 012032). IOP Publishing. (2017).
- [5] **Seo.I et al.** The effect of A site non-stoichiometry on 0.94 (Na_yBi_x) TiO₃-0.06 BaTiO₃. *Journal of the European Ceramic Society*, 37(4), 1429-1436. (2017).
- [6] Chen. X et al. Effects of Bi deficiency on the microstructural and conductive properties of Na_{0.5}Bi_{0.5}TiO₃ (NBT) perovskites. *Solid State Ionics*, 309, 152-162. (2017).
- [7] **Li. F et al.** Ultrahigh piezoelectricity in ferroelectric ceramics by design. *Journal of Nature materials*, 17(4), 349-354. (2018).
- [8] Li. F et al. Giant piezoelectricity of Sm-doped Pb (Mg_{1/3}Nb_{2/3}) O₃-PbTiO₃ single crystals. *Journal of Science*, 364(6437), 264-268. (2019).
- [9] Malic. B, Rojac. T. High piezoelectricity via enhanced disorder. *Journal of Nature Materials*, 17(4), 297-298. (2018).
- [10] Guo. Q et al. High-performance Sm-doped Pb (Mg_{1/3}Nb_{2/3}) O₃-PbZrO₃-PbTiO₃-based piezoceramics. *Journal of ACS Applied Materials & Interfaces*, 11(46), 43359-43367. (2019).
- **Rahal. R et al.** Synthesis of novel Bi_{0.5} Na_{0.5}Ti_{0.95} (Ni_{0.2}Fe_{0.2} Sb_{0. 6}) _{0.05} O₃ perovskite material used as a photocatalyst for methylene blue degradation under sunlight irradiation. *Journal of Reaction Kinetics, Mechanisms and Catalysis, 137*(4), 2377-2393. (2024).
- **Zhao.Q et al**.Highly-efficient piezocatalytic performance of nanocrystallineBaTi_{0. 89}Sn_{0. 11}O₃ catalyst with Tc near room temperature. *Journal of Nano Energy*, 85, 106028. (2021).

Chapter I: Bibliography





I.1. Introduction

The generic term 'ceramic' covers areas as diverse as traditional ceramics (bricks, tiles, etc.) and so-called technical ceramics: ceramics for mechanical and thermomechanical applications or ceramics for electronic applications [1]. Ceramic materials have one essential characteristic compared with other materials: the atoms or constituents of their crystalline lattice are generally very firmly linked together by strong bonds (ionic and covalent) [2].

The interest in oxides with the ABO₃ perovskite structure has been driven for many years by the ease with which the nature of the A and B cations present in the structure can be changed. Modifications to these elements lead to changes in the intrinsic properties of the materials [3].

In this chapter, we present a general overview of ceramics, the perovskite structure and its properties, BNT-type ceramics, and doping techniques.

I.2. General Information on ceramics

The term 'ceramic' generally refers to an inorganic material, neither metallic nor polymeric, obtained by a sintering process. This material is often produced from powders that have been consolidated and heated to achieve high density and strength. Used in a variety of fields, ceramics are characterised by their robustness and resistance to high temperatures and chemical agents.

A ceramic is a polycrystalline inorganic material with a complex structure of grains and grain boundaries (fig. I.1) [1].



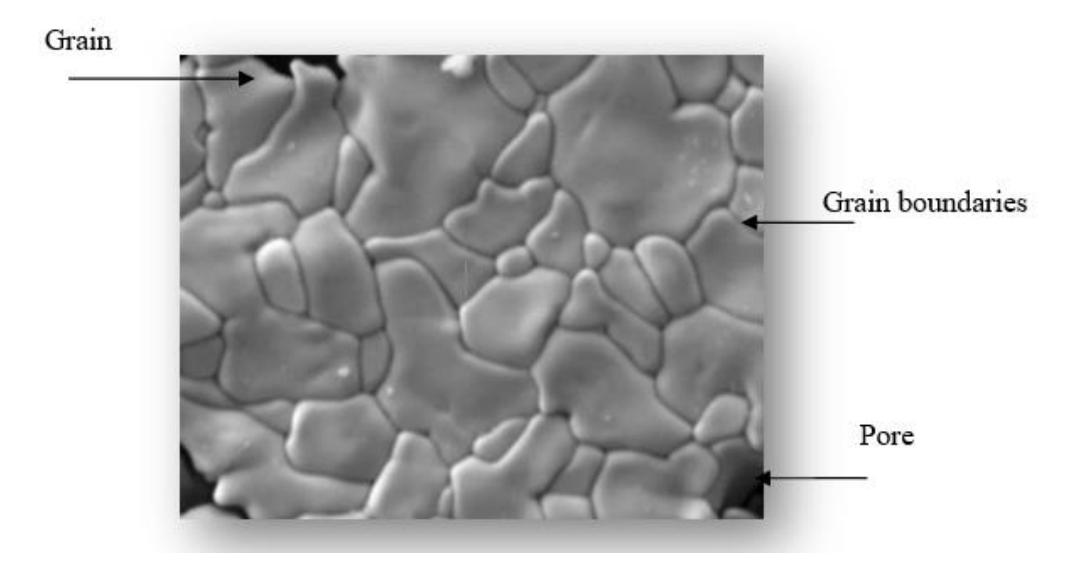


Figure I.1: Typical microstructure of a ceramic surface

I.2.1. Classification of ceramic

There are two types of ceramics:

4 Traditional ceramics

Traditional ceramics are made from natural raw materials (clay, kaolin, quartz) and are generally cast. Examples include earthenware, terracotta (building bricks) and porcelain (crockery, decorative objects) [1].



Figure I.2: Digital photograph showing some traditional ceramics



Technical ceramics

Technical ceramics include materials developed recently in research laboratories because of their exceptional chemical or physical properties.

They are most often obtained by sintering (thermomechanical treatment in special furnaces, which causes powder granules to bond with a cold-prepared agglomerate) or electrofusion (the oxides are poured directly into a mould) [1].



Figure I.3: Digital photograph showing some technical ceramics

I.3. Perovskite structure

Perovskites are one of the main families of crystalline oxides. Their name comes from the mineral CaTiO₃, which has a similar crystalline structure.

The typical lattice of a perovskite has cubic symmetry, with similar structures that are more or less distorted. The chemical composition of an oxide with a perovskite structure is usually made up of an alkaline-earth cation (A), a tetravalent transition cation (B) and oxide anions.

The interest in oxides with the ABO_3 perovskite structure for many years stems from the ease with which the nature of the A and B cations present in the structure can be changed. Modifications to these elements lead to a change in the intrinsic properties of the material, leaving the door open to all sorts of physical properties depending on the chemical and electronic nature of the A and B atoms [4].



I.3.1. Crystalline structure

Chapter I

Most compounds of the formula ABO_3 crystallise in the perovskite structure, which corresponds to the typical $CaTiO_3$ structure. In the ideal case, this structure is cubic with space group P_{m3m} and can be represented as a stack of regular octahedra with the oxygen ions at the top. These octahedra are occupied at their centres by the B cations, with the A cations occupying the centres of the cuboctahedral cavities [5].

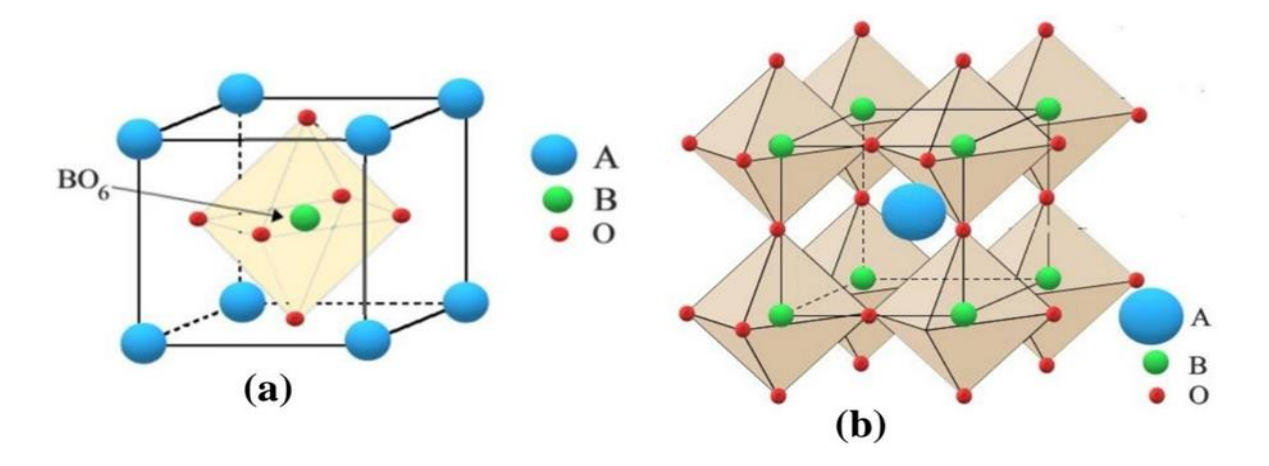


Figure I.4: Representation of the ideal cubic perovskite structure of type ABO₃ [6]

I.3.2. Ideal perovskite structure

Simple perovskites are, by definition, perovskites in which both A and B are occupied by a single chemical element. It should be noted that a large number of compounds belonging to this family exhibit a so-called classical ferroelectric phase transition on cooling [7].

I.3.3. Complex perovskite structure

Unlike simple perovskites, complex perovskites must have A and/or B occupied by at least two different atoms. The distribution of cations can be either random or partially or totally ordered. Depending on whether they are ordered or disordered, these compounds behave as classical ferroelectrics, relaxor ferroelectrics or relaxors [7].

I.3.4. Stability of the structure

The choice of atoms positioned at the sites of the A and B cations in the crystal structure of perovskites is crucial to the stability of these compounds, with the relationship between the ionic radius lengths of the A and B cations and the X anion, the iconicity of the bonds and the





difference in electronegativity between the cations and the anions playing a decisive role in determining the properties of these materials [8].

I.3.4.1. Tolerance factor

The radii of the cations must obey the relation:

$$t = \frac{\overline{R}A + RO}{\sqrt{2} \ (\overline{R}B + RO)}$$
 Eq. I.1

With:

 $\bar{R}Ai = \sum_{i=1}^{k} XAiRAi$: Average radius of Ai atoms.

 \overline{R} Bj= $\sum_{j=1}^{l} XBj RBj$: Average radius of Bj atoms.

Where RAi, RBj and RO are the ionic radii of atoms A, B and O. According to Poix, the structure is only possible for $0.75 \le t \le 1.06$. However, the perovskite will be all the more stable the closer t is to 1. For $t \le 1$: all the ions are in contact, we will have a perfect compact stack. The radius of the B ion in the range 0.6-0.7Å, seems to be a favourable condition to produce ferroelectricity.

+ For t >1: ion B may be mobile in the network.

For t < 1: ion A may be mobile in the network [3].

Table I.1: Evolution of crystal structures as a function of the value of the tolerance factor [9].

t < 0.75 Ilmenite		t > 1.06 Hexagonal		
	0.75 < t <0.96 Orthorhombic distortion	0.96 < t <0.99 Rhombohedral distortion	0.99< t<1.06 Cubic	



I.3. 4.2 Stoichiometric condition

$$\sum_{i=1}^{k} XAi = 1; 0 \le X_{Ai} \le 1$$

$$\sum_{j=1}^{l} XBj = 1; 0 \le X_{Bj} \le 1$$
Eq. I.2

With:

X_A: The fraction of moles at the A_i cation.

 X_B : The fraction of moles at the B_i cation [3].

I.3. 4.3 Electroneutrality condition

Consider the following compound with a perovskite structure:

$$(A_1^1 A_2^2 A_3^3A_n^k)(B_1^1 B_2^2 B_3^3B_n^l)O_3$$

Where k and l indicate the categories of the corresponding A and B sections.

$$\sum_{i=1}^{k} X_{Ai} \, \mathbf{n}_{Ai} + \sum_{i=1}^{l} X_{Bi} \, \mathbf{n}_{Bi} = 6$$
 Eq. I.3

With:

n Ai: Valence number of cation Ai.

n Bi: Valence number of cation Bj [3].

I.4. Properties of perovskites

I.4.1. Electrical properties

I.4.1.1. Piezoelectricity

Piezoelectricity is the ability of certain materials (crystals, ceramics, polymers or composites) to transform electrical energy into mechanical energy. The electrical charge is proportional to the mechanical stress imposed: this is the direct piezoelectric effect (fig I.5).

The reciprocal effect, also known as the inverse effect (fig I.6), means that the application of an external electric field causes mechanical deformation of the material.





It was the Curie brothers who observed and explained the direct effect in 1880[10], but it was Lippmann who theoretically suggested the opposite effect, which was confirmed experimentally by the Curie brothers.

Piezoelectricity can be defined as a phenomenon of coupling between elastic energy and electrical energy (a relationship between two variables: electrical and mechanical and vice versa).

These piezoelectric effects can only be observed on insulators [11].

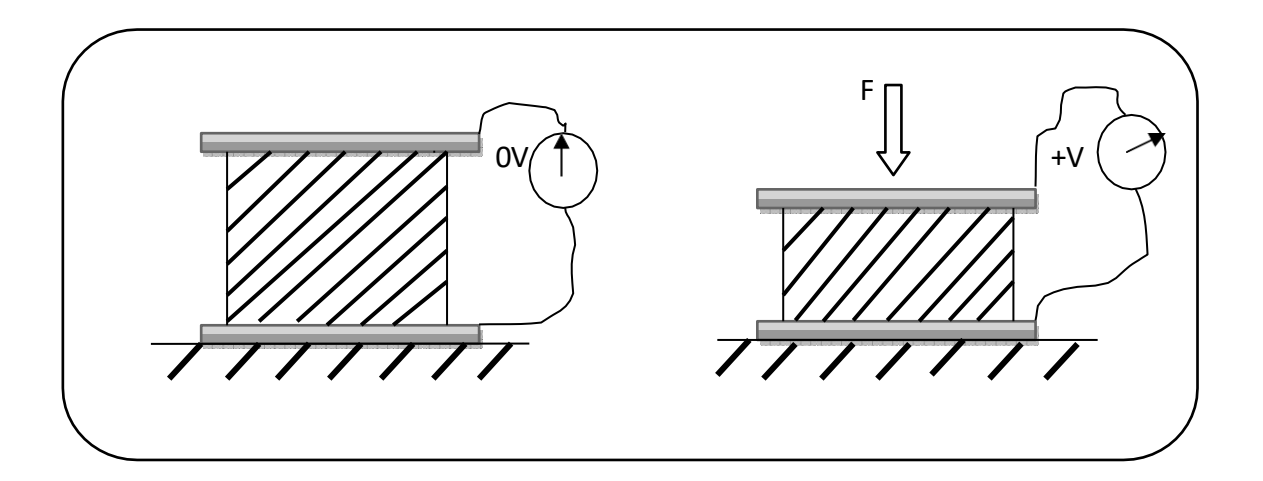


Figure I.5: Direct effect

A force is applied and a voltage is collected [12].

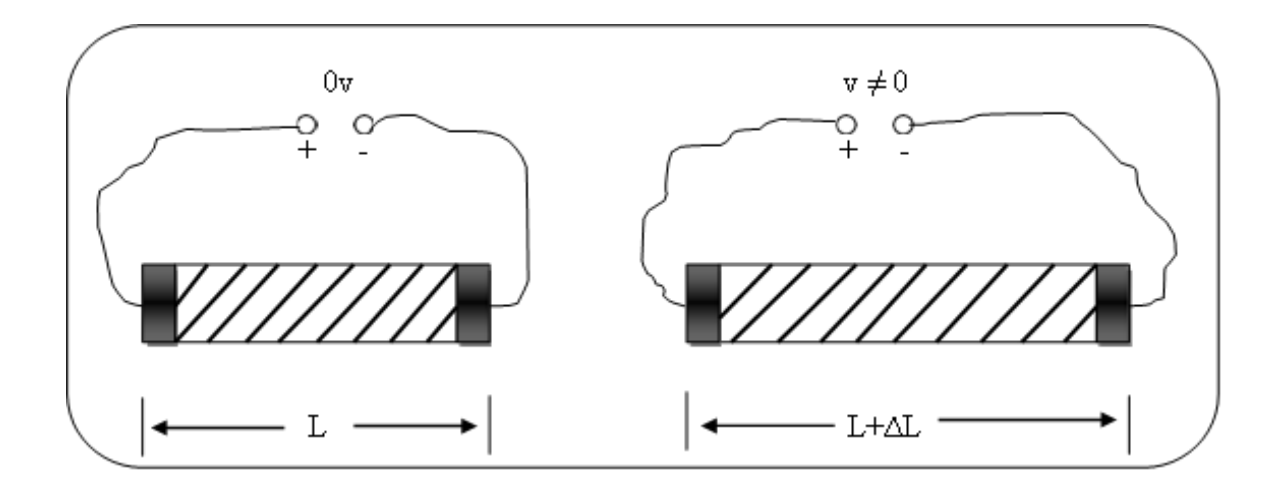


Figure I.6: Inverse effect

Tension is applied and deformation is recorded [12].



I.4.1.1. Symmetry and piezoelectricity

In crystalline solids, piezoelectricity is directly linked to the symmetry of the crystals and manifests itself as a polarisation of the lattice. This dipole moment is created by the separation of the centres of gravity of the positive and negative charges as a result of deformation under stress.

The symmetry properties of crystals are of fundamental importance to the existence or otherwise of piezoelectricity. Anybody with a centre of symmetry cannot be piezoelectric, whereas crystals without a centre of symmetry can be (Fig. I.7) [12].

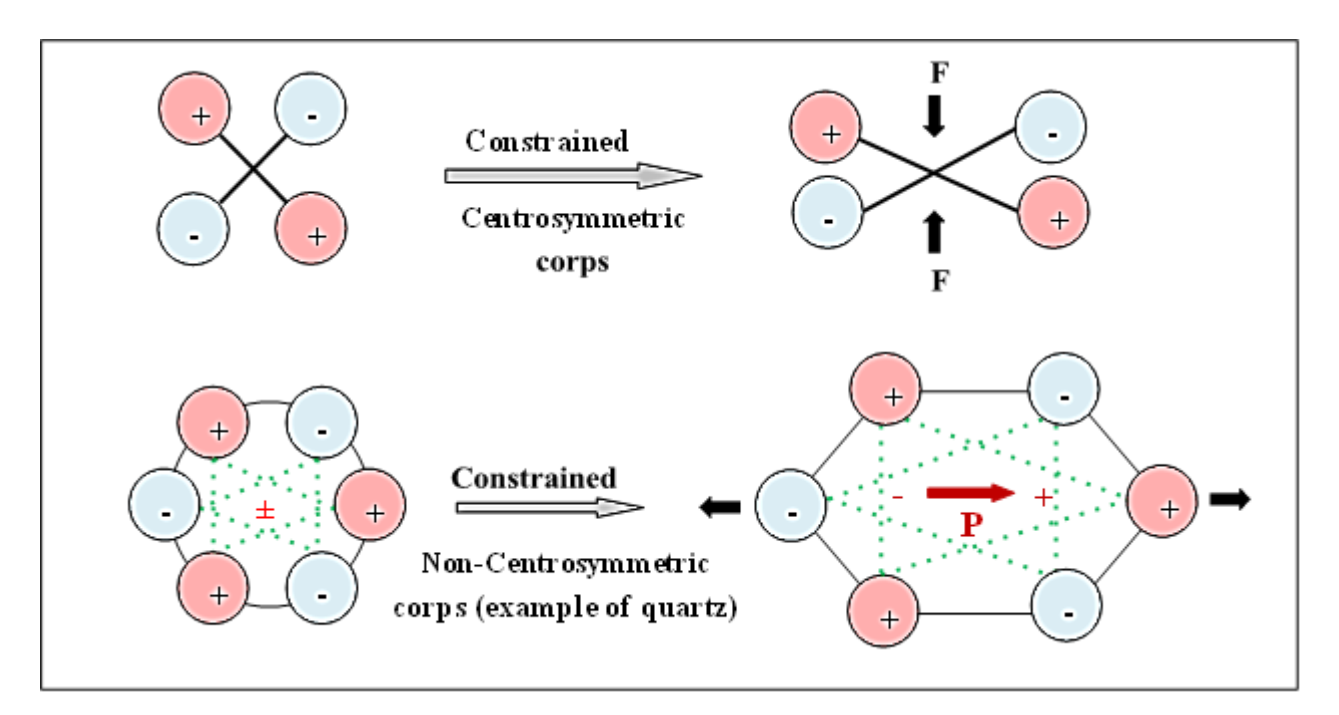
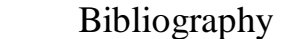


Figure I.7: Aspect schématique de la piézoélectricité [13]

In crystallography, all structures are classified according to 32 classes of symmetry. 11 of these classes are said to be centrosymmetric and therefore cannot exhibit polar properties or spontaneous polarisation. One of the other 21 classes has symmetry elements that prevent it from exhibiting polar characteristics (non-piezoelectric). The remaining 20 classes are piezoelectric, of which 10 are pyroelectric, i.e. they are electrically polarised in the absence of an applied electric field. They are called pyroelectric because of the variation in the amplitude of the dipole moment with temperature. Pyroelectric crystals include ferroelectric crystals in which the polar axis, which supports a permanent dipole, is mobile in the crystal lattice under the influence of an external electric field.





The breakdown of the 32 crystalline classes according to these different names is summarised in (Fig I. 8) [14,15].

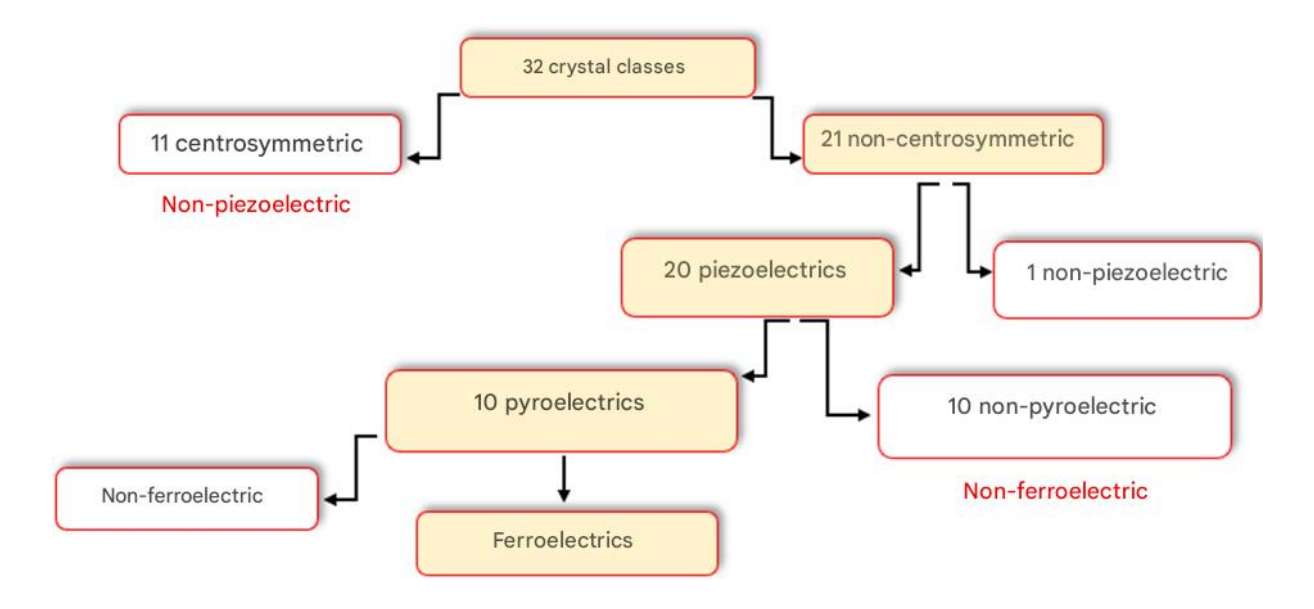


Figure. I. 8: Organisation of the 32 crystalline classes

I.4.1.2. Pyroelectricity

Chapter I

Ten of the twenty piezoelectric crystal classes exhibit natural polarisation in at least one direction, also known as spontaneous polarisation (or permanent dipole moment) [16]. As the amplitude of the dipole moment is a function of temperature, the variation in the spontaneous polarisation of these crystals can be observed by measuring the charges flowing in an external closed circuit when the temperature is varied. These are pyroelectric crystals [17].

I.4.1.3. Ferroelectricity

Ferroelectricity is a sub-group of pyroelectricity. A ferroelectric material is characterised by a structural transition temperature (Tc) between a high-temperature phase exhibiting paraelectric (non-polar) behaviour and a low-temperature phase exhibiting spontaneous polarisation due to spontaneous distortion of the crystal lattice [18,19]. This polarisation can be reoriented or even reversed (switched) in equivalent crystallographic directions under the effect of the external electric field, giving rise to hysteretic behaviour similar to that observed in ferromagnetic materials under the effect of a magnetic field. The hysteresis cycle P=f(E) is thus considered to be the signature of ferroelectricity [20].



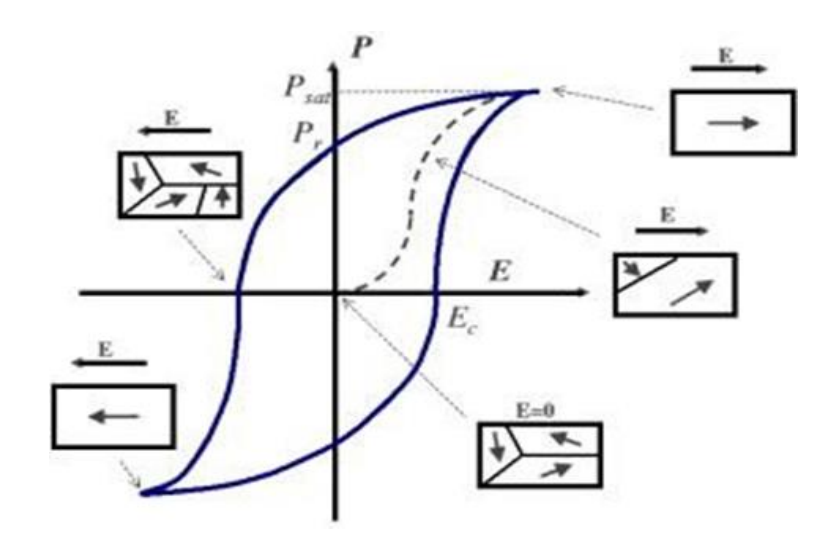


Figure. I. 9: Hysteresis cycle of a ferroelectric material

Ps: Psat: Polarisation saturation.

Pr : Reshape polarisation.

Ec: Coercive field [20].

I.4.1.3.1. Ferroelectric domains

Ferroelectric crystals are composed of domains, which are regions with different polarisation directions separated by domain walls. In the absence of an external field, the domains have random orientations, making the material non-polar. However, when an electric field is applied, the polarisation directions of the domains undergo a reorientation process. This leads to an increase in the number of domains aligned with the applied field and/or the disappearance of domains of opposite polarisation. In materials with a tetragonal and rhombohedral structure, the domains at 180° turn completely inside out without changing the lattice structure. On the other hand, domains at 71° and 109° in rhombohedral structures, and at 90° in tetragonal structures, induce significant deformation of the lattice, leading to partial reorientation. The polarisation process of a ferroelectric ceramic is illustrated qualitatively in (Fig.I.10) [21]



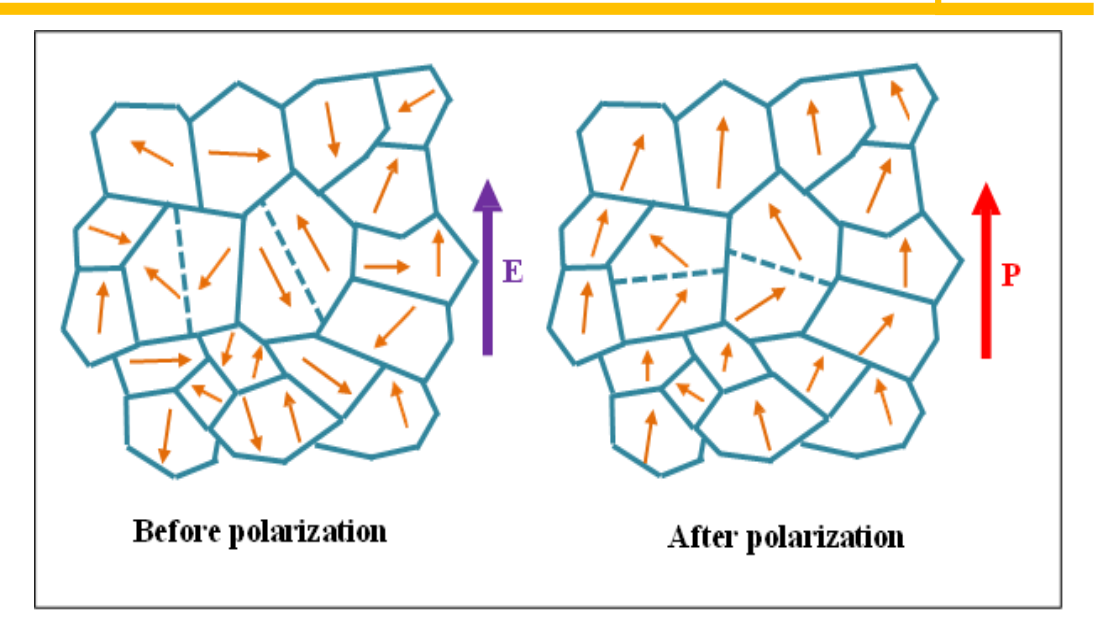


Figure I.10: Orientation of ferroelectric domains under the effect of an electric field [12].

I.4.1.3.2. The Curie point

The Curie point T_C is the temperature at which a ferroelectric material undergoes a structural phase transition to a state where spontaneous polarization disappears. At the Curie point, the relative dielectric permittivity ϵr ($\epsilon r = \epsilon / \epsilon_0$) reaches a maximum value. Above T_C , the ferroelectric material becomes paraelectric, which is reflected by a peak in the permittivity versus temperature curve.

The temperature and dielectric constant in many ferroelectric materials above the curie point are governed by the Curie-Weiss law:

$$\mathbf{\varepsilon} = \varepsilon_0 + \frac{C}{(T_T T0)}$$
 Eq. I.4

Where:

ε: Is the dielectric permittivity of the material.

 ε_0 : The dielectric permittivity of vacuum.

C: Is the curie constant.

T₀: Is the Weiss curie temperature.





The Weiss curie temperature is often different from the T_C curie point (the temperature at which ϵ is maximum). For first-order transitions, $T_0 < T_C$ whereas for second-order transitions, $T_0 = T_C$ [22].

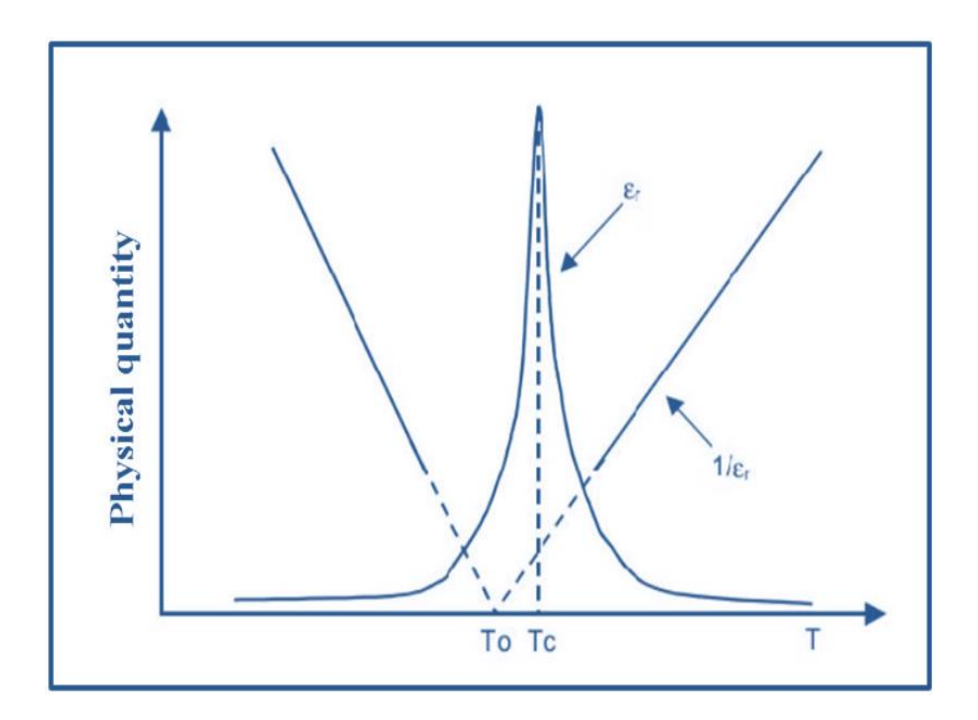


Figure I.11: Evolution of the dielectric permittivity of a ferroelectric as a function of temperature [21].

I.4.1.4. Dielectricity

Chapter I

A dielectric is a collection of atoms or molecules made up of electrons (negative) and nuclei (positive), all of which are electrically neutral. It is a medium that cannot conduct electric current. As such, it is sometimes referred to as an electrical insulator. Glass and many plastics are examples of such media.

Despite the fact that dielectric media cannot conduct current, they have a number of electrical characteristics. Under the effect of an external electric field, negative and positive charges are displaced very slightly. The electrons present in a dielectric medium cannot, by definition, move over long distances. They can, however, exhibit movements of very small amplitude on a macroscopic scale, but which can be the cause of many phenomena. These movements are often oscillations around the nucleus: the electron cloud can be deformed, creating an electrostatic dipole. The same applies to the overall movement of atoms within the material (which also creates dipoles) [23].



I.4.2. Photocatalytic properties

Perovskite oxides are one of a number of photocatalytic materials that have shown great promise and efficiency as photocatalysts under visible light irradiation, due to their crystalline structures and electronic properties. In addition, lattice distortion in perovskite compounds strongly influences the separation of photogenerated charge carriers. Several research studies have been carried out on perovskite materials such as titanates [24,25], vanadium- and niobium-based perovskites [26,27], have shown excellent photocatalytic activity under UV-Vis irradiation.

I.4.3. Catalytic properties

Perovskites have been extensively studied in recent years, their catalytic properties also opening up a very wide field of use in heterogeneous catalysis, in particular as electrocatalysts in fuel cells. Several electrochemical studies concerning the evolution and reduction of oxygen on electrodes based on these oxides have been carried out in aqueous alkaline media. They revealed very significant electrocatalytic behaviour with regard to the release and reduction of molecular oxygen at ambient temperature. It should be noted that this work reported that the catalytic activity of perovskites is mainly linked to the synthesis method, the composition of the electrode material and the electrical properties of the transition metal in these oxides [28].

I.5. Generalities on BNT perovskite-type oxide

I.5.1. History

In recent years, the trend towards environmental protection has led to a search for new types of ferro piezoelectric materials, lead-free or with a low lead content, which could lead to numerous applications in the form of bulk ceramics to replace the family of lead-based ceramics (PbZrTiO₃(PZT)).

In 1956, a Soviet team replaced Pb²⁺ ions with Bi³⁺ and Na⁺ ions in the perovskite structure of PZT, to form Bi_{0.5}Na_{0.5}TiO₃ (BNT). In 1961, Smolensky et al. reported that these ceramics (BNT) have ferroelectric properties.

Chapter I Bibliography



Between 1962 and 1970, there was very little activity in the field of BNT, with only five articles on these materials in ceramic form. However, the new guidelines on lead toxicity led to renewed interest in BNT as a lead-free ferroelectric material [29].

I.5.2. The BNT-type structure

BNTs have a complex perovskite structure, in which Bi³⁺ and Na⁺ ions occupy the A site, while Ti⁴⁺ ions occupy the B site of the perovskite unit cell, with the general formula ABO₃ [30] (the vertices of the cube) randomly occupy the bismuth atoms (Bi) or a sodium atom (Na), the B position (the centre of the cube) is occupied by titanium (Ti), and an oxygen atom (O) is located at the centre of the face. These oxygen atoms form an octahedral site, with a titanium atom at its centre. The octahedral sites are connected by vertices; their geometric arrangement forms a cube with sodium and bismuth atoms at their centre(fig I.12) [29].

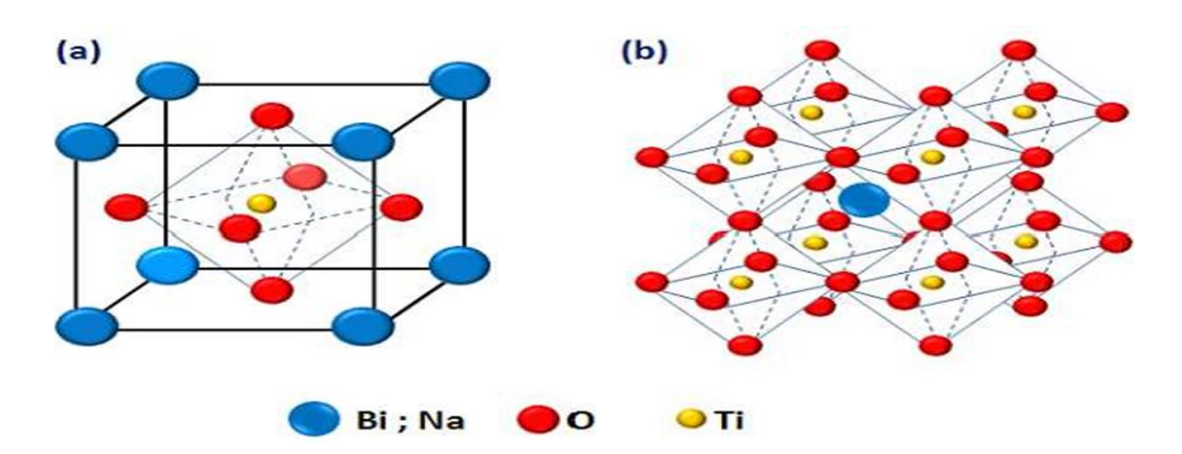
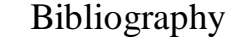


Figure I.12: (a) BNT perovskite structure; (b) three-dimensional lattice formed by BO₆ octahedra [31]

I.5.3. The dielectric and ferroelectric properties of BNT

At room temperature, the space group of BNT is R3c. Consequently, its point group is 3m and it is a pyroelectric (polar) compound. Its spontaneous polarisation is of the order of $35\mu\text{C/cm}^2$. What's more, the direction of its polarisation can be reversed by the action of an electric field. BNT is therefore a ferroelectric material, whose coercive field measured on ceramics is between 6 and 7.5kV/mm, whereas it is lower on single crystals (2.8kV/mm). As a ferroelectric material, BNT also has piezoelectric properties. Its piezoelectric coefficients are of the order of d33=65pC/N, d31=15pC/N [32].





As a function of temperature, BNT exhibits several phase transitions and, consequently, its properties change. Several authors have shown, using pyroelectric measurements, that BNT is ferroelectric up to 200-230°C.

However, X-ray and neutron diffraction studies have never revealed a doubling of the lattice parameters characteristic of anti-ferroelectric materials. In addition, piezoelectric activity was detected above 230°C, attesting to the presence of a non-Centro symmetrical phase.

This is why suchanicz hypothesised that this phenomenon (double loop) would be the response of a system where several phases coexist (rhombohedral and tetragonal) under the action of a strong electric field. [33,34].

I.5.4. Advantages and disadvantages of BNT

Despite its good ferroelectric and piezoelectric properties, BNT's main drawback is the existence of significant dielectric leakage, which explains the problems generally encountered during the material's polarisation process. The high leakage currents observed can result from the vaporisation of the bismuth and therefore from the creation of oxygen vacancies, which lead to the anchoring of the walls of ferroelectric domains [31,34].

To overcome this problem, two solutions have been envisaged: altering the composition of the A site [35], doping and/or forming solid solutions [36].

I.6. Perovskite doping

Chapter I

I.6.1. Definition of doping

Doping is the action of adding small quantities of impurities to a pure substance in order to modify its conductivity properties.

The properties of semiconductors are largely governed by the quantity of charge carriers they contain. These carriers are electrons or holes.

Doping a material involves introducing atoms from another material into its matrix. These atoms replace some of the initial atoms and thus introduce more electrons or holes. The atoms of the doping material are also called impurities, and are in a dilute phase: their concentration remains negligible compared to that of the atoms of the initial material [37].



I.6.2. Doping purposes

The aim of doping is to modify the intrinsic electronic property of the pure crystal, i.e. The crystal whose initial impurity content is largely equal to the concentration of the doping element. These impurities may be homovalent, i.e. Have the same valency as the atoms in the crystal they replace, or heterovalent, if they have a different valency [38].

I.6.3. Doping techniques

I.6.3.1. Ion implantation doping

Ion implantation doping consists of accelerating ionised impurities with an electric field to electric field to give them the energy they need to penetrate the material to be doped. This method allows a wide variety of doping elements to be used. The single-energy mono-energy beam and vacuum chamber make it possible to achieve high reproducibility and localized localised doping. In practice, the implanter is an ion accelerator [39].

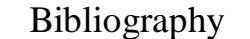
I.6.3.2. Diffusion doping

Diffusion doping is carried out in an oven. The dopant can be obtained from:

- ♣ Solid source: the sample to be doped is placed in the oven opposite a solid compound containing the dopant. The doping atom is then transported to the sample by an inert carrier gas. Carrier gas, from the solid compound which sublimates.
- **↓ Liquid source:** the carrier gas bubbles through the liquid or brushes against its surface at a chosen temperature. The partial pressure of the compound in the gas is equal to the vapour pressure of the liquid.
- **♣ Gaseous source:** the gas containing the doping species is introduced into the furnace. Doping takes place at a temperature of between 850°C and 1,150°C, to allow diffusion of the doping species in the material (sample to be doped) [40].

I.6.3.3. Doping by laser technique

A laser induces a very rapid melting/solidification cycle (of the order of 10⁻⁸ S) during which the dopant is diffused into the liquid phase. As the rate of diffusion of the dopant is very rapid in the liquid phase and negligible in the solid phase, repeating this process makes it





possible to obtain a dopant density greater than the solubility limits obtained using conventional techniques [41].

I.6.3.4. Doping by epitaxy

Chapter I

Epitaxy is the technological process of growing crystal on crystal. The technique therefore consists of using the substrate as a crystalline growth seed and growing the layer by adding the elements that make up the new layer [39].

I.6.4. Classification of doping agents

Ferroelectric materials are rarely used for technical or very specific applications in their simple formulation: in order to optimise their integration into devices, they are generally modified by the addition of one or more foreign cations which will replace the A or B sites of the ABO₃ perovskite structure and sometimes by anions to replace the oxygen. Dopants are generally classified into three categories [42,43].

4 Isoivalent dopants

Isoivalent dopants are ions with the same valency and ionic radii close to those of the cations they replace. In the case of BNT, the most commonly used dopants to substitute Bi³⁺ at site A are La³⁺, Nd³⁺, Sm³⁺ and other rare earths, while for site B, Ti⁴⁺ can be partially replaced by Zr⁴⁺, Hf⁴⁺, Sn⁴⁺. The incorporation of these elements alters the structural properties of BNT, increasing or decreasing lattice distortion, which can influence dielectric, piezoelectric and Curie temperature (T^c) properties.

Acceptor dopants

Acceptor dopants in BNT are generally referred to as hard dopants, as they introduce charge defects compensated by the creation of oxygen vacancies. Examples include Fe³⁺, Co³⁺, Mn³⁺, Ni²⁺, Cr³⁺, Al³⁺ for site B in substitution of Ti⁴⁺. These dopants lead to an increase in the coercive field, an improvement in the mechanical quality factor, as well as a reduction in permittivity and dielectric losses.

Donor dopants

Donor dopants, also known as soft dopants, are ions with a higher valence than the cation they replace. For BNT, the soft dopants commonly used at site A include La³⁺, Nd³⁺, Sm³⁺, while at site B, Nb⁵⁺, Ta⁵⁺, W⁶⁺ are often used to replace Ti⁴⁺. The main effect of these dopants



is to improve the electrical conductivity and optimise the ferroelectric and piezoelectric properties of BNT.

Multi-purpose dopants

These are dopants with a variable valency, such as manganese and uranium. These additives can change valency (variable oxidation number) to adapt to the valency of the vacant site to be occupied [44].



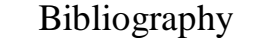


Bibliographic References

- [1] Haussonne. F. J. M. Céramiques pour composants électroniques. Ed. Techniques Ingénieur. (1820).
- [2] Cheng.H et al. Reaction mechanisms in the formation of lead zirconate titanate solid solutions under hydrothermal conditions. *Journal of the American Ceramic Society*, 76(3), 625-629. (1993).
- [3] **Lebbal. Ch, Lahlouhi. A.** Synthèse et caractérisation structurale de la solution solide (Na_{0.5}, Bi_{0.5}) xBa_{0.9-x} Mg_{0.1} TiO₃, mémoire de master, univ Mohamed Khider- Biskra-Algérie. (2019).
- [4] Omari. E. Synthèse, propriétés rédox et catalytiques des oxydes polymétalliques La Fe_{1-x} M_x O₃(M : Cu, Zn, Co), thèse de doctorat, univ Mohamed Khider -Biskra-Algérie. (2021).
- [5] Smyth. D. M. Defects and order in perovskite-related oxides. *Journal of Materials Science*, 15(1), 329-357. (1985).
- [6] **Hussain. S et al.** Unique hierarchical mesoporous LaCrO3 perovskite oxides for highly efficient electrochemical energy storage applications. *Journal of Ceramics International*, 45(12), 15164-15170. (2019).
- [7] Hentati. M.A. Effets des inhomogénéités locales et des contraintes extérieures sur les propriétés diélectriques et structurales des monocristaux PZN-x%PT, thèse de doctorat, Faculté des Sciences de Sfax Tunisie. (2013).
- [8] Berkane. W, Bouderhem. G. Éélaboration et caractérisation d'un matériau de structure pérovskite, mémoire de master, univ Mohamed Khider-Biskra- Algérie. (2022).
- [9] **Abdelli. R. K.** Synthèse et caractérisation d'un matériau de la structure pérovskites à base plomb, mémoire de master, univ Mohamed Khider-Biskra- Algérie. (2018).
- [10] Curie. J, Curie. P. Développement par compression de l'électricité polaire dans les cristaux hémièdres à faces inclinées. Journal of *Bulletin de minéralogie*, 3(4), 90-



- 93. (1880).
- [11] Million. C. Contributions à l'étude de procédés de réalisation de structures métal/PZT/métal sur silicium pour microsystèmes piézoélectriques, thèse doctorat, univ de Lyon-France. (2003).
- [12] Meklid. A. Etude de la transition de phase de la solution solide de céramiques piézoélectrique dans le système ternaire : (0.80-x) Pb (Cr_{1/5}, Ni_{1/5}, Sb_{3/5}) O_{3-x} PbTiO₃-0.20PbZrO₃, mémoire de magistère, univ Kasdi Merbah -Ouargla Algérie. (2011).
- **Khacheba.M.** Elaboration et caractérisation diélectrique de céramiques de formule : A_x (Y_{0,5}, N / A_{0,5})_{1-x} [(Zr_{0,05}, Ti_{0,95})_{0,97}(A_{11/3}, Zn_{1/2}, W_{1/3})_{0,03}] (A=Pb, Ba), thèse de doctorat, univ Mohamed Khider-Biskra-Algérie. (2023).
- [14] Haussonne.J. M. Céramiques pour l'électronique et l'électrotechnique. EPFL Press. (2002).
- [15] Eyraud. L. Diélectriques solides, anisotropes et ferroélectricité. Feni XX. (1967).
- **BENAYAD.A.** Matériaux monocristallins à forte activité piézoélectrique : élaboration, caractérisation et application, thèse de doctorat, univ de Lyon-France. (2005).
- **KOBOR.D.** Synthèse dopage et caractérisation de monocristaux ferroélectriques type PZT-PT par la méthode du flux, thèse de doctorat, univ de Lyon -France. (2005).
- [18] Zheludev.I. S. Ferroelectricity and symmetry. In *Solid state physics* (Vol. 26, pp. 429-464). Academic Press. (1971).
- [19] Moulson. A. J, Herbert.J. M. Materials, properties, applications. Chapman & Hall. (1996).
- [20] Benabdallah. F. Evolution des propriétés diélectriques, ferroélectriques et électromécaniques dans le système pseudo-binaire (1-x) BaTi_{0.8} Zr_{0.2} O_{3-x}
 Ba_{0.7} Ca_{0.3} TiO₃ /Corrélations structures et propriétés, thèse de doctorat, univ Bordeaux 1 & univ de Sfax Tunisie. (2013).
- [21] Meklid. A. Elaboration, caractérisation et étude des propriétés diélectriques et électromécaniques d'un nouveau matériau de céramique de type Zirconate- Titanate de plomb (PZT), thèse de doctorat, Univ Mohamed Khider-Biskra- Algérie. (2018).





[22] Hachemi. F.A. Effect of doping and sintering temperature on the structural properties of a dielectric ceramic, mémoire de master, univ Mohamed Khider - Biskra- Algérie. (2024).

Chapter I

- [23] MAHBOUB. Ch, ROUAG. R. Synthèse et caractérisation structurale d'une solution solide de type PZT dopée, mémoire de master, univ Mohamed Khider Biskra- Algérie. (2020).
- [24] Tanabe. Ni. L, Irie. M. H. A visible-light-induced overall water-splitting photocatalyst: conduction-band-controlled silver tantalate. *Journal of Chemical communications*, 49(86), 10094-10096. (2013).
- [25] Liu.X et al. A novel contractive effect of KTaO₃ nanocrystals via La³⁺ doping and an enhanced photocatalytic performance. *Journal of Alloys and Compounds*, 622, 894-901. (2015).
- **Parida. K. M et al.** Fabrication of nanocrystalline LaFeO₃: An efficient sol–gel auto-combustion assisted visible light responsive photocatalyst for water decomposition. *International journal of Hydrogène Energy*, *35*(22), 12161-12168. (2010).
- [27] Feng. Y. N et al. Ferromagnetic and photocatalytic behaviors observed in Cadoped BiFeO3 nanofibres. *Journal of Applied Physics*, 113(14). (2013).
- [28] Guesmia.V, Saadi.V. Elaboration et Caractérisation Des Oxydes de Type Pérovskite XFeO₃ Dopés, mémoire de master, univ Mohamed Khider-Biskra-Algérie. (2021).
- [29] Hattna. S, Hachani. Ch. Synthèse et caractérisation d'un nouveau matériau sans plomb, mémoire de master, univ Mohamed Khider-Biskra- Algérie. (2020).
- [30] Meguellati. I, BAKHTI. A. Les composés de type BNT, méthodes de synthèse, propriétés et domaines d'application, mémoire de master, univ Mohamed Khider-Biskra- Algérie. (2022).
- [31] **Dorcet.V.** Etude de la relation entre structure et propriétés des pérovskites pseudocubiques du système Na _{0.5} Bi _{0.5} TiO ₃ Bi Fe O₃, thèse de doctorat, univ de Limoges. (2008).
- [32] Sung. Y. S et al. Effects of Na nonstoichiometry in (Bi_{0. 5} Na_{0. 5+ x}) TiO₃ ceramics. Journal of *Applied Physics Letters*, 96(2). (2010).
- [33] Hiruma. Y et al. Thermal depoling process and piezoelectric properties of bismuth





sodium titanate ceramics. Journal of applied physics, 105(8). (2009).

Chapter I

- [34] Nagata. H et al. Developments in dielectric materials and electronic devices. *Ceramic Transactions*, 167, 213-221. (2004).
- [35] Zhou. Z. H et al. Leakage current and charge carriers in (Na_{0.5}Bi_{0.5}) TiO₃ thin film. *Journal of Physics D: Applied Physics*, 38(4), 642. (2005).
- [36] Takenaka.T et al. Phase transition temperatures and piezoelectric properties of (Bi 1/2 Na 1/2) TiO₃-and (Bi 1/2 K 1/2) TiO₃-based bismuth perovskite lead-free ferroelectric ceramics. *Journal of IEEE transactions on ultrasonics, ferroelectrics, and frequency control*, 56(8), 1595-1612. (2009).
- [37] Yan. H et al. The dependence of the piezoelectric properties on the differences of the A-site and B-site ions for (Bi_{1-x}Na_x) TiO₃-based ceramics. *Materials & design*, 26(5), 474-478. (2005).
- [38] GADI. F.Z. Etude structurale et les propriétés électriques d'un matériau composite à base PZT-Al₂O₃, mémoire de master, univ Mohamed Khider Biskra-Algérie. (2015).
- [39] **Djedjiga. L.** Etude et optimisation des cellules solaires en couches minces CdTe/CdS, mémoire de master, univ Mouloud Mammeri Tizi-Ouzou -Algérie. (2016).
- [40] **Djeghidel. Ch, Sam. H.** Étude de pérovskites semi-conductrices et leur application dans le domaine de capteurs de gaz : le composé La_{1-x} M_x FeO₃ dopé, mémoire de master, univ Mohamed Khider Biskra-Algérie. (2021).
- [41] Mahboub.W. L'effet de dopage sur la structure de la composition pérovskite (Bi_{0.5} Na _{0.5}) Ti O₃, mémoire de master, univ Mohamed Khider Biskra-Algérie. (2019).
- **Kell. R. C.** High-permittivity temperature-stable ceramic dielectrics with low microwave loss. *Journal of the American Ceramic Society*, 56(7), 352-354. (1973).
- [43] Bounab. K. Elaboration, caractérisation et étude des propriétés diélectriques d'une solution solide de type PZT, thèse de doctorat, univ Mohamed Khider– Biskra-Algérie. (2015).
- [44] Lines. M. E, Glass. A. M. Principles and applications of ferroelectrics and related materials. Oxford university press. (2001).

Chapiter II:

Experimental Techniques





II.1. Introduction

This chapter first presents the synthesis and shaping techniques used to prepare ceramics with a perovskite structure, with particular emphasis on BNT. It then describes the physicochemical characterisation techniques used to analyse its chemical, structural, microstructural and electrical properties.

The growing interest in lead-free ferroelectric materials, particularly BNT and its derivatives, has led to the development of various synthesis methods tailored to their specific properties. The choice of manufacturing technique depends not only on the composition of the material, but also on its final state (grain size, porosity, surface finish, homogeneity, etc.), particularly on an industrial scale. To save energy and optimise performance, low-temperature synthesis methods are preferred.

Among the various approaches, the molten salts method stands out as an effective alternative for the preparation of BNT. Unlike the traditional ceramic method based on solid-phase reaction, this technique significantly lowers the synthesis temperature by using salts as melting agents.

The process for making BNT using this method involves several essential steps:

- ♣ Preparation of the mixture of precursors and melting salts.
- ♣ Heat treatment to induce the BNT-forming reaction.
- **♣** Washing and removal of residual salts.
- ♣ Characterisation and shaping of the final material.

Powder preparation and control of heat treatment conditions are critical parameters in this process. The purity, morphology and particle size distribution of the powder obtained directly influence the final properties of the BNT, as do the choice of melting salts and calcination parameters.

This approach makes it possible to obtain well-crystallised, homogeneous powders of controlled size, while reducing energy consumption compared with conventional methods.



II.2. The Molten Salt method

Molten salt' is any ionic medium made up of inorganic anions and cations between which strong electrostatic interactions hold the liquid together [1].

Molten salt synthesis, one of the methods for preparing ceramic powders, involves using a molten salt as a medium to prepare complex oxides of their constituent materials (oxides and carbonates). Salt with a low melting point is added to the reactants and heated above the melting point of the salt [2]. The molten salt acts as a solvent instead of water to form the oxide [3].

In molten salt synthesis, a large amount of salt is used as a solvent to control powder characteristics (size, shape, etc.). Typical examples of salts used in molten salt synthesis are chlorides and sulphates [2]. In many experiments, the eutectic composition (0.5 NaCl - 0.5 KCl) of a salt mixture is often used and has a lower temperature than the liquid formation temperature. While the melting point of NaCl and KCl is 801 C° and 770 C°, for the eutectic composition it is 650 C° [4].

II.2.1. The advantages of the molten salt synthesis MSS

Simplicity:

The MSS process can be easily carried out in a simple laboratory with basic facilities. No sophisticated instrumentation is needed. Precursors and molten salts are air stable with no need for glove box handling [5].

Reliability:

Once all initial synthesis parameters such as concentration, pH, processing time, and annealing temperature are optimized, high-quality and pure products are assured when using the MSS method [5].

Scalability:

The MSS method's ability to produce large quantities of size- and shape-controlled particles is crucial. This critical factor is important because it allows for the determination of industrial usefulness and efficiency. Compared to other synthesis techniques, MSS can easily generate a



sufficient amount of products by adjusting stoichiometric amounts during the process. This is an important feature of the method because it allows for convenience at the industrial level, making it a more desired approach due to this scalability [6,7].

Generalizability:

The MSS method is also a generalizable technique to produce nanoparticles with various compositions. Other than simple metal oxides and some fluorides, nanomaterials of complex metal oxides that have been successfully synthesized by the MSS method include perovskites (ABO₃) [5]. More specifically, these nanomaterials include ferrites, titanates, niobates, mullite, [8,6,9]. The MSS method has also been used to produce nanomaterials of various morphologies such as nanospheres, ceramics powder bodies, nanoflakes, nanoplates, nanorods, and core-shell nanoparticles, depending on synthesis conditions and crystal structure of the products [5].

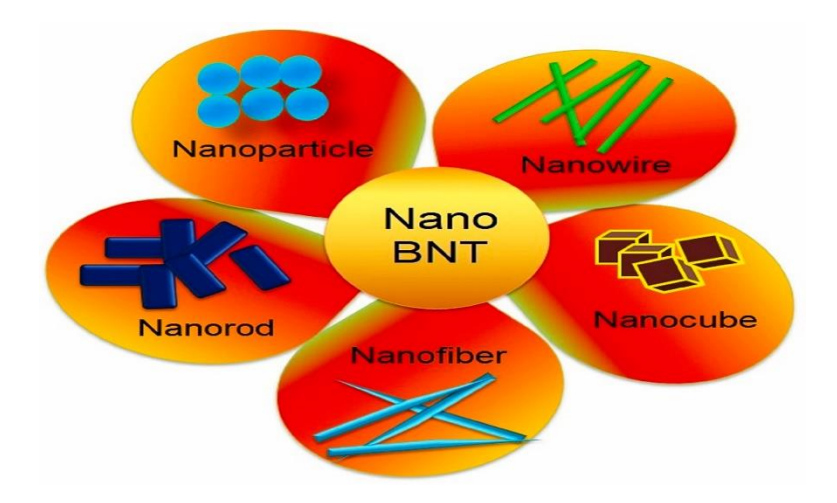


Figure II .1: Generalizability of the Molten Salts Synthesis Method in Nanomaterial Morphologies

Environmental friendliness:

Several traditional methods for making nanomaterials involve the use of large amounts of organic solvents and toxic agents that generate environmental issues. The partial or total elimination of the use of them and the generation of waste by sustainable processes is in demand of green chemistry nowadays [10]. The MSS method is an environmentally friendly approach



to synthesize nanomaterials by employing nontoxic chemical and renewable materials and minimizing waste, byproducts, and energy [5].

♣ Relative low synthesis temperature:

The MSS method has a low processing temperature compared to conventional methods. This helps save energy during the preparation process while producing high quality nanoparticles.

♣ Cost effectiveness:

The MSS method does not require any harsh or costly reactants or solvents nor any specialized instrumentation. Water is the main solvent used for washing away the used molten salts, which are also cheap. Moreover, experimental setup needed includes only simple glassware and a furnace without specialized instrumentation, while nanomaterials with complex composition and refractory nature can be produced [5].

II.2.2. The important purpose of using molten salts synthesis

- ♣ To prepare powders for sintering.
- **♣** To prepare an isometric particle [11].

II.2.3. The role of molten salts

- ♣ To increase the reaction rate and lower the reaction temperature.
- ♣ To increase the degree of homogeneity (the distribution of constituents in the solid solution).
- **♣** To control the particle size.
- **♣** To control the shape of the particle.
- **♣** To control the state of agglomeration [11].

II.3. Experimental procedure

II.3.1. Starting products

Our BNT solid solution is prepared from a mixture of starting products (base oxides and dopants).



II.3.1.1. Base oxides

The base oxides used in the synthesis of our samples are: Bi₂O₃, Na₂CO₃, TiO₂.

♣ Bismuth (III) oxide Bi₂O₃



Figure II.2: Bismuth trioxide powder

Bismuth trioxide, with the formula Bi₂O₃, is a yellow crystalline powder (fig II.2). The most stable degree of oxidation of bismuth is degree (III) Bismuth oxide (Bi₂O₃) has several allotropic varieties (phases) Their main crystallochemical characteristics are presented in (Table II.1).



Table II.1: The main crystallochemical characteristics of Bismuth trioxide Bi_2O_3

The phase	System	Mesh parameters (Å)
α-Bi ₂ O ₃	Monoclinic	a = 5.83 Å, b = 8.14 Å,
		c = 13,78 Å
		And $\beta = 113^{\circ}$
β-Bi ₂ O ₃	Tetragonal	a = 10,93 Å
		c = 5,62 Å
γ-Bi ₂ O ₃	Cubic centred	a = 10,08 Å
δ-Bi ₂ O ₃	Face-centred cubic	a= 5,53 Å
w-Bi ₂ O ₃	Triclinic	a =7,268Å, b = 8,639Å,
		$c = 1 1,969 \text{ Å, And } \alpha =$
		87,71°, β= 93,22°γ= 86,65°
ε-Bi ₂ O ₃	Orthorhombic	a = 4,955 Å, b = 5,585 Å,
		c = 1 2,729 Å

♣ Sodium carbonate Na₂CO₃



Figure II.3: Sodium carbonate powder



Sodium carbonate Na₂CO₃ is an inorganic compound with a molar mass of 105.99 g/mol. It appears as a white (fig II.3), odorless powder and is highly soluble in water. It crystallizes in the monoclinic crystal system. It has a melting point of 851°C and a boiling point of approximately 1600°C. The density of anhydrous sodium carbonate is 2.54 g /cm³.

Titanium dioxide TiO2



Figure II.4: Titanium dioxide powder

This is a white powder when cold and yellow when hot. It has a melting point of 2000°C and a boiling point of 3000°C. The rutile TiO_2 has a quadratic structure and parameters a=4.59 Å and c=2.96 Å [12].

II.3.1.2. Dopants

The ABO₃ perovskite structure of BNT was chosen as the basis for this study. The dopants at site B are fixed, while at site A, Sm_2O_3 is introduced in different proportions with x=0.00;0.02;0.04;0.06.



II.3.1.2.1. Doping at site A

♣ Samarium oxide Sm₂O₃



Figure II.5: Samarium oxide powder

Samarium oxide Sm_2O_3 is a white powder (fig II.5), a high-k dielectric rare-earth sesquioxide, with a density of $8.43 \,\mathrm{g/cm^3}$, and melting and boiling points of 2335 °C and 4118 °C respectively [13] .

II.3.1.2.2. Dopings at site B

♣ Zirconium dioxide ZrO₂



Figure II.6: Zirconium dioxide powder



It is a white powder with good hardness (fig II.6), good thermal shock and corrosion resistance and low thermal conductivity [14].

It has a fluorite-type structure. The mesh is monoclinic with parameters a =5.14 Å, b = 5.20 Å, and c = 5.21 Å, β = 80, 45°.It Presents a melting point at 2677°C and a boiling point at 3500°C [15].

♣ Zinc oxide ZnO



Figure II.7: Zinc oxide powder

It is a white powder with a ZnO molar mass equal to 81.389 g/mol, a melting point of 1975 °C and a density of 5.642 g/cm³.

♣ Iron oxide Fe₂O₃



Figure II.8: Iron oxide powder



It is obtained by heating FeO (H_2O) to a temperature of 200°C, its colour is red-brown and it is used in low-temperature pastes and enamels [16].

♣ Indium oxide In₂O₃



Figure II.9: Indium oxide powder

Indium oxide In₂O₃ is a yellow powder with a molar mass of 277.633 g/mol. It has a high melting point of 1910°C, making it thermally stable. With a mass density of 7.18 g/cm³, it is relatively dense. Indium oxide is insoluble in water.

II.3.2. Powder preparation

II.3.2.1. Weighing and mixing

The starting powders are weighed and mixed in stoichiometric quantities according to the reaction equation. This mixing can be done in an acetone medium in a beaker, and the powder from the mixture is homogenised using a magnetic stirrer for 7 hours. The paste obtained was then dried at 110°C in an oven for 3 hours. Finally, the powder is ground in a glass mortar for 30 minutes to obtain a fine granulometry. It should be noted that we chose acetone because it has a low evaporation point, which makes drying easier, and also because it does not react with any of the products in the mixture.

II.3.2.2. Grinding with salts

The obtained powder was mixed with a large amount of NaCl and KCl and ground for 3 hours and 30 minutes in a glass mortar.





Figure II.10: Grinding in a glass mortar

♣ Sodium chloride NaCl



Figure II.11: Sodium chloride

Sodium chloride is a white powder with a melting point of 801 °C and a boiling point of 1413 °C. Its mass density is 2.16 g/cm³. It is soluble in water.



4 Potassium chloride KCl



Figure II.12: Potassium chloride

Potassium chloride is a white powder with a melting point of 770 °C and a boiling point of 1420 °C. Its mass density is 1.98 g/cm³. It is soluble in water.

II.3.2.3. Heat treatment

Heat treatment, also called calcination, is carried out at around 900°C for four hours in a programmable furnace with a heating rate of 2°C/min. Calcination is used to form the perovskite phase.

For this purpose, the samples are placed on a ceramic plate and subjected to a thermal cycle during which, through solid-phase diffusion phenomena, they react and form the desired phase [17].





Figure II.13: Programmable furnace for calcination

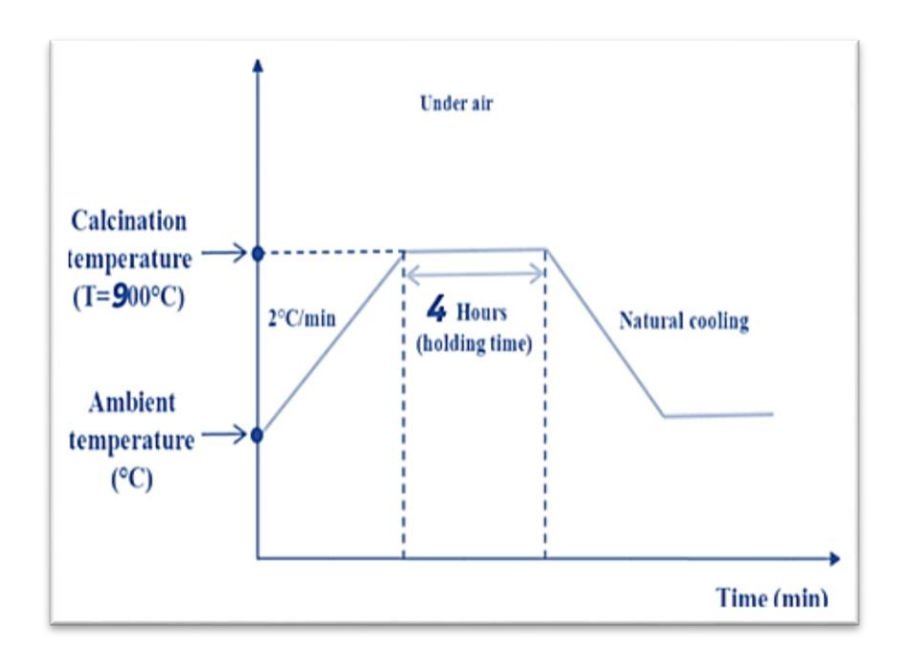


Figure II.14: Thermal cycle of the calcination process



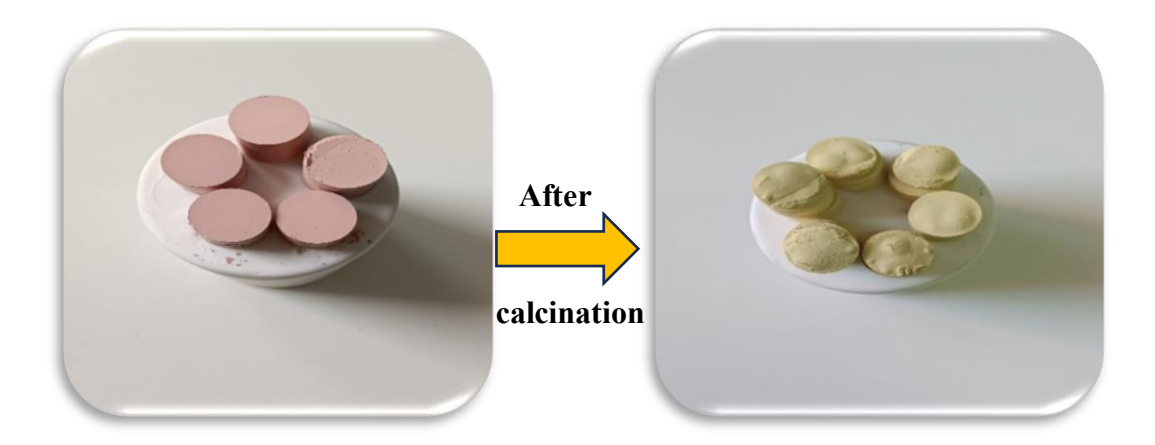


Figure II.15: Transformation of powder before and after heat treatment II.3.2.4. Grinding and drying procedure of pellets

We ground the pellets by adding a small amount of hot water to facilitate the process, then dried them completely in an oven at 110°C. After that, they were ground for 20 minutes to ease the washing process.

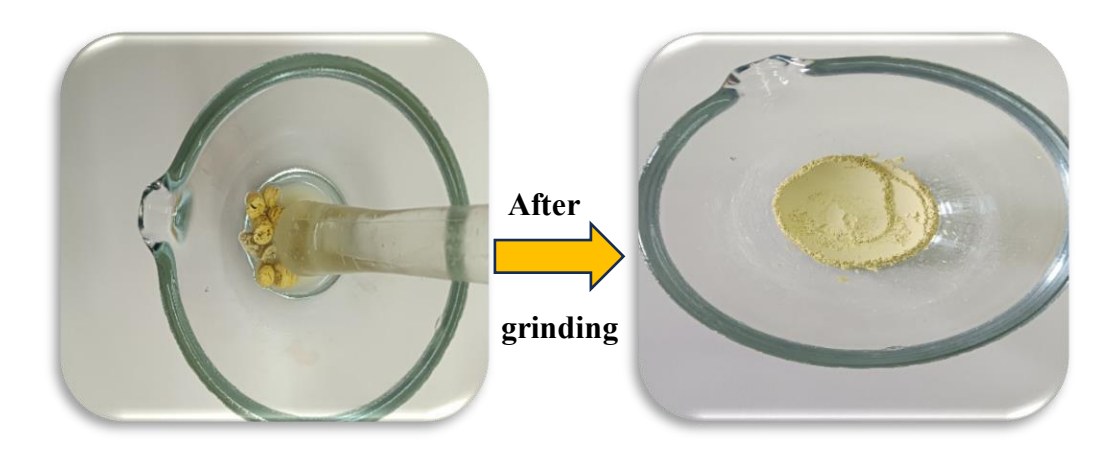


Figure II.16: Pellets before and after grinding process

II.3.2.5. Salt washing

After heating, the product mass is washed with a suitable solvent to remove the salt. In general, this is water, which means that water-soluble salts are generally used in the synthesis of molten salts. The solubilities of chlorides and sulphates are generally high and washing with water two or three times seems sufficient to remove all the salt. However, dissolved salt ions



can adsorb onto the surfaces of product particles, in which case repeated washing is necessary. Chloride ions are sometimes detected by an Ag⁺ (Silver nitrate) solution even after ten washes.

To desorb the ions effectively, we recommend using hot water rather than cold water. After washing, the supernatant water is decanted and the remaining powder is dried [11].



Figure II.17: Salt washing process for removing dissolved salts

II.3.2.6. Drying

This stage consists of drying the mixture obtained at a temperature of 95°C for four hours in an oven until the water evaporates. The compounds are again in powder form.



Figure II.18: Oven drying



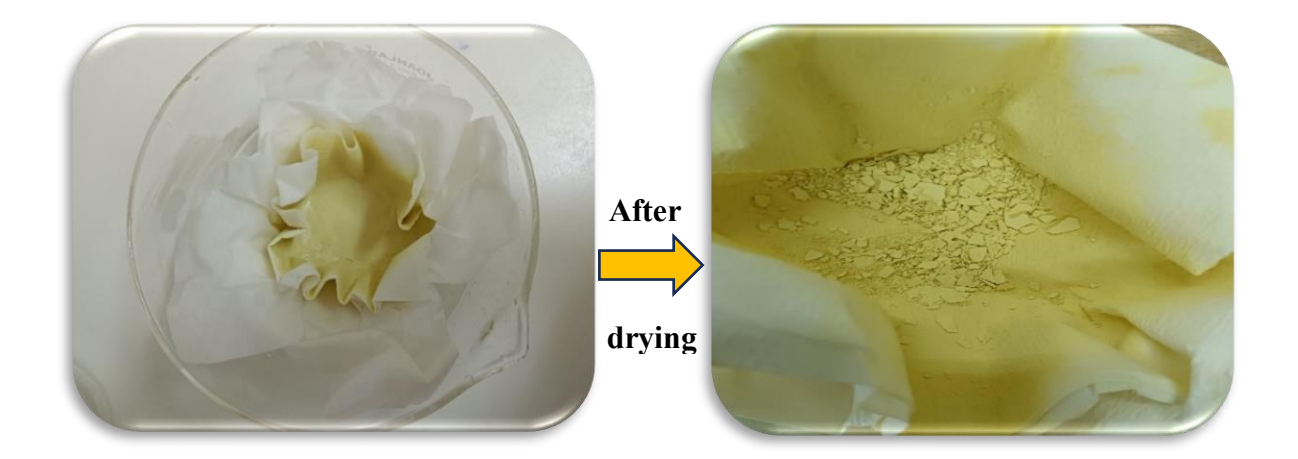


Figure II.19: Powder before and after drying

II.3.2.7. Regrinding

Ce broyage est réalisé dans les mêmes conditions de premier broyage, pendant 4 heures. La poudre est rebroyée afin de réduire la taille des grains, de l'homogénéiser et d'augmenter sa réactivité [3].



Figure II.20: Regrinding of the powder in a glass mortar

II.3.2.8. Shaping

The samples are shaped under uniaxial pressure of 1.1g powder weight at 3000Kg/cm² using a hydrostatic press. The samples then take on cylindrical shapes of fixed diameter 13 mm and variable thickness depending on the force applied [15].



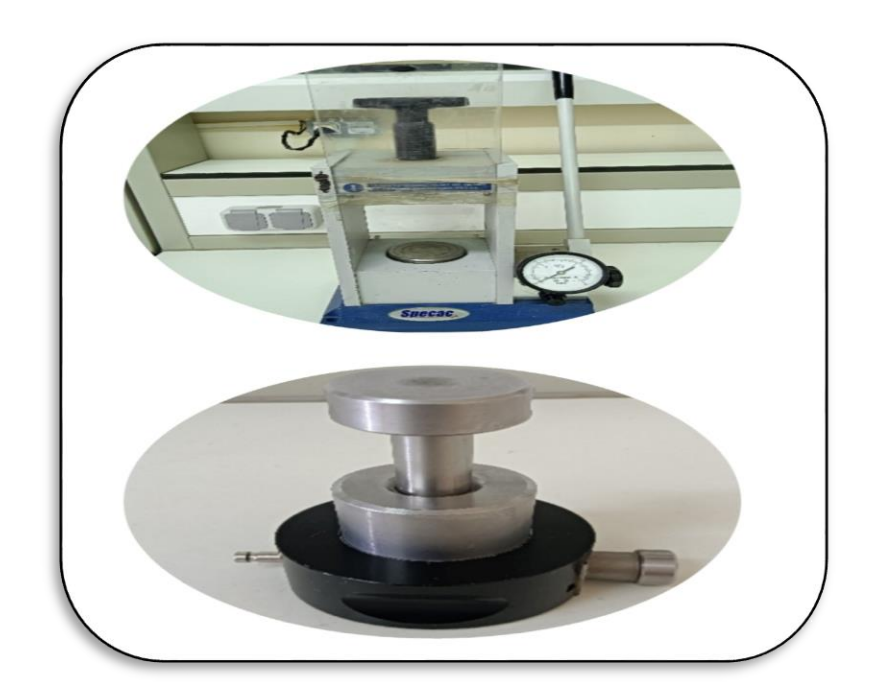


Figure II.21: The hydrostatic press used to prepare the pellets



Figure II.22: Pellets before sintering

II.3.2.9. Sintering

Sintering, a generic term encompassing all the physical processes that enable a powdery material to become a material with a certain mechanical strength, can in some cases take place naturally without the action of an external constraint, simply by increasing the temperature [18]. Sintering is defined as the heat-induced consolidation of a more or less compact granular agglomerate, with or without fusion of one or more components [15].



Sintering samples is a delicate operation, depending essentially on two parameters: temperature (kinetic and palpy) and sintering atmosphere. These two parameters have a direct influence on the density, grain size and compositional homogeneity of the material [17].

The aim of this heat treatment is to complete the formation of the crystalline phase and allow the ceramic to condense. This process involves heating the material to a high temperature, but below the melting temperature. The aim is to grow the bonds between the grains leading to cohesion and size reduction. The selected sintering temperatures are 1000°C, 1050°C, 1100°C and 1150°C at a heating rate of 2°C/min for 4hours.

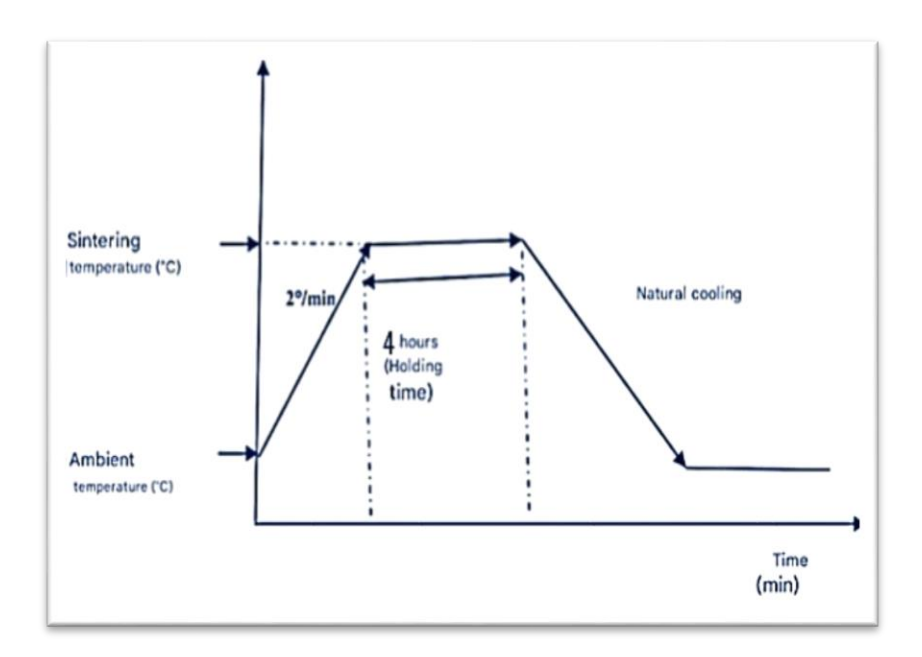


Figure II.23: Schematic diagram of sintering cycles



II.4. Structural characterisation techniques for calcined powders and sintered ceramics

II.4.1. Study of the structure by X-ray diffraction

X-ray diffraction is considered to be a key technique for resolving crystalline structures due to its high sensitivity to changes in the elemental lattice of crystals or polycrystalline materials.

Sample preparation seems to be one of the essential parameters for obtaining good quality, reproducible results, as the three main pieces of information obtained from diffraction data are influenced by the sample $[\underline{19}, \underline{20}]$:

- The position of the lines.
- **4** The intensity of the lines.
- **♣** The shape of the lines.

Figure II.24 shows a schematic representation of a powder diffractometer with a Bragg-Brentano reflection arrangement, used to measure the angles at which diffraction occurs in the case of pulverised samples. A sample in the form of a solid plate rests on a support so that it can rotate on its axis, which is perpendicular to the plane of the page.

A beam of monochromatic X-rays is projected from the X-ray source and the intensity of the diffracted beams is measured using a detector. The sample, X-ray source and detector are all coplanar.



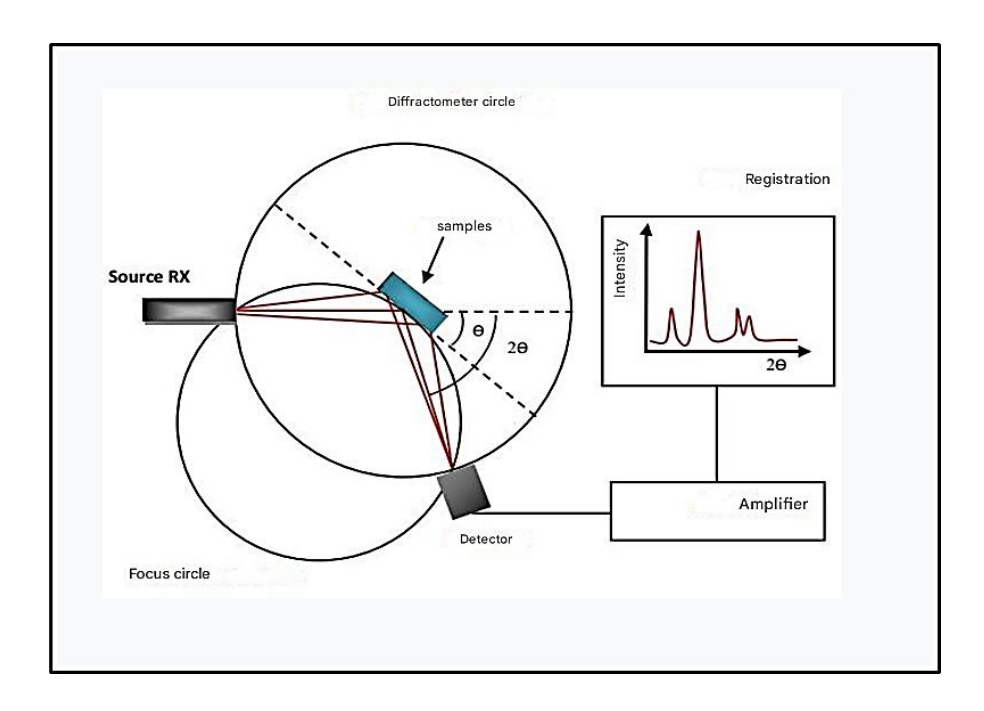


Figure II.24: Diagram showing the main components of an automatic diffractometer

In the so-called 2θ configuration, the X-ray tube and detector move symmetrically, each making a (variable) angle θ with the horizontal surface of the sample. When an angle corresponding to a family of planes (hkl) under Bragg conditions is reached, the detector registers an increase in diffracted intensity. Diffractograms (I= f (2θ)) are then obtained and compared with the X-ray diffraction spectra of powdered reference materials in the Joint Committee on Powder Diffraction Standards (JCPDS crystallographic database), to determine the phase or phases under which the sample crystallised. Bragg's law is an empirical law that accounts for the constructive interference between the scattered beams. Which the diffraction maxima are observed [21]:

$$2. d_{hkl} . sin\theta = n. \lambda$$
 Eq. II.1

d_{hkl}: the characteristic reticular distance of the atomic planes (hkl).

n: interference order (integer).

 λ : the radiation wavelength.

θ: the angle of incidence of the X-rays on the reticular plane (hkl).



Experimental set-up

Radio crystallographic analysis of the samples at room temperature was carried out using a (XRD, PANalytical EMPYREAN) diffractometer. This diffractometer is characterised by X-rays that were produced from a Cu K α radiation source with a wavelength λ =1.540598 Å, within an angular range of 10° to 80°, in steps of 0.02°.



Figure II.25: X-ray diffractometer: XRD, PANalytical EMPYREAN.

II.4.2. Measurement of density (d)

The density of ceramics is defined as the mass per unit volume. The quality of the material increases as the density increases, and the density increases as the sintering temperature increases [22].

The structural and physical properties of a ceramic are related to its density.

To determine the optimal sintering temperature, specific samples were selected for density analysis. Geometric measurements, including the diameter and thickness of each pellet, were carried out. The samples were analyzed at four different temperatures: 1000, 1050, 1100, and 1150°C. These measurements were performed using a caliper to ensure optimal precision.



The density (d) is calculated by the formula:

$$d = \frac{m}{\pi (\frac{\phi}{2})^2 e}$$
 Eq. II.2

Where:

m: Mass of the pellet (g).

φ: Pellet diameter (cm).

e: Pellet thickness (cm).

II.4.3. Measurement of porosity (P)

The mechanical properties of ceramics are influenced by porosity, so the point of studying porosity is to obtain less porous ceramic samples with good mechanical properties.

Porosity is calculated as follows:

$$P = 1 - d Eq. II.3$$

And

$$d = \frac{d_{exp}}{d_{th\acute{e}}}$$
 Eq. II.4

dexp: Experimental density of composition (g/cm³).

d_{th}: Theoretical density of composition (g/cm³).

The theoretical density of the material is obtained from geometric measurements, while the experimental density is obtained from the results of X-ray diffraction providing the lattice parameters.

$$d_{exp} = \frac{m}{\pi (\frac{\phi}{2})^2 e}$$
 Eq. II.5

With:

m: Mass of the pellet (g).

φ: Pellet diameter (cm).

e: Pellet thickness (cm).

$$d_{th\acute{e}} = \frac{MZ}{VN}$$
 Eq. II.6

With:

M: Molar mass of the sample.

Z: Number of form units per mesh.

N: Avogadro number.

V: Mesh volume.

II.4.4. SEM analysis

Principle of the analysis

Scanning electron microscopy (SEM) is an analysis technique based on electron-matter interactions, enabling high-resolution images to be produced of the surface or slice of a sample.

Experimental set-up

It works as follows: in a vacuum chamber, a beam of electrons accelerated by an electric field and focused by magnetic lenses scans the surface of the sample, which in response emits secondary, backscattered Auger electrons and X-rays. Because of their low energies (around 50 eV), secondary electrons (SE) are emitted in the surface layers close to the surface. They can be easily deflected with a low potential difference and collected by the detectors to form a topographic image of the sample surface. (the shape, grain size and microporosity of ceramics) at a wide range of magnifications. Backscattered electrons (BSE) are electrons that result from the quasi-elastic interaction of electrons in the primary beam with the nuclei of atoms in the sample and are re-emitted in a direction close to their original direction. They have a relatively



high energy, much higher than that of secondary electrons (up to 30 keV). This type of electron is generally sensitive to the atomic number of the atoms making up the sample. Indeed, areas formed by heavy atoms have the particularity of re-emitting more electrons than those formed by light atoms and therefore appear brighter. This is known as chemical contrast or atomic number. Backscattered electrons can therefore provide images for qualitative chemical analysis of a sample (chemical homogeneity) [23].

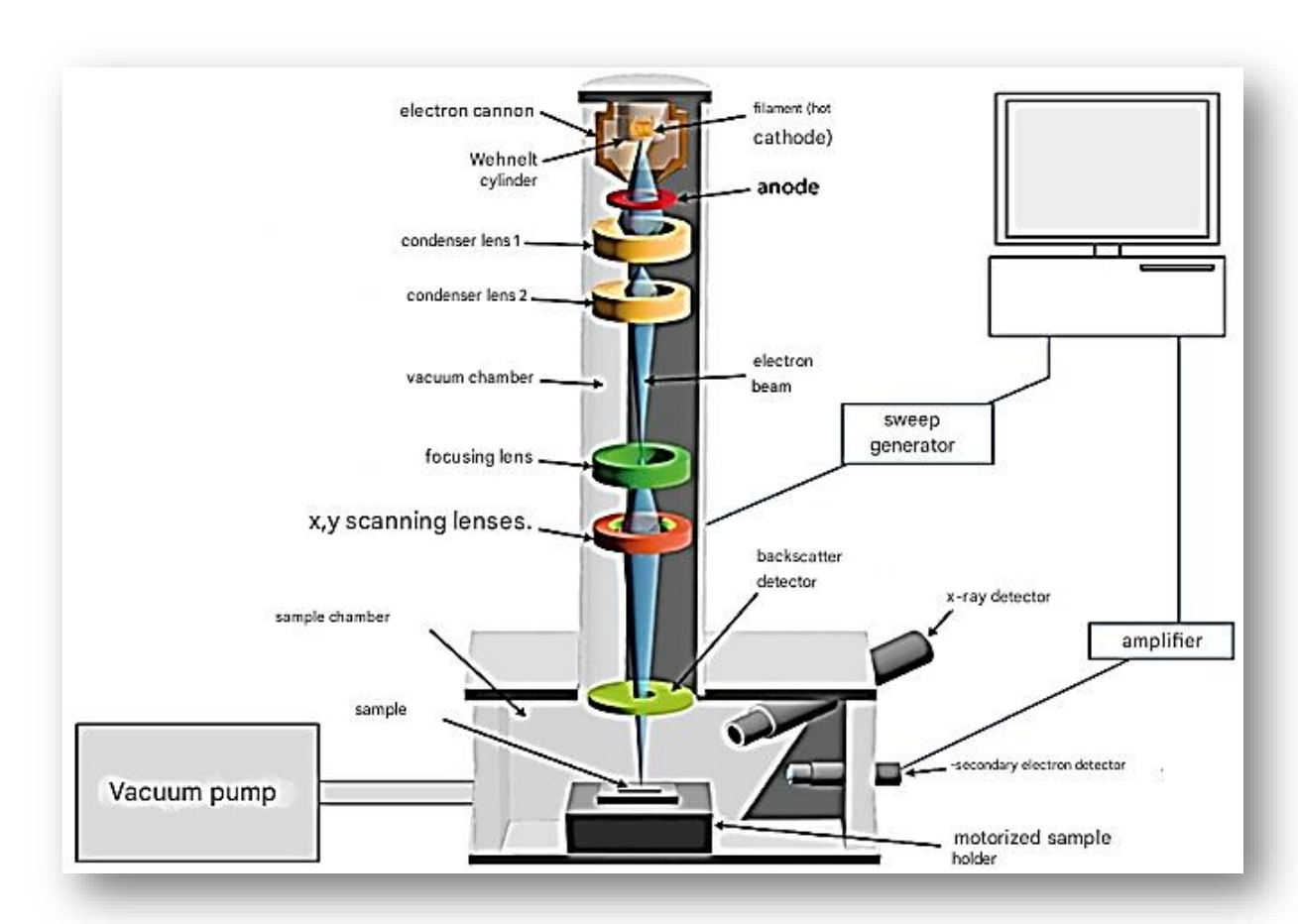


Figure II.26: Main components of a scanning electron microscope

II.4.5. FTIR analysis

Principle of the analysis

Fourier Transformed Infra-Red Spectroscopy (FTIR) is based on the absorption of infrared radiation by the sample being analysed. In cramics with a perovskite structure, infrared absorption spectra can be used to identify the B-O and O-B-O bonds of the ABO₃ structure



[23,24], thus confirming the formation of the perovskite phase we are looking for. The physical quantity placed on the ordinate of these infrared spectra can be either the transmission:

$$T = I / I_0$$

Eq. II.7

or the absorbance:

Chapter II

$$A = -\log(T)$$

Eq. II.8

Where I₀ and I represent respectively the incident and transmitted intensities of the sample.

Experimental set-up

The samples to be analysed are in pellet form. They are prepared by mixing 0.2 g of KBr (dried) and 0.001 g of the sample, which is ground in an agate mortar and then compressed by a hydraulic press. A Agilent Cary 630 FTIR (Fourier Transform spectrophotometer) was used for simultaneous analysis in the wavelength range 400-4000 cm⁻¹.



II.5. Photocatalysis

II.5.1. Introduction

The contamination of water by pollutants of various origins is a topical problem. This contamination serves to upset the biological balance, making the water susceptible to environmental damage. They cause the loss of agricultural land and impact on flora and fauna. There are many pollutants that affect water quality. These include hydrocarbons, phenols, organic acids and dyes, all of which are toxic and have serious effects on the environment and on human beings. The textile industry significantly contributes to water pollution by consuming large amounts of water. It generates waste rich in recalcitrant organic molecules, leading to issues such as discoloration, high toxicity, and elevated conductivity.

These discharges pose enormous problems for human health and the environment because of their stability and low biodegradability. It is therefore necessary to treat these effluents before they are discharged into the sewer system.

To address this issue, photocatalysis emerges as a promising solution for eliminating organic pollutants from water. The principle of catalytic photodegradation is based on the natural phenomenon of photolysis, which occurs in the environment when the conditions necessary for photochemical reactions to take place are present [25].

II.5.2. Dyes

II.5.2.1. Definition of a dye

By definition, a dye is a strongly coloured substance that interacts with the medium into which it is introduced, colouring it by dissolving and dispersing. The medium into which it is introduced, colouring it by dissolving and dispersing.

According to Larousse, a dye is a coloured substance, natural or synthetic, which, when brought into contact with a support under appropriate conditions, fixes itself on the support in a durable manner, imparting a certain colour.



Dyes have the power to give a certain colour to a product. This colour is due to light waves. A compound appears coloured when it absorbs radiant energy corresponding to the visible spectrum (380 to 750 nm) [26].

II.5.2.2. Classification of dyes

Dyes can be classified according to a chemical classification or a functional classification.

- ♣ The chemical classification depends on the chemical structure of the dye, more precisely on the nature of its chromophore group.
- ♣ The functional classification is based on the mode of use and application of the dye, which in turn depends on its auxochrome group.

The common chromophores and auxochromes are summarized in Table II.2:

Table II.2: Main chromophore and auxochrome groups, ranked by increasing intensity

[26]

Chromophore groups	Auxochrome groups
Azo (-N=N-)	Amino (-NH ₂)
Nitroso (-NO or-N-OH)	Methylamino (-NHCH ₃)
Carbonyl (=C=O)	Di methylamino (-N(CH ₃) ₂)
Vinyl (-C=C-)	Hydroxyl (-HO)
Nitro (-NO ₂ or=NO-OH)	Alkoxyl (-OR)
Sulphide (>C=S)	Electron donor groups

II.5.3. Photocatalysis

II.5.3.1. Definition of photocatalysis

Photocatalysis or photocatalytic reaction is defined, as a chemical reaction induced by photo absorption of a solid material, or "photocatalyst," which remains chemically unchanged during and after the reaction. In other words, the solid acts catalytically, without any changes



in its composition or structure, under photoirradiation, and this explanation may be consistent with most other definitions [27].

II.5.3.2. Principles and mechanisms of photocatalysis

A catalyst is a substance that accelerates the rate of a chemical reaction without being consumed during the reaction [28]. In photocatalysis, photogenerated electrons are accelerated in the presence of a catalyst [29]. The International Union of Pure and Applied Chemistry (IUPAC) describes photocatalysis as a modification of the rate or initiation of chemical reactions under UV, visible or infrared (IR) irradiation in the presence of a photocatalyst that absorbs light and participates in the chemical transformation of the reactants in the reaction [30]. The light excites the photocatalyst and the reaction rate without consuming the photocatalyst [31]. Photocatalysis has a wide range of applications, from environmental remediation to medicine and processes leading to the degradation of various pollutants such as phenols, alkanes, alkenes, aromatics, pesticides, organic contaminants [31] and heavy metals [32].

The photocatalytic process using semiconductor materials (SC) involves various stages, as shown in Figure II.4. Photons whose energy is greater than or equal to the energy of the band gap (Eg) of a given SC photocatalyst are absorbed, creating electron-hole pairs (e⁻, h⁺). The electron (e⁻) migrates to the BV, leaving behind a complementary hole (h⁺) in the BC. The e⁻ and h⁺ created catalyse redox reactions at the surface of the photocatalysts, leading to the degradation of contaminants [33].



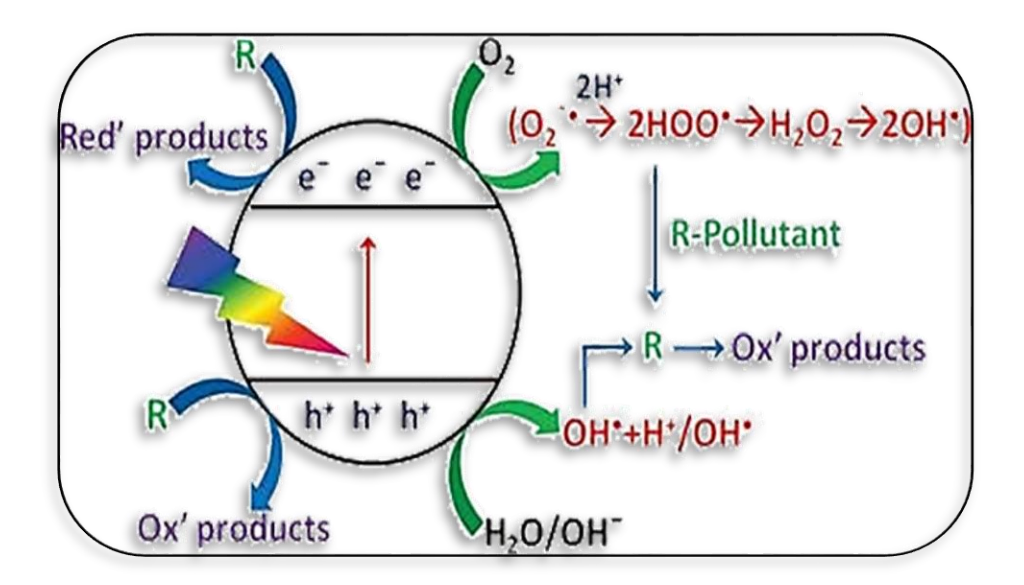


Figure II.27: Photocatalytic mechanism for environmental remediation applications

The positive holes can interact with electron donor species or OH radicals to form hydroxyl radicals (OH), which belong to the oxidising radicals, while the electrons react with oxygen to form superoxide radicals (O₂ -), potentially creating several reactive oxidation species (-OH, -O₂, H₂O₂, O₂). However, the main limitation of the process occurs when the photo-induced charge carriers recombine without participating in the reactions, i.e. when their lifetime remains negligible. Several approaches, such as doping, heterostructure or heterojunction formation, can be used to improve the lifetime of photogenerated charge carriers and overcome this limitation [34,35].

The redox reactions supported by a SC semiconducting photocatalyst follow reactions dedicated to the degradation of pollutants in water. These include,

Photocatalyser + photons (hv) = $e^- + h^+$	Eq. II.9
$\mathbf{O}_2 + \mathbf{e}^- = \mathbf{O}_2^-$	Eq. II.10
$\mathbf{H_2O} + \mathbf{h}^+ = \mathbf{OH}^\bullet + \mathbf{H}^+$	Eq. II.11
$\mathbf{OH}^{-} + \mathbf{h}^{+} = \mathbf{OH}^{\bullet}$	Eq. II.12
$O_2^- + 2H^+ + 2e^- = H_2O_2$	Eq. II.13



$$2e^{-} + H_2O_2 = OH^{*} + OH^{-}$$
 Eq. II.14

Pollutant $+ e^{-} =$ products (reduction) Eq. II.15

Pollutant + h^+ = products (oxidation) Eq. II.16

II.5.3.3 Factors affecting the efficiency of the photocatalytic process

Several factors influence the efficiency of the photocatalytic process

- **♣** pH
- **♣** Initial contaminant concentration
- **4** Radiation intensity
- Catalyst dosage

Photocatalytic reactions can be homogeneous or heterogeneous, depending on the medium used for the reactions.

- Homogeneous photocatalysis occurs when the catalyst and the reagent are in the same phase, for example the ozone and Fenton photo- systems [33].
- ♣ Heterogeneous photocatalysis means that the catalyst is solid, while the fluid medium in which it operates may be gaseous, liquid or even aqueous [36].

In this chapter, we use BNT photocatalysis to degrade two organic dyes: methylene blue and rhodamine.

A) Preparation of the solutions

A stock solution of each dye was prepared by dissolving 0.5 g of dye in a 1 L volumetric flask, giving a mass concentration of 0.5 g/L.

To obtain a dilute solution, 1 mL of the stock solution was taken and added to a 100 mL volumetric flask, giving the correct concentration for the experiment.



4 Methylene blue

Figure II.28: The chemical structure of methylene blue

Methylene blue dye is a cationic dye that exists as a dark green powder. It is commonly used as a model for organic contaminants because of its stable molecular structure.

Table II.3: Main physico-chemical characteristics of Methylene Blue

Chemical name	3,7-Bis (dimethyl amino) chloride Phenazathionium
Family	Basic dye
Solubility in water (g/l) at 20°C	40
λ _{max} (nm)	665-662
Melting point (°C)	180

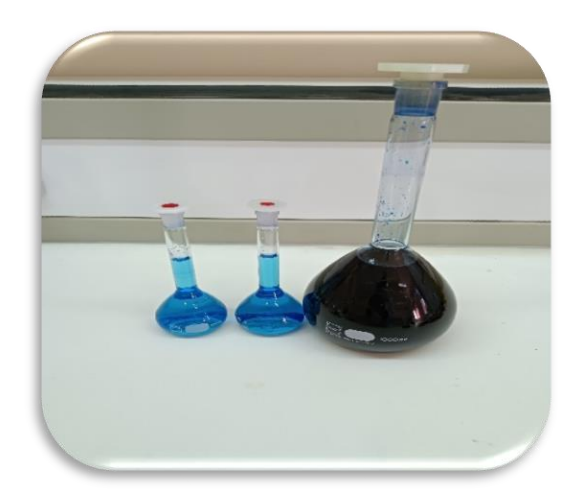


Figure II.29: Evolution of Methylene Blue before and after dilution



B) Conduct of the experiment

♣ Control (reference sample):

4 mL of the diluted solution was placed in a test tube, marked with the number 0 (control sample, without photocatalyst).

Contact with the photocatalyst:

0.1 g of BNT powder was weighed and added to the remaining diluted solution. The mixture was wrapped in aluminium foil and placed in a dark room under agitation for 30 minutes, to ensure adsorption of the dye molecules onto the surface of the catalyst in the absence of light.

A first sample (4 mL) was taken after this period and recorded as 1.

4 Exposure to light

The entire mixture was then exposed to sunlight under continuous agitation. Every 15 minutes, a 4 mL sample was taken and placed in a sequentially numbered test tube. A total of 14 test tubes were collected, corresponding to the different light exposure times.

This procedure makes it possible to assess the effectiveness of BNT as a photocatalyst by monitoring the degradation of the dyes as a function of time.

II.5.4. UV-visible spectroscopy

Principle

UV-visible spectrophotometry measures the amount of light absorbed at each wavelength in the ultraviolet and visible bands of the electromagnetic spectrum. The absorbance of light causes electrons to move from a lower energy level, the stable state, to a higher energy level in the excited state [37].



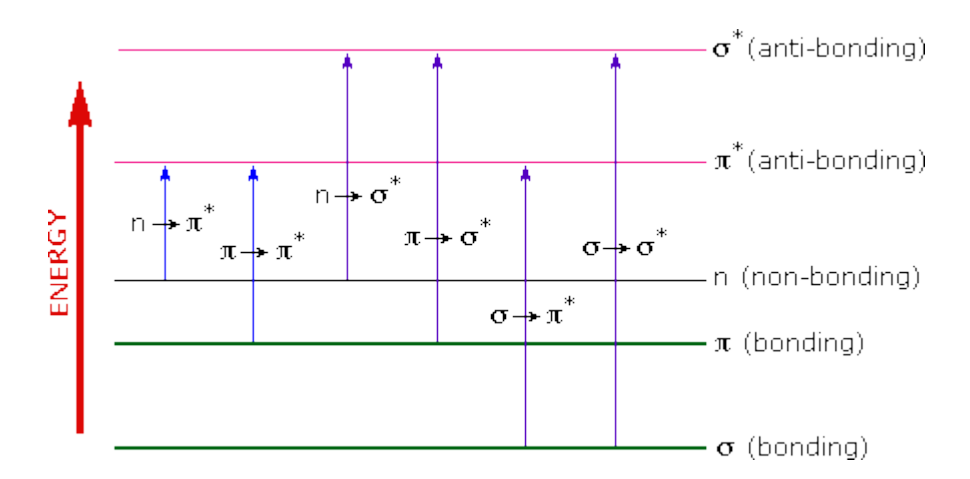


Figure II.30: Electronic transition states in UV-Visible spectroscopy

In a spectrophotometer, a beam of light passes through the sample and a detector measures the intensity before and after absorption (I_0 and I) at each wavelength. This is quantitative spectroscopy, governed by Beer-Lambert's law if the solution is sufficiently dilute:

$$A = Log I/I_0 = \varepsilon I c$$
 Eq. II.17

A: Absorbance.

ε: Absorbance coefficient (mol⁻¹. l.cm⁻¹).

I: Length of cell in cm.

C: Concentration of the solution in mol. L⁻¹.



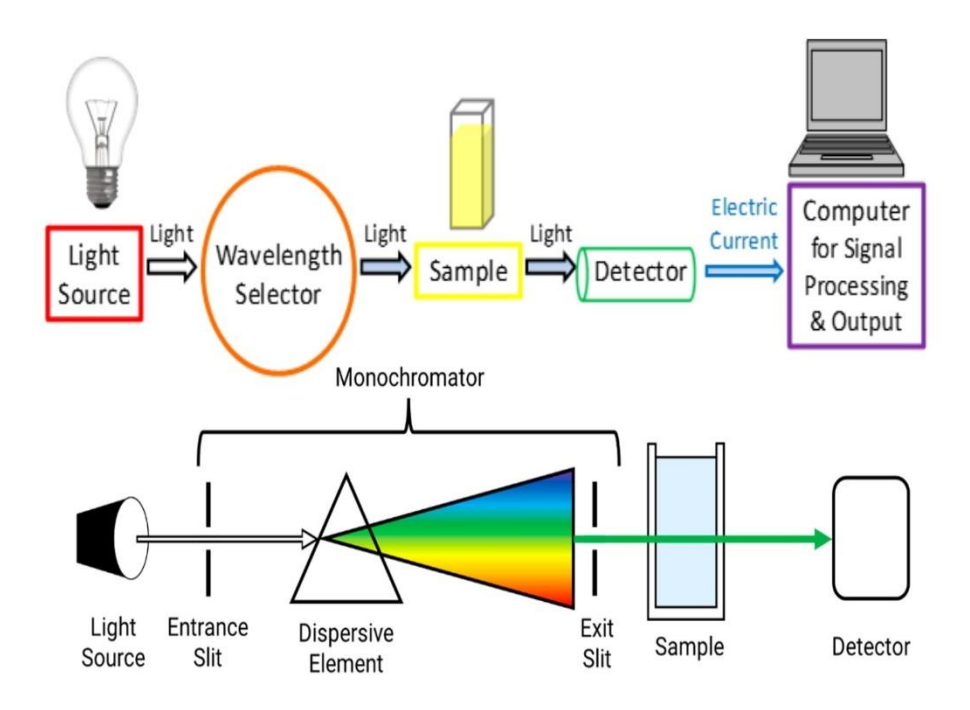


Figure II.31: Operating principle of the UV-Visible spectrophotometer

The UV-visible spectrum is made up of the absorbance curve as a function of wavelength: Log (I/ I_0) = $f(\lambda)$, λ being expressed in nm.

It takes the form of broad bands characterised by their wavelengths at the absorption maximum (λ_{max}) and their absorbance coefficients (ϵ)[37].

A) Optical absorption

In the process of optical absorption, the energy of an absorbed photon is transferred to an electron, causing it to move from the valence band (VB) to the conduction band (CB). The difference in energy between the top of the valence band (VBM) and the bottom of the conduction band (CBM) is defined as the band gap energy (Eg), often referred to as the 'gap'. Absorption only occurs when the energy of the photon (hv) exceeds the band gap energy (Eg) [38].



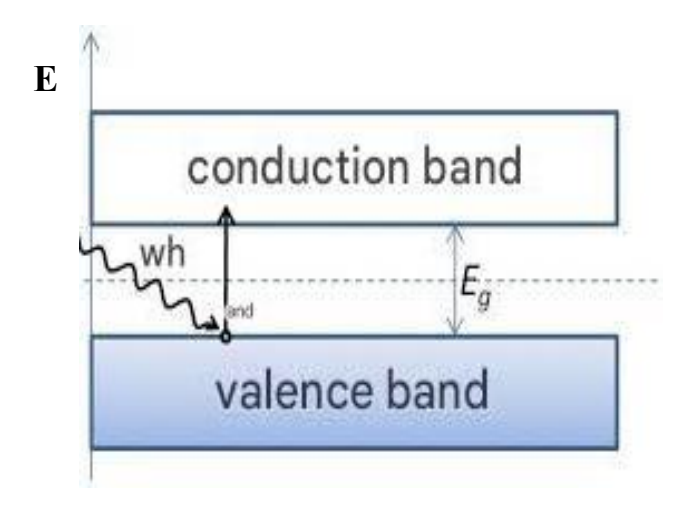


Figure II.32: Optical absorption between the occupied valence band and the unoccupied conduction band

B) Optical Gap

The concepts of direct and indirect gaps in a semiconductor are associated with the representation of energy dispersion, illustrated by the diagram E = f(k), which shows how the energy (E) varies as a function of the wave vector k. This diagram is used to define the conduction and valence bands, where two types of gaps are observed:

- **♣ Direct Gap**: The minimum of the conduction band and the maximum of the valence band coincide in terms of the wave vector.
- **↓ Indirect gap:** the minimum of the conduction band and the maximum of the valence band are not aligned (different wave vectors) [38].



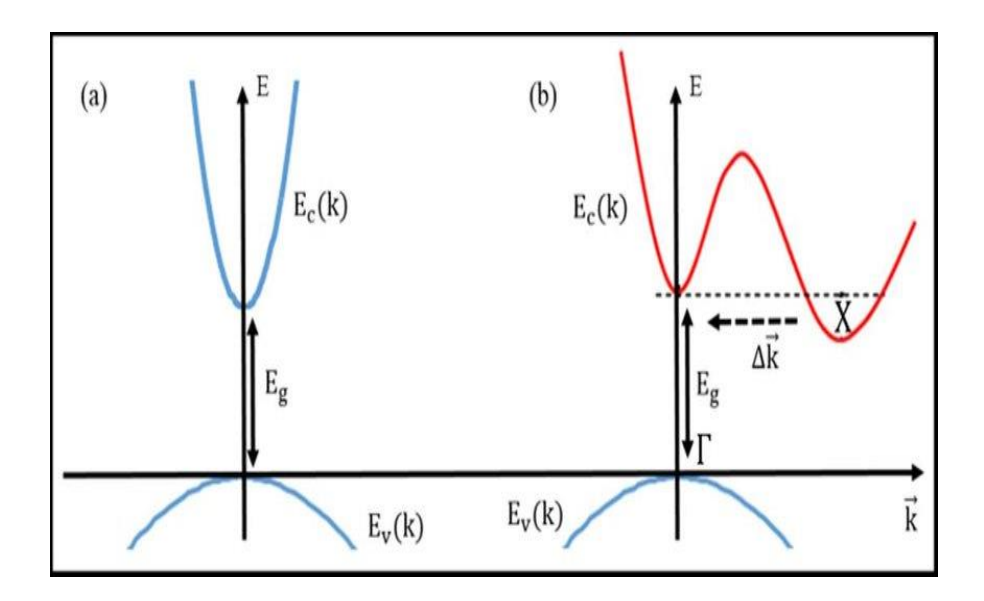


Figure II.33: Band structure of a semiconductor with (a) direct and (b) indirect gaps

♥ Estimation of the bandgap value (Eg)

The optical gap energy (Eg) is a crucial parameter for describing semiconductor materials. The following relationship establishes a correlation between this energy and the wavelength of the exciting light (λ ex) [39]:

$$\lambda_{ex}(nm) = \frac{1240}{Eg(eV)}$$
 Eq. II.18

There are two types of semiconductors:

- \checkmark Those with a low band gap (< 3 eV), which absorb in the visible range.
- \checkmark Those with a wide band gap (> 3 eV), which absorb in the ultraviolet [40].

The optical gap was calculated from Tauc's empirical relationship, given by the following equation:

$$(\alpha h \vartheta) = A (h \vartheta - E_g)$$
 Eq. II.19



Where:

n: An integer depending on the nature of the transition; for a direct gap, n= 1/2, while for an indirect gap n=2.

h: Represents Planck's constant.

ν: The frequency.

A: A constant linked to the properties of the material.

a: The absorption coefficient, determined by absorbance measurements according to the relationship [41].

$$\alpha = \frac{2.3026 A}{d}$$
 Eq. II.20

Where:

d: Thickness of the sample.

By extrapolating the curve to obtain a zero ordinate, i.e. when (αhv) ⁿ=0, we can deduce the experimental value of the optical gap Eg.



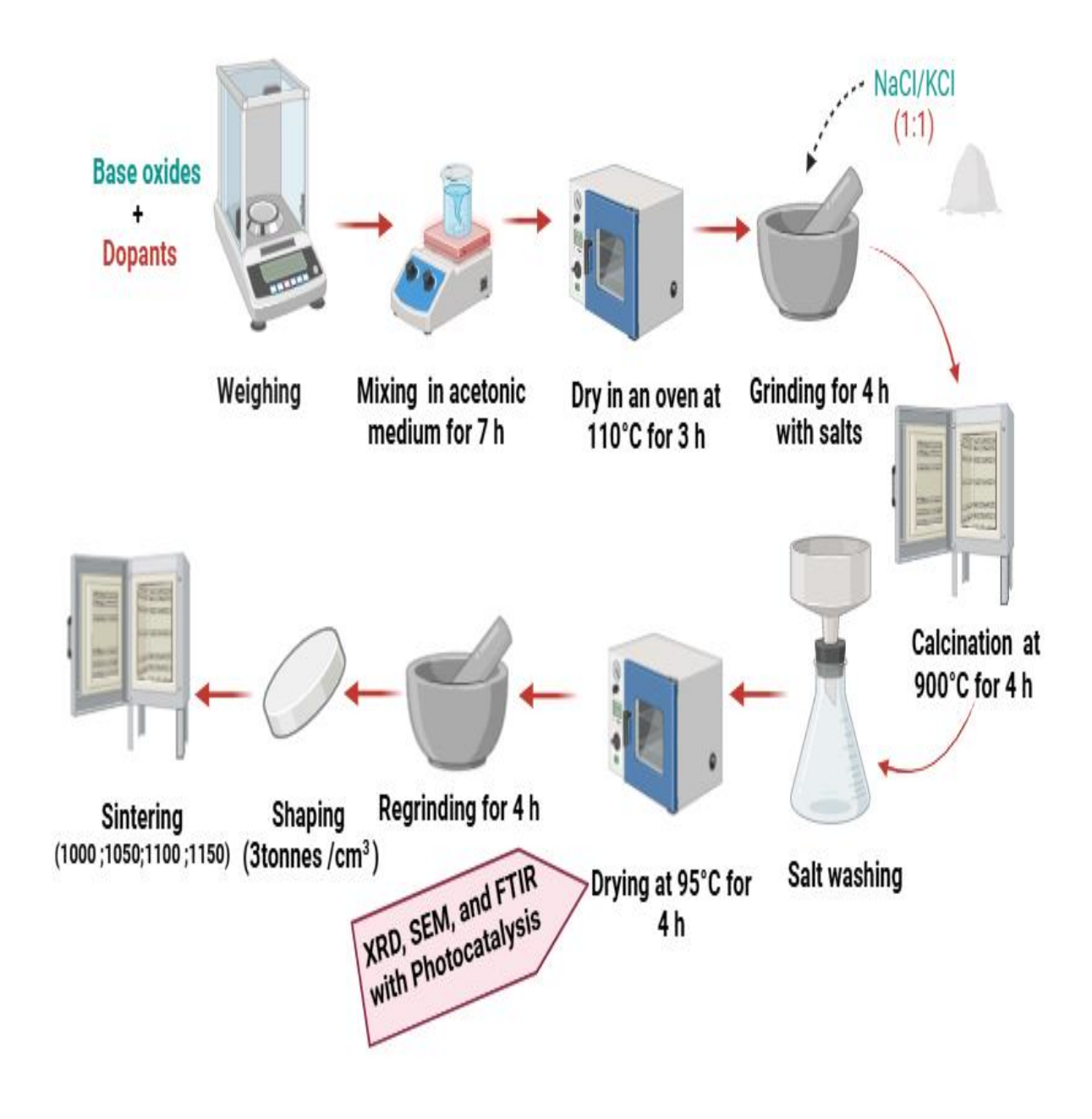


Figure II.34: The main steps of BNT ceramics synthesis by the molten salts method









- [1] **Boehm.** E et al. Oxygen diffusion and transport properties in non-stoichiometric $Ln_{2-x}NiO_{4+\delta}$ oxides. *Journal of Solid-State Ionics*, 176(37-38), 2717-2725. (2005).
- [2] Million. C. Contributions à l'étude de procèdes de réalisation de structures métal/PZT/métal sur silicium pour microsystèmes piézoélectriques, thèse de doctorat ,univ Institut National des Sciences Appliquées Lyon -France. (2003).
- [3] Aydi. A. Elaboration et caractérisations diélectriques de céramiques ferroélectriques et/ou relaxeur de formule MSnO₃-NaNbO₃ (M= Ba, Ca), thèse de doctorat, univ de Limoges-France. (2005).
- [4] Haeni. J. H et al. Epitaxial growth of the first five members of the Srn Ruddlesden-Popper homologous series. *NANOENGINEERING OF RUDDLESDEN-POPPER PHASES USING MOLECULAR BEAM EPITAXY*, 116. (2002).
- [5] **Zuniga.** J. P et al. Molten-salt synthesis of complex metal oxide nanoparticles. *Journal of visualized experiments: JoVE*, (140), 58482. (2018).
- [6] Liu.J. R et al. Large-scale production of strontium ferrite by molten-salt-assisted coprecipitation. *Journal of Powder Technology*, 262, 142-149. (2014).
- [7] Yuanbing. M. Large-scale synthesis of single-crystalline perovskite nanostructures. *Journal of American Chemical Society*.125(51),15718-15719. (2003).
- [8] Chang. Y et al. Molten salt synthesis of morphology controlled α-alumina platelets. *Journal of Ceramics International*, 43(15), 12684-12688. (2017).
- [9] Gilbert. M. R. Molten salt synthesis of titanate pyrochlore waste-forms. *Journal of Ceramics International*, 42(4), 5263-5270. (2016).
- [10] Mao. Y. Environmentally friendly methodologies for nanostructure synthesis. Journal of Small, 3(7), 1122-1139. (2007).



- [11] Kimura. T. Molten salt synthesis of ceramic powders. Advances in ceramics-synthesis and characterization, processing and specific applications, 75-100. (2011).
- [12] Angenault. J. Symétrie [et] structure : cristallochimie du solide : cours & exercices corrigés : premiers et deuxièmes cycles universitaires. Vuibert. (2001).
- [13] Michel.C. R et al. Novel CO2 and CO gas sensor based on nanostructured Sm2O3 hollow microspheres. *Journal of Sensors and Actuators B: Chemical*, 202, 1220-1228. (2014).
- [14] Jaffe. H et al. Piezoelectric ceramics. Journal of the American Ceramic Society, 41(11), 494–498. (1958).
- [15] Meklid. A. Elaboration, caractérisation et étude des propriétés diélectriques et électromécaniques d'un nouveau matériau de céramique de type Zirconate-Titanate de plomb (PZT), thèse de doctorat, univ Mohamed Khider-Biskra- Algérie. (2018).
- [16] Kahoul. F. Elaboration et caractérisation de céramiques PZT dopé et détermination de la frontière morpho tropique (FMP), thèse de doctorat, univ Mohamed Khider Biskra- Algérie. (2013).
- [17] Menasra. H. Influence de la température de frittage sur les propriétés structurales, diélectriques et piézoélectriques dans le système ternaire : Pb_{0.95}(La_{1-z}, Bi_z)_{0.05}[(Zr_{0.6}, Ti_{0.4})_{0.95}(Mn_{1/3}, Sb_{2/3})_{0.05}] O₃, thèse de doctorat, univ Mohamed Khider-Biskra-Algérie. (2015).
- [18] Bounab. K. Elaboration, caractérisation et étude des propriétés diélectriques d'une solution solide de type PZT, thèse de doctorat, univ Mohamed Khider-Biskra-Algérie. (2015).
- [19] Zachariasz. R et al. Influence of the Technology Conditions on the Mechanical and Dielectric Properties of the PZT-base Piezoceramic Transducers. *Journal of Solid-State Phenomena*, 89, 303-308. (2003).
- [20] Hachemi. F.A. Effect of doping and sintering temperature on the structural properties of a dielectric ceramic, mémoire de master, univ Mohamed Khider Biskra- Algérie. (2024).



- [21] Benabdallah. F. Evolution des propriétés diélectriques, ferroélectriques et électromécaniques dans le système pseudo-binaire (1-x) BaTi_{0.8}Zr_{0.2}O_{3-x}Ba_{0.7} Ca_{0.3} TiO₃ / Corrélations structures et propriétés, thèse de doctorat, Univ Bordeaux 1-France. (2013).
- [22] Boutarfaia. A. Investigations of co-existence region in lead zirconate-titanate solid solutions: X-ray diffraction studies. *Journal of Ceramics International*, 26(6), 583-587. (2000).
- [23] Nacera. Z. Étude de système quaternaire xPbZrO₃-yPbTiO₃-zPb (Mg_{1/3}, Nb_{2/3})_{1/2}O₃-zPb (Ni_{1/3}, Sb_{2/3})_{1/2}O₃ près de la frontière morpho tropique de phase (FPM), thèse de doctorat, univ Mohamed Khider-Biskra- Algérie. (2018).
- [24] Last. J. T. Infrared-absorption studies on barium titanate and related materials.

 Journal of Physical Review, 105(6), 1740. (1957).
- [25] Goetz. V. et al. Génie des réactions photo catalytiques pour la dépollution de l'eau par voie solaire, Rapport scientifique, Laboratoire Procédés Matériaux et Energie Solaire, PROMES CNRS Perpignan-France. (2006).
- [26] Mecheddou. CH, BARR. K. Valorisation des carapaces des crevettes dans la dépollution des eaux : Extraction du chitosane et optimisation des procédés, mémoire de master, univ Akli Mohand Oulhadj BOUIRA- Algérie. (2018).
- [27] Ohtani. B. Photocatalysis by inorganic solid materials: Revisiting its definition, concepts, and experimental procedures. In *Advances in inorganic chemistry* (Vol. 63, pp. 395-430). Academic Press. (2011).
- [28] Lettmann. C et al. Visible light photodegradation of 4-chlorophenol with a coke-containing titanium dioxide photocatalyst. *Journal of Applied Catalysis B: Environmental*, 32(4), 215-227. (2001).
- [29] Ganguly. P et al. Recent advances in photocatalytic detoxification of water. In S. Sharma & R. Sanghi (Eds.), *Nanoscale materials in water purification* (pp. 653–688). (2019).
- [30] Braslavsky. S. E et al. Glossary of terms used in photocatalysis and radiation catalysis (IUPAC Recommendations 2011). *Journal of Pure and Applied Chemistry*, 83(4), 931-1014. (2011).



- [31] Ameta. S. C, Ameta. R. (Eds.). Advanced oxidation processes for wastewater treatment: emerging green chemical technology. Academic press. (2018).
- [32] Vargas-Solano. S. V et al. Heavy metals in the volcanic and peri-urban terrain watershed of the River Yautepec, Mexico. *Journal of Environmental monitoring and assessment*, 191, 1-15. (2019).
- [33] **BENBRIKA. Ch.** Synthèse et caractérisation de l'hétérojonction [BIT dopé/ BFT] et son effet sur les propriétés photo catalytiques, thèse de doctorat, univ Mohamed Khider-Biskra- Algérie. (2024).
- [34] Hashimoto. K et al. TiO₂ photocatalysis: a historical overview and future prospects. *Japanese journal of applied physics*, 44(12R), 8269. (2005).
- [35] Li. Y et al. Photocatalytic reduction of CO₂ with H₂O on mesoporous silica supported Cu/TiO₂ catalysts. *Journal of Applied Catalysis B: Environmental*, 100(1-2), 386-392. (2010).
- [36] Herrmann. J. M. Bases de la photocatalyse hétérogène. L'Actualité Chimique, (397–398), 78. (2015).
- [37] AZAIZIA. B. L'huile essentielle de la plante médicinale Lythrum Salicaria, mémoire de master, univ8 Mai 1945 -Guelma-Algérie. (2021).
- [38] Achour. A. Élaboration et étude des propriétés structurales et photo catalytiques d'oxydes mixtes dérivés de pérovskites d'ortho ferrite de Lanthane (LFO) : La_{1-x}A_xFe_{1-y}B_yO₃, thèse de doctorat, univ Mohamed Khider-Biskra- Algérie. (2018).
- [39] Zhang. S et al. Atomically thin arsenene and antimonene: semimetal—semiconductor and indirect—direct band-gap transitions. *Journal of Angewandte Chemie International Edition*, 54(10), 3112-3115. (2015).
- [40] Levanyuk. A. P, Osipov. V. V. E. Edge luminescence of direct-gap semiconductors. Journal of *Soviet Physics Uspekhi*, 24(3), 187. (1981).
- [41] Pathan. H. M et al. Modified chemical deposition and physico-chemical properties of copper sulphide (Cu2S) thin films. *Journal of Applied Surface Science*, 202(1-2), 47-56. (2002).

Chapiter III: Experimental Results and Interpretation



III.1. Introduction

In this chapter, we carry out an in-depth analysis of the structural and morphological characteristics of a new ceramic matrix composed of BNT doped with different quantities of Sm₂O₃ ions at the A sites. These ceramics were developed using the molten salt method. We will analyze the characterization techniques employed in this study and discuss the obtained results. The aim of this approach is to understand how the doping process influences the structural and morphological properties of the ceramics [1].

III.2. Synthesis and production of ceramics

The chemical formula of our samples chosen for this study is: $(Na_{0.5} Bi_{0.5})_{1-x} Sm_x (Ti_{0.8} Zr_{0.2})_{0.9} (Fe_{1/5}Zn_{1/5} In_{3/5})_{0.1}$. Where x takes the values 0.00, 0.02, 0.04 and 0.06 successively.

Were manufactured using the molten salts method from a stoichiometric mixture of oxides and carbonate, as detailed and explained in Chapter II. The characteristics of the starting materials are shown in the table below:

Table III.1: Characteristics of the starting products.

Starting products	Degree of purity	Molar mass (g/mol)	The ions
	(%)		
Bi ₂ O ₃	99.6	465.96	Bi ³⁺
Na ₂ CO ₃	99.8	105.98	Na ⁺
T iO ₂	99.6	079.87	Ti ⁴⁺
Sm_2O_3	99.6	348.72	Sm ³⁺
ZrO ₂	99.6	123.22	Zr ⁴⁺
ZnO	99.6	081.37	Zn ²⁺
Fe ₂ O ₃	99.6	159.69	Fe ³⁺
In ₂ O ₃	99.6	309.63	In ³⁺

The table below summarises the different compositions that we are going to synthesise.

Table III.2: Different ceramic compositions prepared.

Composition	Samples	Matrix
	X	$(Na_{0.5}Bi_{0.5})_{1\text{-x}}Sm_x(Ti_{0.8}Zr_{0.2})_{0.9}(Fe_{1/5}Zn_{1/5}In_{3/5})_{0.1}$
Composition N°1	0.00	$(Na_{0.5}Bi_{0.5})(Ti_{0.8}Zr_{0.2})_{0.9}(Fe_{1/5}Zn_{1/5}In_{3/5})_{0.1}$
Composition N°2	0.02	$(Na_{0.5}Bi_{0.5})_{0.98}Sm_{0.02}(Ti_{0.8}Zr_{0.2})_{0.9}(Fe_{1/5}Zn_{1/5}In_{3/5})_{0.1}$
Composition N°3	0.04	$(Na_{0.5}Bi_{0.5})_{0.96}Sm_{0.04}(Ti_{0.8}Zr_{0.2})_{0.9}(Fe_{1/5}Zn_{1/5}In_{3/5})_{0.1}$
Composition N°4	0.06	$(Na_{0.5}Bi_{0.5})_{0.94}Sm_{0.06}(Ti_{0.8}Zr_{0.2})_{0.9}(Fe_{1/5}Zn_{1/5}In_{3/5})_{0.1}$

III.3. Stability conditions of the perovskite structure

The calculation of tolerance factors for BNT is related to knowing the atomic radii of the elements forming the prepared matrices. The table below presents the values of these radii.

Table III.3: Ionic radii and Valance number of elements in prepared matrices.

The ions	Ionic radii (Å)	Valance number
Bi ³⁺	1.03	3
Na ⁺	1.02	1
Ti ⁴⁺	0.74	4
Sm ³⁺	0.96	3
$ m Zr^{4+}$	0,72	4
Zn ²⁺	0.60	2
Fe ³⁺	0.65	3
In ³⁺	0.80	3



III.3.1. Electroneutrality condition

Table III.4 shows the results of the electroneutrality condition for each sample studied.

Table III.4: Results of the electroneutrality condition for the synthesized ceramic compositions.

Composition	X	k	k	k k
		$\sum X_{A_i} n_{A_i}$	$\sum X_{B_i} n_{B_i}$	$\sum X_{A_i} n_{A_i} + \sum X_{B_i} n_{B_i}$
		t=l	i=l	i=l i=l
Composition N°1	0.00	2.00	3.88	5.88
Composition N°2	0.02	2.02	3.88	5.90
Composition N°3	0.04	2.04	3.88	5.92
Composition N°4	0.06	2.06	3.88	5.94

It can be seen that the sum of the valence numbers for the AB part of the perovskite structure is close to six for all the compositions, so the stability of the perovskite structure is confirmed for all the samples.

The values in this table clearly confirm the stability of the criterion of the electroneutrality condition of the perovskite structure of the compositions studied [2].

III.3.2. Stoichiometric condition

Table III.5 shows the results of the stoichiometric condition for each composition studied.

Table III.5: Stoichiometric condition of the studied compositions.

Composition	X	k	k
		$\sum_{i=l} X_{A_i}$	$\sum_{i=l} X_{B_i}$
Composition N°1	0.00	1.00	1.00
Composition N°2	0.02	1.00	1.00
Composition N°3	0.04	1.00	1.00
Composition N°4	0.06	1.00	1.00

The sum of the fractions $\sum_{i=l}^{k} XAi$ and $\sum_{i=l}^{k} XBi$ is equal to 1 for all the compositions, so we say that the stoichiometric condition is verified [2].



III.3.3. Geometric condition

Table III.6 shows the results for the geometric condition of each composition studied.

Table III.6: Geometric tolerance factor(t) for the studied compositions.

Composition	X	t
Composition N°1	0.00	0,9845
Composition N°2	0.02	0,9831
Composition N°3	0.04	0,9823
Composition N°4	0.06	0.9815

According to Goldschmidt, the perovskite structure is stable if: 0.8 < t < 1.09 and this is verified for all the samples. We can therefore synthesise these compositions because all the compositions obey the stability conditions of a perovskite [3].

The 15g samples were prepared from the mixture of starting oxides according to the stoichiometry of the compositions.

Table III.7: The required masses of oxides for the different compositions.

Starting oxides	Masse (g)			
b	N° 1	N° 2	N° 3	N° 4
Bi ₂ O ₃	7.4313	7.2801	7.1125	6.9458
Na ₂ CO ₃	1.6868	1.6525	1.6144	1.5766
TiO_2	3.6685	3.6672	3.6574	3.6477
Sm ₂ O ₃	0.0000	0.2222	0.4435	0.6636
ZrO ₂	1.4149	1.4144	1.4106	1.4069
Fe ₂ O ₃	0.1018	0.1018	0.1015	0.1012
ZnO	0.1038	0.1037	0.1035	0.1032
In ₂ O ₃	0.5925	0.5923	0.5907	0.5892



III.4. Powder characterisation

As a preliminary step, we characterised our samples using infrared (IR) spectroscopy before and after calcination. Subsequently, X-ray diffraction (XRD) and scanning electron microscopy (SEM) analyses were performed on the calcined samples to confirm the formation of the perovskite phase of BNT.

III.4.1. Structural characterisation

III.4.1.1. X-ray diffraction analysis

a) Crystallographic study of BNT

In order to determine the phase transition line of a new bismuth-sodium titanate (BNT) ceramic material containing dopants such as Sm₂O₃, ZnO, and Fe₂O₃, we performed a study using the geometric addition method.

Below the Curie temperature, BNT exhibits crystalline behaviour similar to that observed in PZT, where it exists in the form of two main phases: The tetragonal (T) phase, which is typically observed in titanium-rich compositions, and the rhombohedral (R) phase, which is seen in bismuth or sodium-rich compositions. This behaviour is reflected in the X-ray diffraction results, as the crystal peak (200) in the tetragonal structure splits into two peaks (200) and (002), while the peak (200) remains unbroken in the Rhombohedral phase.

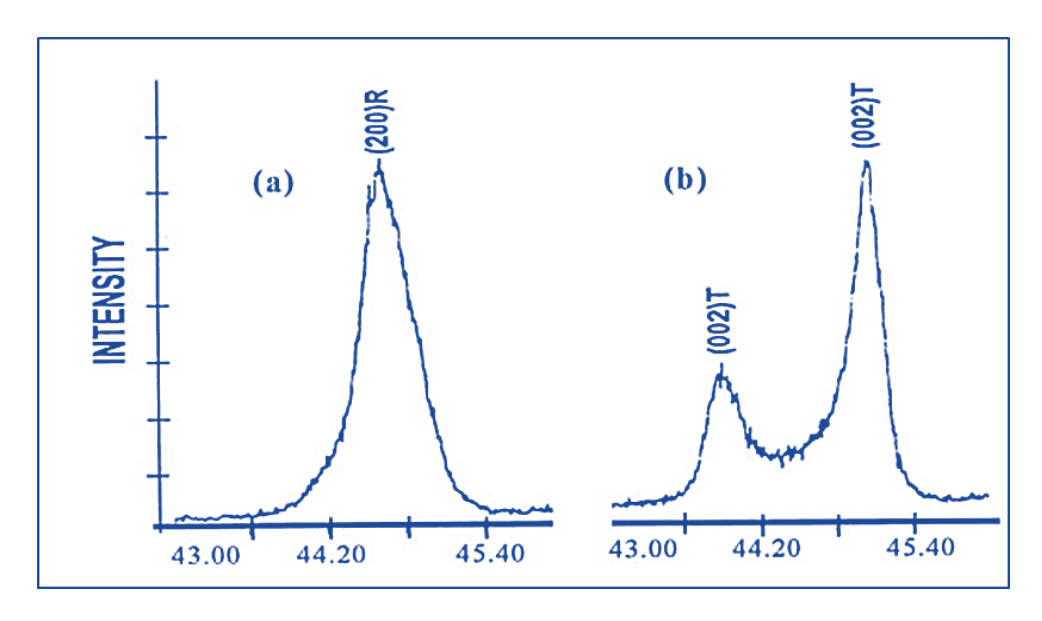


Figure III.1: Typical diffraction spectra of the Tetragonal (T) and Rhombohedral (R) phases



The morpho-tropic phase boundary (T+R) is determined by observing the shape of the diffracted lines. The appearance of the lines diffracted by samples where the two tetragonal and rhombohedral phases coexist (T+R) is represented by three types [4].

- ♣ A pattern with three maxima (fig. III.2. a).
- ♣ Alignment with two maxima (fig. III.2. b).
- ♣ A curve with a maximum accompanied by an inflection point (fig. III.2.c).

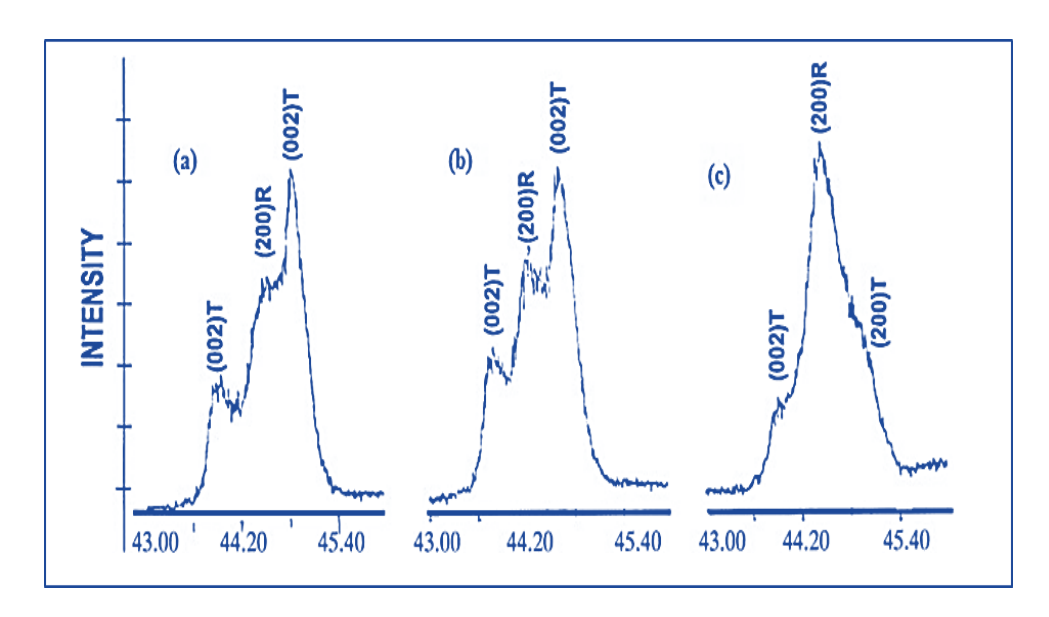


Figure III.2: The different shapes of the peaks characteristic of the coexistence of the (T+R) phase

It should be noted that many researchers have reported that the coexistence of Tetragonal (T) and Rhombohedral (R) phases can be detected in several regions of the diffractogram spectrum. Table III.8 below summarises the most important regions in 2θ where the R and T phases coexist.



Table III.8: Region of coexistence of the Tetragonal-Rhombohedral phases and indexing of the corresponding planes.

2θ	(hkl) _T	(hkl) _R
21-23	(001) and (100)	(100)
30-33	(101) and (110)	(110) and (101)
37-40	(111)	(111) and (111)
43-47	(002) and (200)	(200)
53-56	(112) and (211)	(211), (211) and (211)

b) Calcined BNT powders

According to the literature, the calcination temperature of doped BNT ceramics varies according to the dopants, generally between 750°C and 900°C. X-ray diffraction results for two compositions calcined at 900°C are shown in fig.III.5.

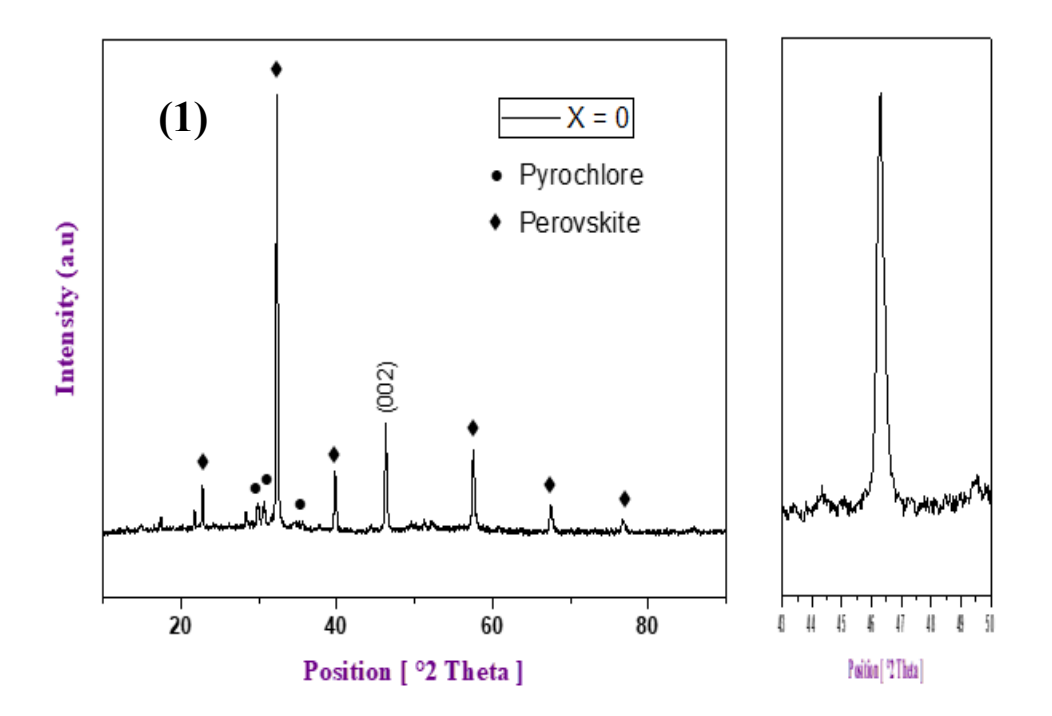


Figure III.3: Diffractogram for composition N°1 with X =0% calcined at 900°C



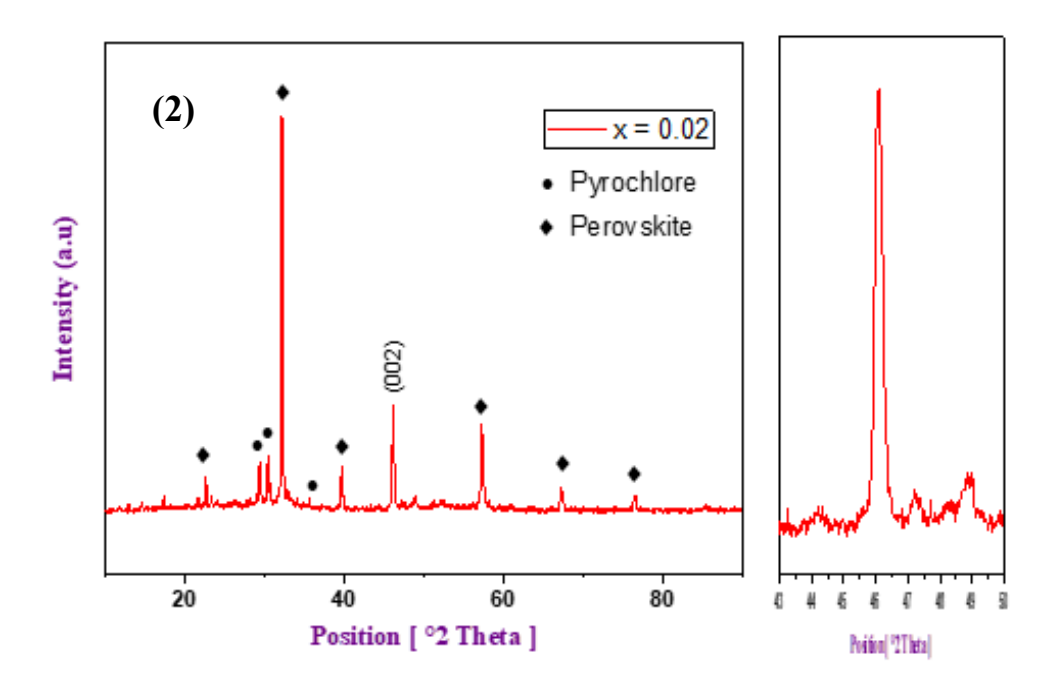


Figure III.4: Diffractogram for composition N° 2 with X =0.02% calcined at 900°C

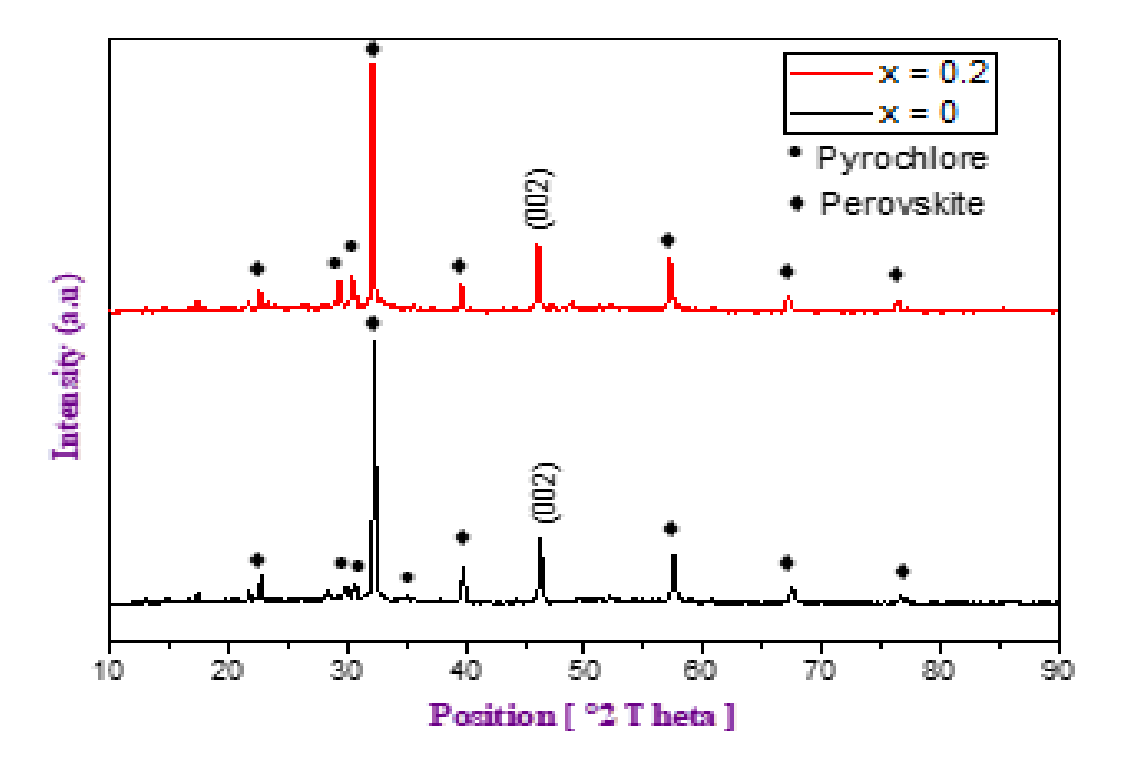


Figure III.5: Diffractogram for two compositions N°1 and N° 2 calcined at 900 °C.

1)
$$x = 0\%$$
, 2) $x = 2\%$



According to the results It can be seen that there is no great difference between the two diffractogram and that the main phase present in both compositions is the perovskite phase, accompanied by several secondary peaks corresponding to the pyrochlore phase $Bi_2Ti_2O_7$ [5]. A well-defined peak corresponding to the (002) (tetragonal phase) plane around 2θ =46° was noted in both compositions

The intensity of the pyrochlore phase in composition 2 is higher than in composition 1 and this is due to the presence of the samarium element in the ceramic structure of the sample.

The obtained result signifies the presence of tetragonal (P_{4bm}) symmetry according to ASTM data sheet 01-070-4760.

Table III.9: Crystallographic phases identified after calcination at 900 °C.

Sm concentration (%)	Nature of phases
0	T
2	Т

During calcination at 900°C, we noticed that the synthesized compositions were a mixture of the two perovskite and pyrochlore phases detected for all samples, the peaks of this phase (pyrochlore) detected at 2θ (°) = 31.65, 35.40. The relative proportion of the pyrochlore phase is evaluated based on the specified peak intensity [6]:

pyrochlore (%) =
$$\frac{Ipyro}{Ipyro + I(002)} \times 100$$
 Eq. III.1

I pyro: The intensity of the pyrochlore peak.

 $I_{(002)}$: The intensity of the (002) peak.



Table III.10: Estimation of the pyrochlore phase proportion based on the intensity of characteristic peaks.

Sm concentration (%)	pyrochlore (%)
0	08.48
2	13.87

Evolution of lattice parameters as a function of composition BNT

At a fixed temperature of 900 °C, we studied the evolution of the lattice parameters of the $(Na_{0.5} Bi_{0.5})_{1-x} Sm_x (Ti_{0.8} Zr_{0.2})_{0.9} (Fe_{1/5}Zn_{1/5} In_{3/5})_{0.1}$ solution as a function of Sm composition.

The lattice parameters are determined by the evolution of the position of the peak of the phase formed using High score Plus. (Tab.III.11) shows the crystalline parameters of our BNT samples after calcination at a temperature of 900 $^{\circ}$ C.

Table III.11: Calculated crystalline parameters of the prepared BNT sample.

Type of phase	Sm %	a=b (Å)	c (Å),	$\alpha = \beta = \gamma$ (°)	Volume
Tetragonal	0	5,5040	3,9067	90	118,1496
	2	5,5190	3,9080	90	118,8158

Figure III.6 shows the calculated crystal parameters of the two prepared samples as a function of samarium content, for all ceramic samples calcined at 900 °C. It is observed that these parameters are highly sensitive to changes in composition. The a_T, c_T parameters of the tetragonal phase (T) phase decrease with increasing Sm concentration.

In general, there is a slight difference between the a_T and c_T lattice parameter values for compositions N^o . 1 and N^o . 2. This slight difference confirms the stability of the perovskite structure.



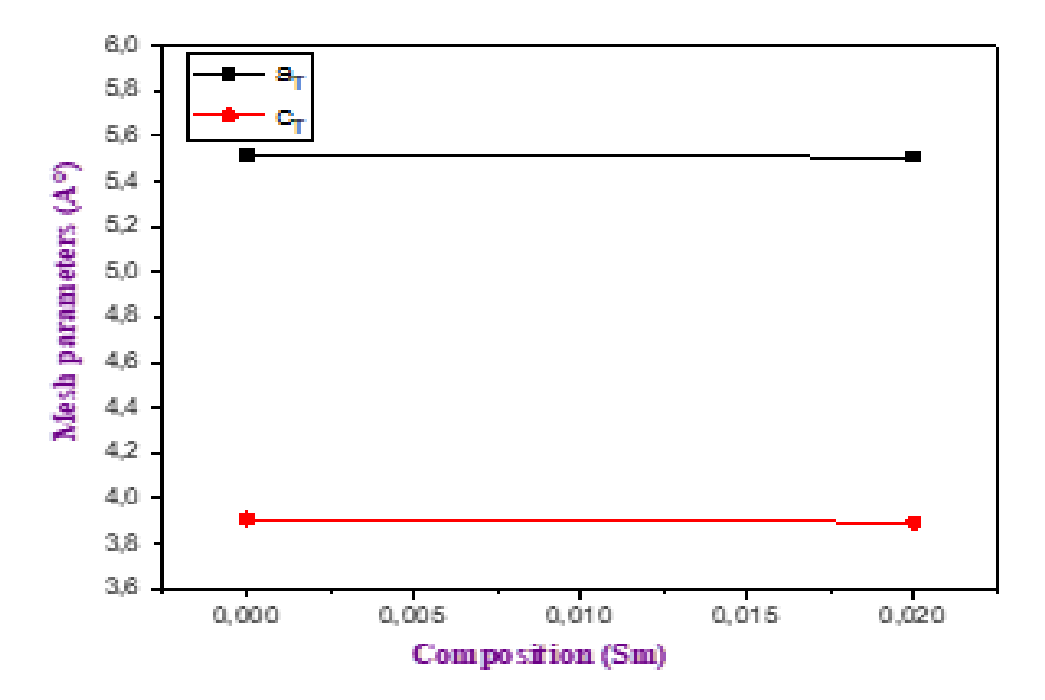


Figure III.6: Evolution of mesh parameters as a function of samarium rate for two samples calcined at 900 °C

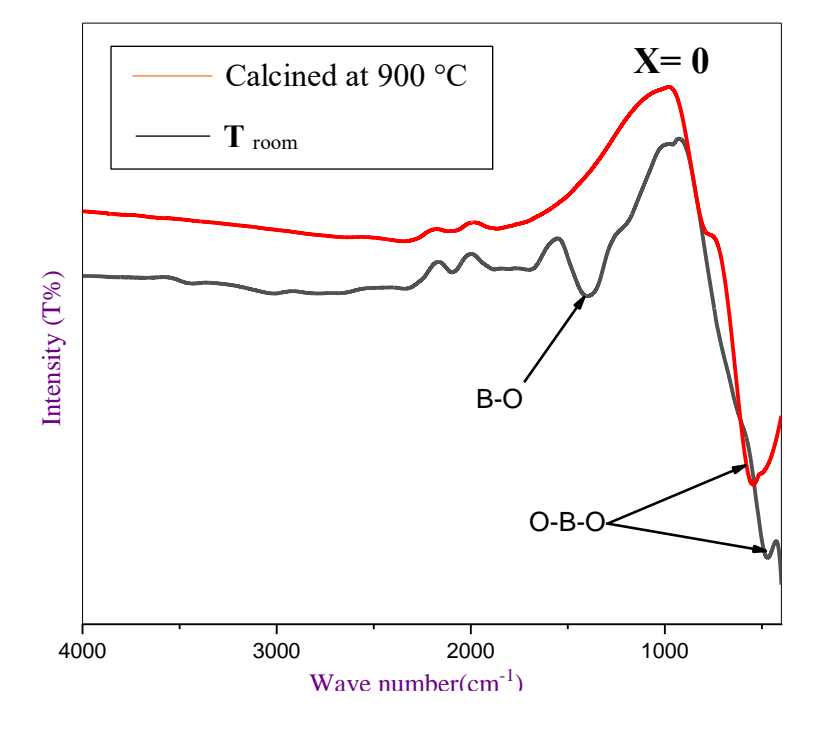
III.4.2. Characterisation of powders by infrared spectroscopy

The use of Fourier Transform Infrared (FTIR) spectroscopy is only a complementary step that provides further information on the formation temperature of the BNT solid solutions.

Transmission infrared spectra were obtained using an Agilent Cary 630 FTIR spectrometer. The wavelengths studied ranged from 4000 - 400 cm⁻¹ in the mid-infrared [1].

Figure III.7 shows the infrared (IR) spectra of the mixtures at room temperature, with IR spectra of the powders calcined at 900 °C, with different concentrations of Sm.





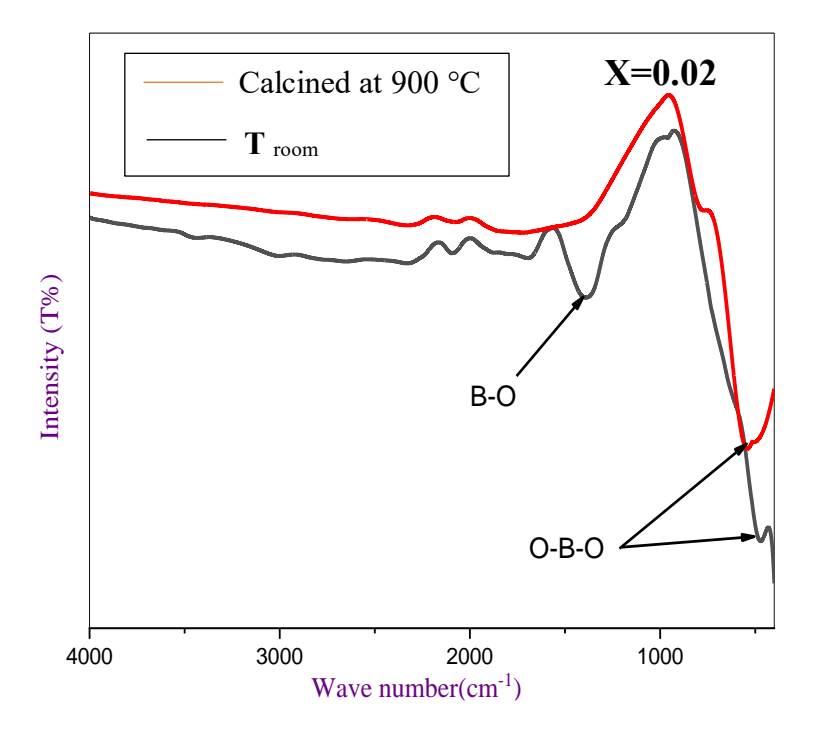
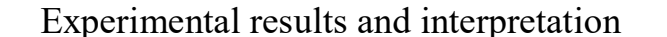


Figure III.7: The infrared (IR) spectra of the mixtures before calcination and after calcination at 900 $^{\circ}\mathrm{C}$





For the powders before calcinations, an intense band at around 1400 cm-¹ was observed, corresponding to the vibration of the B-O bond of the reactants

After calcination at 900 °C, the powders exhibit an intense band around 540 cm⁻¹, also attributed to the O–B–O bond vibration, which further confirms the formation of the perovskite (ABO₃) phase of BNT.

III.4.3. Morphological study of BNT ceramics

Chapitre III

In our work, the morphological study is carried out after calcinations (900 °C) and sintering at different temperatures (1000, 1050, 1100 and 1150 °C). These are density, porosity and microstructure.

III.4.3.1. Scanning electron microscopy (SEM) characterization

Scanning electron microscopy provides information on the shape and size of the grains. This technique makes it possible to estimate the particle size distribution, the average grain size after sintering and qualitatively evaluate the presence of porosity and secondary phases.

Figure.III.8, presents SEM micrographs for the composition N° 2 at the calcination temperature $T=900^{\circ}C$.



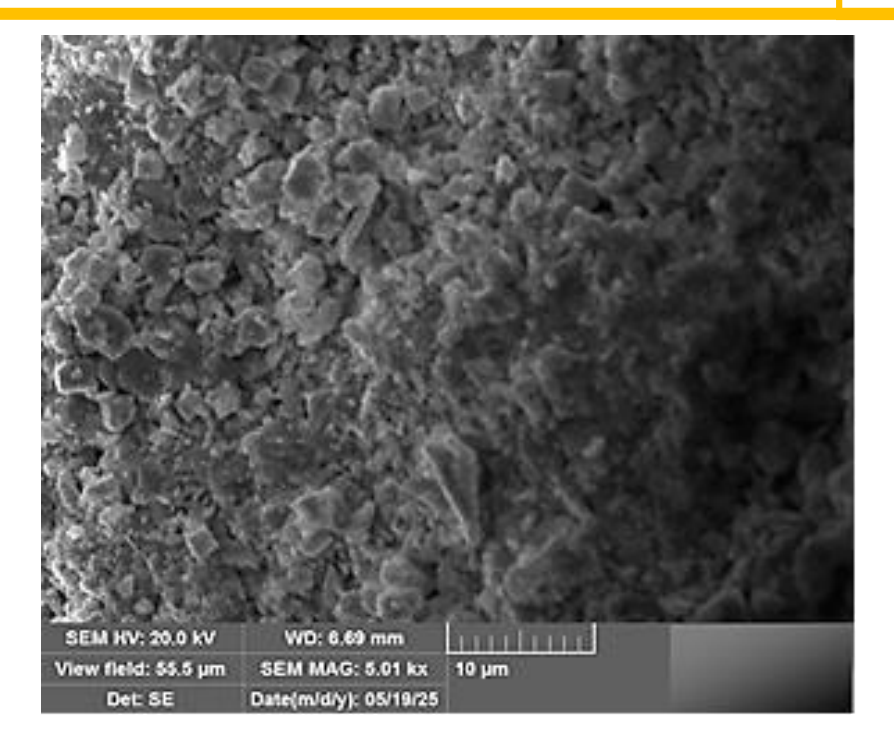


Figure III.8: SEM micrographs of the composition N° 2 calcined at 900°C

The micrograph of the ceramic show that the material is very dense (fig.III.8), confirming the densification of the materials due to the diffusion mechanisms of the material during calcinations.

It also shows remarkable intergranular porosity for this composition doped with 2% samarium, narrow grain distribution in the sample, as well as the appearance of unreacted starting materials, which could be due to insufficient calcinations temperature, etc.

It can be seen that the average grain size calculated by "visiomètre" software for the second (x=0.02) sample is 2.87 μ m, and the grain distribution is uniform throughout. It is clear that porosities are not eliminated during calcinations for the composition, which could influence the electrical and electromechanical properties of these perovskite materials, which are highly dependent on their microstructures.

Density and porosity measurements are performed on 1.1g pellet samples of sintered BNT powders.

The results of the theoretical density, experimental density, porosity, and densification rate of samples of the sintered BNT system at different temperatures are reported in (Tab. III.12).



Table III.12: Experimental and theoretical density, densification rate and porosity for all samples.

T (°C)	Composition	Molar mass (g/mol)	Exp. density (g/cm ³)	Densification rate	Porosity (P)
1000	X=0.00	236.0757	5.3360	66,7004	0,3329
	X=0.02	236.1607	5.0885	63,6066	0,3639
1050	X=0.00	236.0757	5.3550	66,9381	0,3306
	X=0.02	236.1607	5.9089	73,8612	0,2613
1100	X=0.00	236.0757	4.4149	55,1863	0,4481
	X=0.02	236.1607	4.0504	50,6300	0,4936
1150	X=0.00	236.0757	3.9921	49,9012	0,5009
	X=0.02	236.1607	3.8328	47,9101	0,5208

III.4.3.2. Density

The study of density is necessary in order to optimise the sintering temperature. Material quality increases with increasing density, and density increases with increasing sintering temperature [2].

Density measurements were carried out on pellet samples of diameter $D=13\,$ mm and thickness $e=1.1\,$ mm, and the density of BNT was studied as a function of sintering temperature and Sm ratio. This study is necessary in order to optimise the sintering temperature and find the densest composition at the optimum sintering temperature, and to see the effect of the doping rate on the density.



Use of the end of the

The optimum sintering temperature is determined from the curves of density versus sintering temperature d = f(T). The maximum density corresponds to the product with the best electrical quality. Figure III.9 shows the density curves for two BNT (X = 0 and 0.02) samples as a function of sintering temperature.

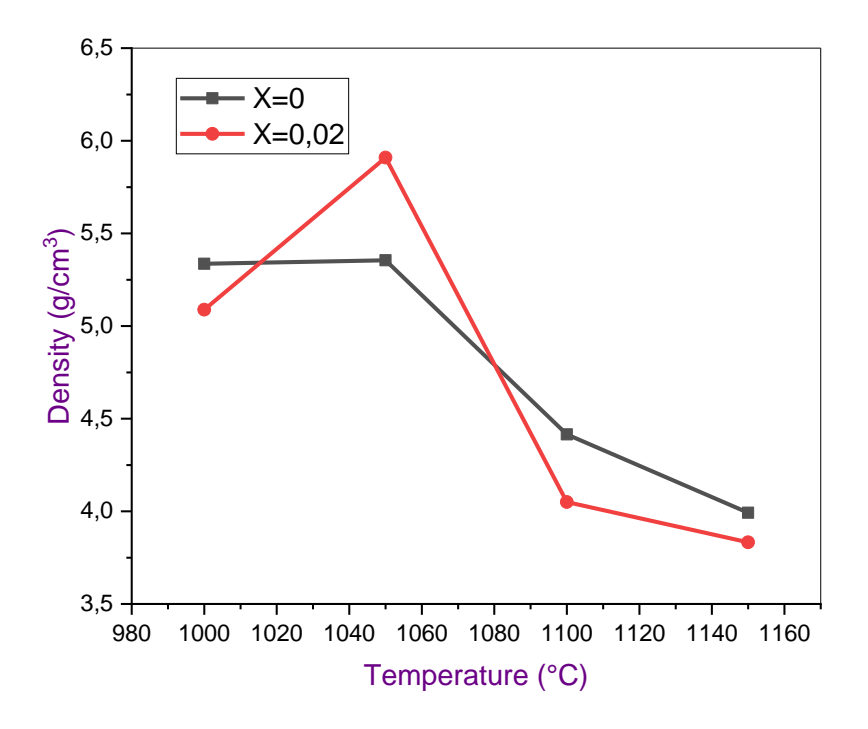


Figure III.9: Evolution of density as a function of sintering temperature

The same pattern can be observed for all the curves: the density is minimal for a sintering temperature T_S = 1000 °C, it starts to increase until it reaches a maximum value at a sintering temperature T_S = 1050 °C, above this temperature the density starts to decrease again for samples sintered at a temperature $T_S = 1100$ °C and 1150 °C. We can therefore say that the sintering temperature of 1050 °C is the optimum sintering temperature.

The increase in density implies a reduction in the number of pores, so the volume of the mesh decreases and, as a result, the structure becomes more compact.

The optimum sintering temperature depends on a number of factors, such as the addition of impurities, the sintering speed and the holding time.

Evolution de la densité en fonction de la composition

The evolution of the density of the different BNT samples sintered at 1000, 1050, 1100 and 1150 °C as a function of the Sm rate is illustrated in the fig.III.10.



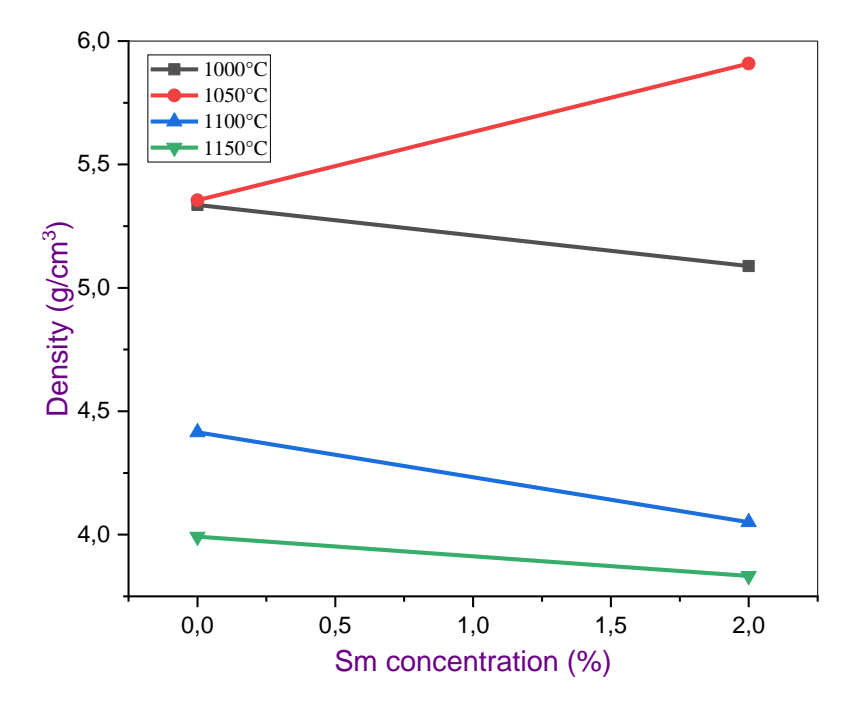


Figure III.10: Evolution of density as a function of Samarium content

Figure.III.10 shows that the density increases for all the samples sintered at 1050 °C with increasing Sm content, reaching a maximum value of 5.9089 (g/cm³) (73.86 % of the theoretical density) at Sm= 2% (sample N°.2).

III.4.3.3. Porosity

The variation in porosity as a function of sintering temperature for all the samples is plotted in fig.III.11.



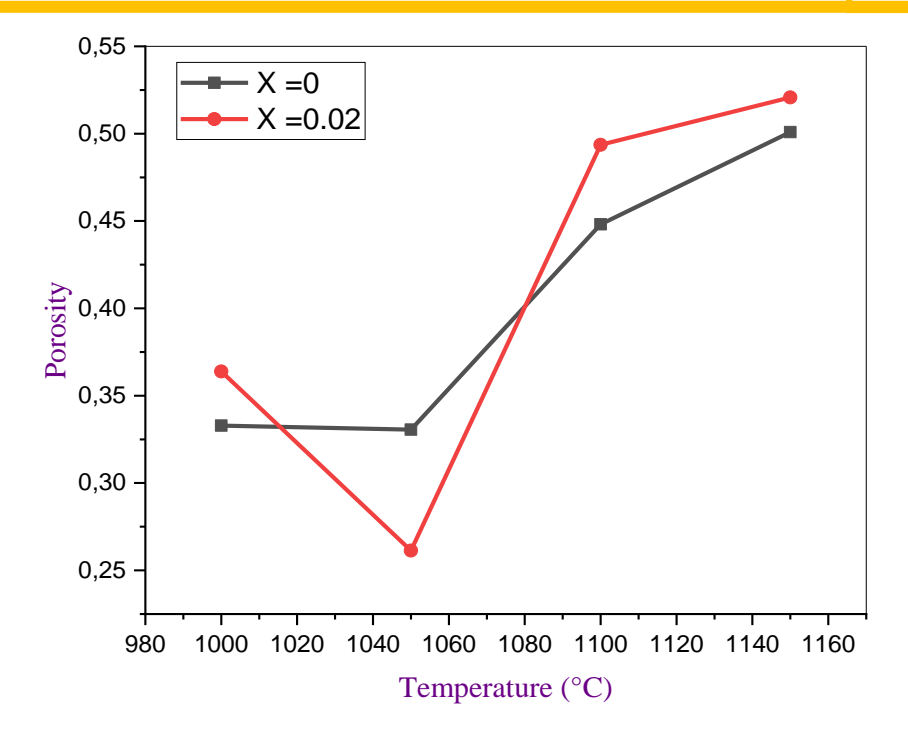


Figure III.11: Variation in porosity as a function of sintering temperature

The porosity curve is the inverse of the density curve. The same behaviour was observed for all the samples sintered at different sintering temperatures. Porosity decreases progressively as the sintering temperature rises, reaching a minimum value at 1050 °C, the temperature at which the maximum density is recorded; after this temperature, porosity increases again; this behaviour indicates that the optimum sintering temperature is 1050 °C.

The variation in porosity as a function of samarium content at the optimum sintering temperature of 1050 °C for all the samples is plotted in fig. III.12.

Figure III.13 shows porosity and density as a function of samarium content for all the ceramic samples sintered at $1050~^{\circ}$ C. We can see that the porosity curve is the inverse of the density curve, decreasing to a minimum for the sample with a doping rate of 2% (sample N° 2), which corresponds to the maximum density.



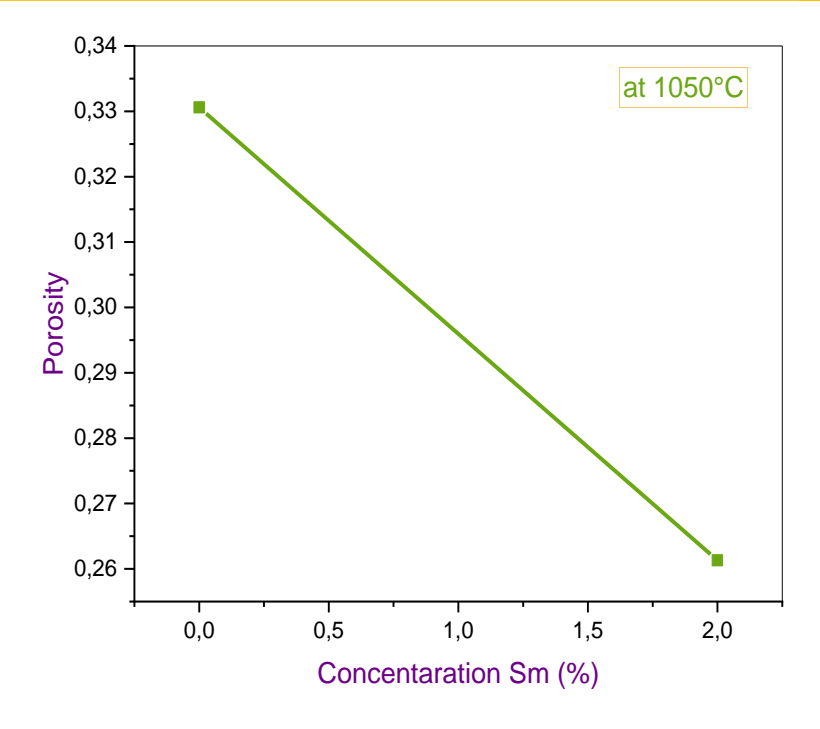


Figure III.12: Evolution of porosity as a function of samarium content for all samples sintered at 1050 °C

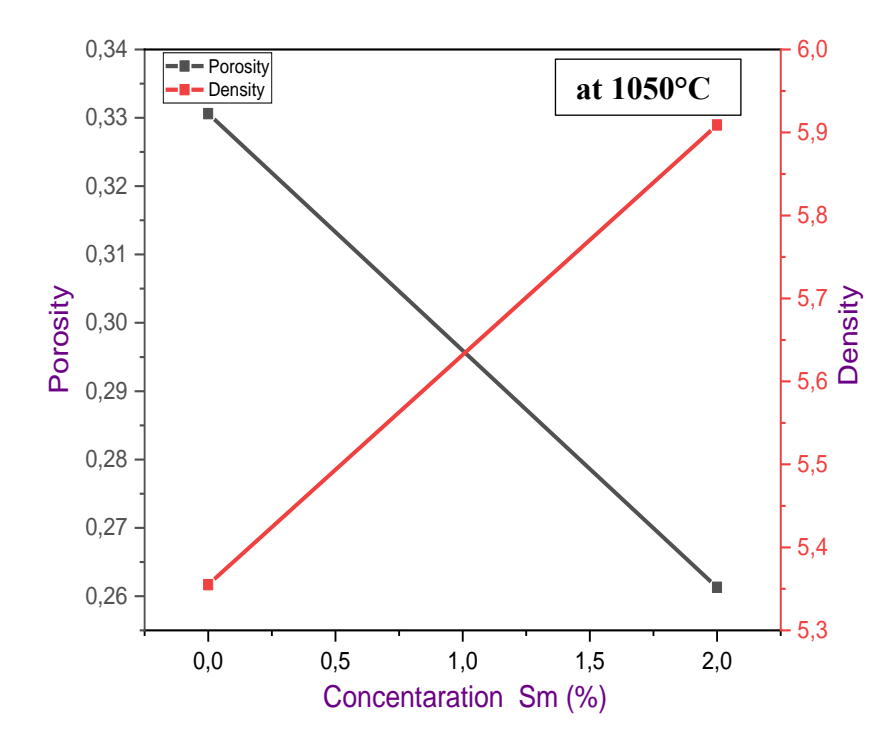


Figure III.13: Evolution of porosity and density as a function of samarium content for all samples sintered at 1050 $^{\circ}$ C



III.5. Optical characterisation by UV-Visible

The optical bandgap energy of perovskite materials is a crucial factor in assessing their photocatalytic activity [7, 8].

The optical gap (Eg) of the synthesised compounds, composition N°. 1 and N°. 2, was estimated by applying Tauc's relation: for a direct gap, described by the following equation:

$$(\alpha hv) = A (hv - E_a)^{1/2}$$
 Eq. III.2

Where:

hv: The photon energy (eV).

A: A constant.

α: The absorption coefficient.

Eg: The optical gap expressed in eV.

The optical gap (Eg) was evaluated by plotting $(\alpha h v)^{1/2}$ versus photon energy hv. The intersection of the linear part of this curve with the x-axis corresponds to the value of Eg, as shown in fig. III.14.

The optical gap values, determined from fig III.14, are as follows: 2.22 eV (composition N°. 1), 2.14 eV (composition N°. 2). It is notable that the bandgap value for composition N°. 2 is significantly lower than that for composition N°. 1, indicating a significant reduction due to the doping effect. Furthermore, sample N°. 2 has the lowest bandgap value, which can be attributed to its high specific surface area, suggesting its potential as a material for visible light photocatalytic applications.



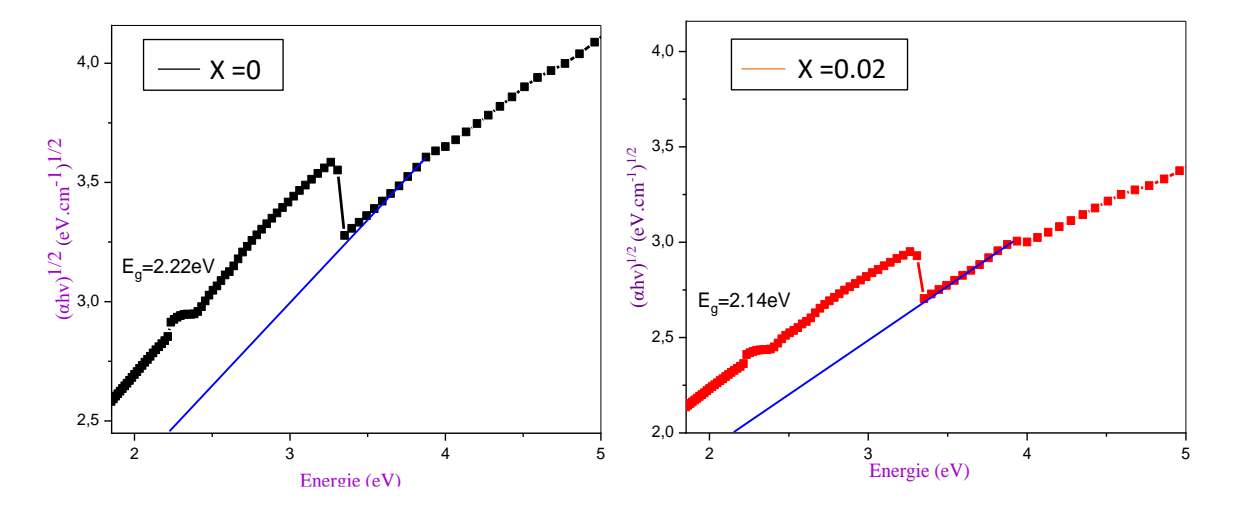


Figure III.14: Evaluations of $(\alpha h v)^{1/2}$ as a function of energy (hv) for the two compositions studied

III.5.1. Methylene blue (MB) self-degradation test

Before studying the photocatalytic activity of our catalysts, a preliminary test was carried out to assess the stability of the MB in the absence of any catalyst. The aim of this test was to check whether the MB could degrade spontaneously, without the intervention of a photo-induced process, and thus make it possible to clearly dissociate the effect of the catalyst itself. Two experimental conditions were considered:

- ♣ In total darkness: to observe any degradation linked solely to adsorption or physical phenomena.
- **Under solar irradiation**: to determine whether solar radiation alone is capable of inducing MB degradation, without a catalyst [8].

The tests were carried out over a period of 3 hours, with regular monitoring of the MB concentration in each condition. The results, presented in Tab. III.13, rule out any non-photo-induced contribution to dye degradation. In this way, the performance subsequently observed can be reliably attributed to the synthesised catalysts.



Table III.13: Evolution of the MB concentration (without catalyst) under different conditions for 3 hours

t= 0	$A_{\text{max}} = 0.9740$
t =3h without light	$A_{\text{max}} = 0.9591$
t=3h with light	$A_{\text{max}} = 0.8972$

The results in the table show that the MB undergoes virtually no degradation in the absence of a catalyst, either in the dark or under direct solar irradiation. This observation confirms that the degradation processes observed in subsequent experiments will be essentially due to the photocatalytic effect of the catalysts studied.

III.5.2. Study of the photodegradation of methylene blue

III.5.2.1. Experimental protocol

The photocatalytic activities of BNT with different Sm amounts were evaluated by degradation of Methylene blue (MB) in an aqueous solution ([MB]₀=5mg/l, catalyst m=100mg, pH (MB)=6) under sunlight irradiation (wavelength > 400 nm).

Methylene blue was selected as a model organic pollutant.

Before irradiation, the solutions were kept in the dark for 30 minutes to eliminate any interference from adsorption. A 4 mL sample was taken and analysed by UV-visible spectrophotometry. The suspension was then exposed to sunlight, with samples taken every 15 minutes for 3 hours. Each sample was filtered and analysed to measure the absorbance of the MB.

The degradation efficiency (DE) of the organic dye was calculated using the following equation [9]:

$$DE (\%) = \frac{Ci - Ct}{Ci} \times 100 \qquad Eq. III.3$$

Where:

DE: The degradation efficiency.

Ci: The initial concentration of the MB.

Ct: The concentration of the MB after a time t.



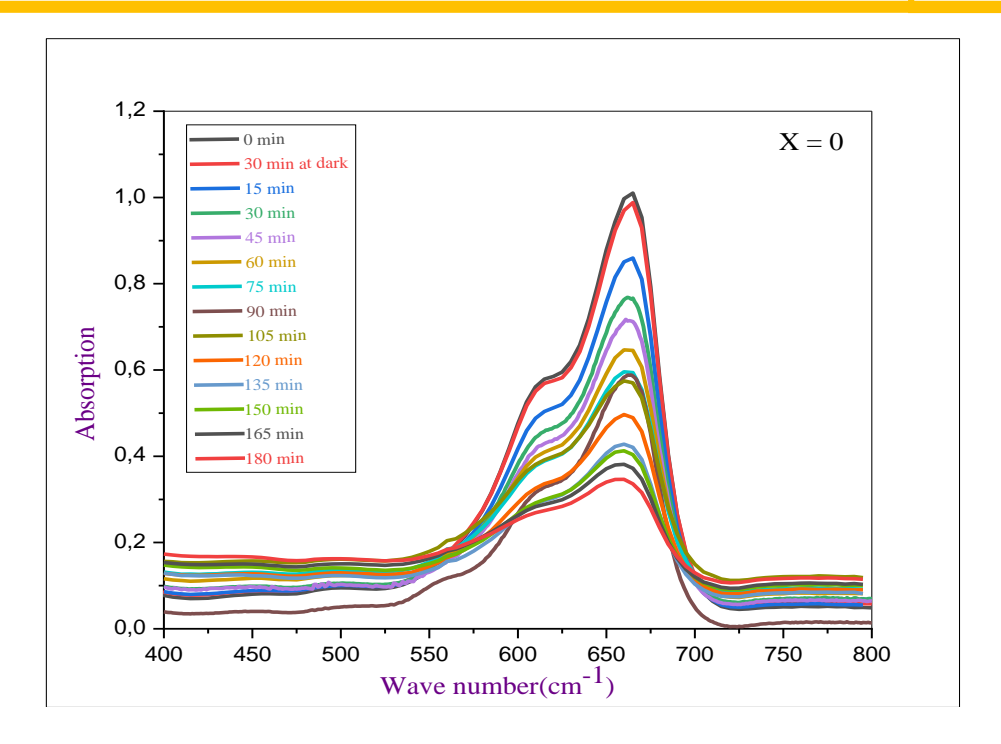


Figure III.15: photocatalysis of methylene blue under solar irradiation

III.5.2.2. Photocatalytic activity Sm doped and undoped BNT ceramics

In order to evaluate the impact of samarium (Sm³⁺) doping at site A on the photocatalytic activity of BNT for the degradation of methylene blue (MB) under natural sunlight, we monitored the temporal evolution of the UV-visible spectra of MB (fig. III.16), as well as the variation of the relative concentration C_t/C_0 as a function of irradiation time (fig. III.17). The results in terms of degradation efficiency are presented in (fig. III.18).





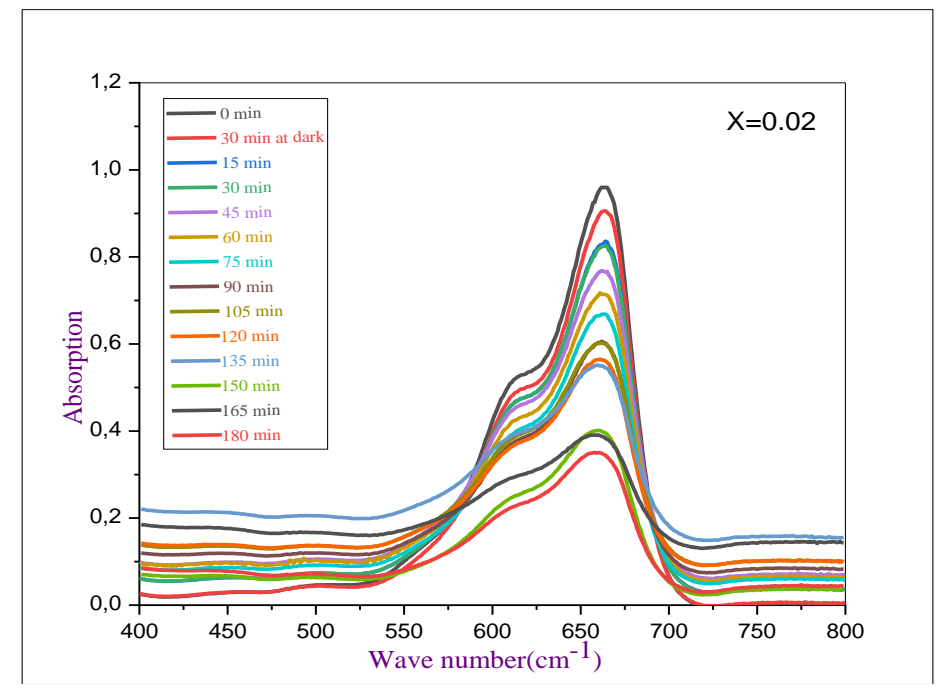


Figure III.16: Changes in the absorbance spectra of methylene blue under light irradiation in the presence of BNT-X=0 and BNT-X=0.02 photocatalysts

Figure III.16 shows that the characteristic MB absorption peak (664nm) decreases rapidly as a function of reaction time in the presence of the BNT-X=0.02 catalyst compared with the undoped compound BNT-X=0.02



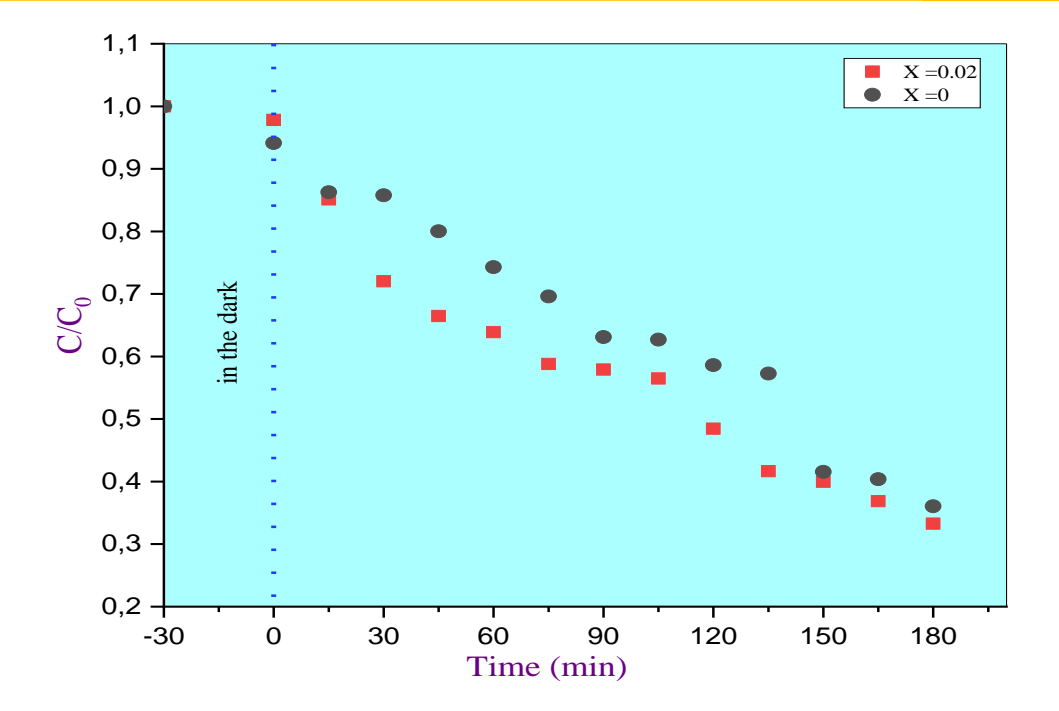


Figure III.17: Evolution of the relative concentration C_t/C_0 of MB as a function of irradiation time in the presence of BNT-X=0 and BNT-X=0.02

From Figure III.17, a faster decrease in the relative concentration of methylene blue (C_t/C_0) in the presence of the BNT-X=0.02 catalyst compared to BNT-X=0. This decrease results in a higher degradation rate for BNT-X=0.02 (63.44%) than for BNT-X=0 (58.25%), as confirmed by Figure III.18 and the data in Table III.14.

Although our results are interesting, it is important to note that a direct comparison with previous studies. is complex due to experimental differences. A more in-depth analysis would require the study of the degradation of the same dye under the same experimental conditions [8].



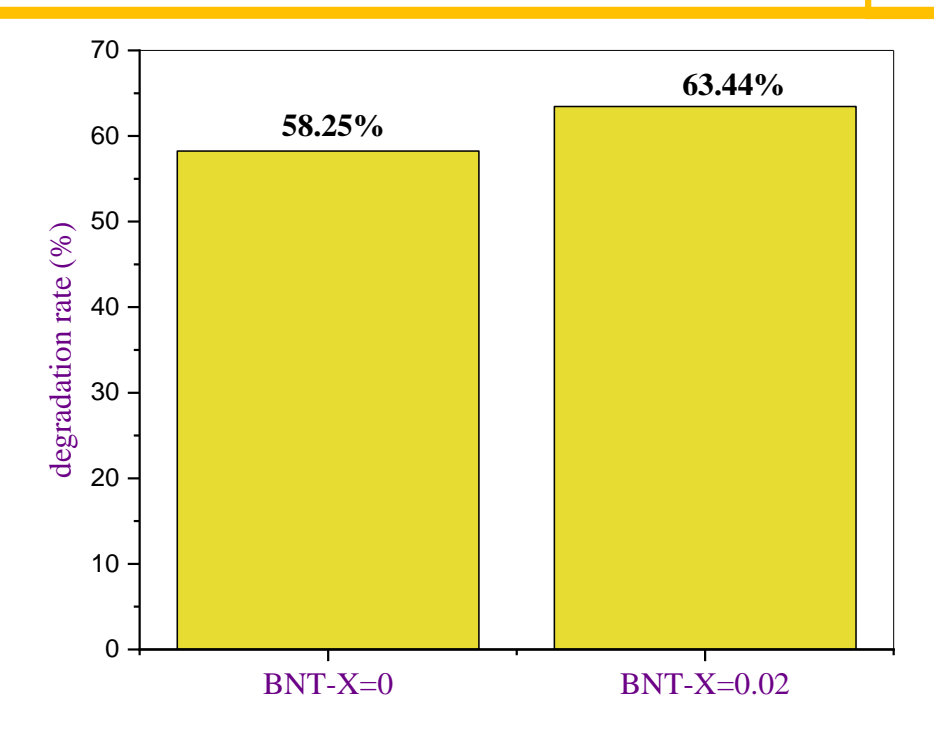


Figure III.18: Photocatalytic efficiency of MB degradation by BNT-X=0 and BNT-X=0.02 catalysts

Table III.14 shows the values of the gap energy (Eg) and the degradation rate (D %) of two compositions BNT-X=0 and BNT-X=0.02.

Table III.14: Eg values and degradation rate (D%) for BNT-X=0 and BNT-X=0.02.

Catalyst	D (%)	E _g (eV)
BNT-X=0	58.25	2.22
BNT-X=0.02	63.44	2.14

a key factor in photocatalytic activity is the optical gap energy (Eg), which is the energy differential between the valence and conduction bands. A lower Eg promotes the production of electron-hole pairs, which are in charge of the oxidation reactions that break down the pollutant, by enabling more effective absorption of visible light [8]. Samarium (Sm³+) doping of the BNT-X=0 compound resulted in a decrease in Eg from 2.22 eV to 2.14 eV for BNT-X=0.02, which accounts for the latter catalyst's higher methylene blue degradation efficiency.



III.5.2.3. Kinetic study of MB degradation by BNT pure and BNT doped

This section presents an in-depth kinetic analysis of the photocatalytic degradation of methylene blue (MB) in order to evaluate the performance of the synthesised catalysts. For this purpose, the Langmuir-Hinshelwood pseudo-first-order kinetic model was used, expressed by the following equation:

$$\operatorname{Ln}\left(\frac{C0}{Ct}\right) = K_{app} \cdot t \qquad Eq. III.4$$

Where:

C₀: Is the initial concentration of BM

C_t: Is the concentration at an instant (t)

 K_{app} : Is the apparent pseudo-first-order rate constant [10].

Fitting the experimental data to this model allows us to extract Kapp, reflecting the speed of the degradation process. Figure III.19 shows the linear relationship between Ln (C_0/C_t) and irradiation time, validating the fit to the Langmuir-Hinshelwood model.

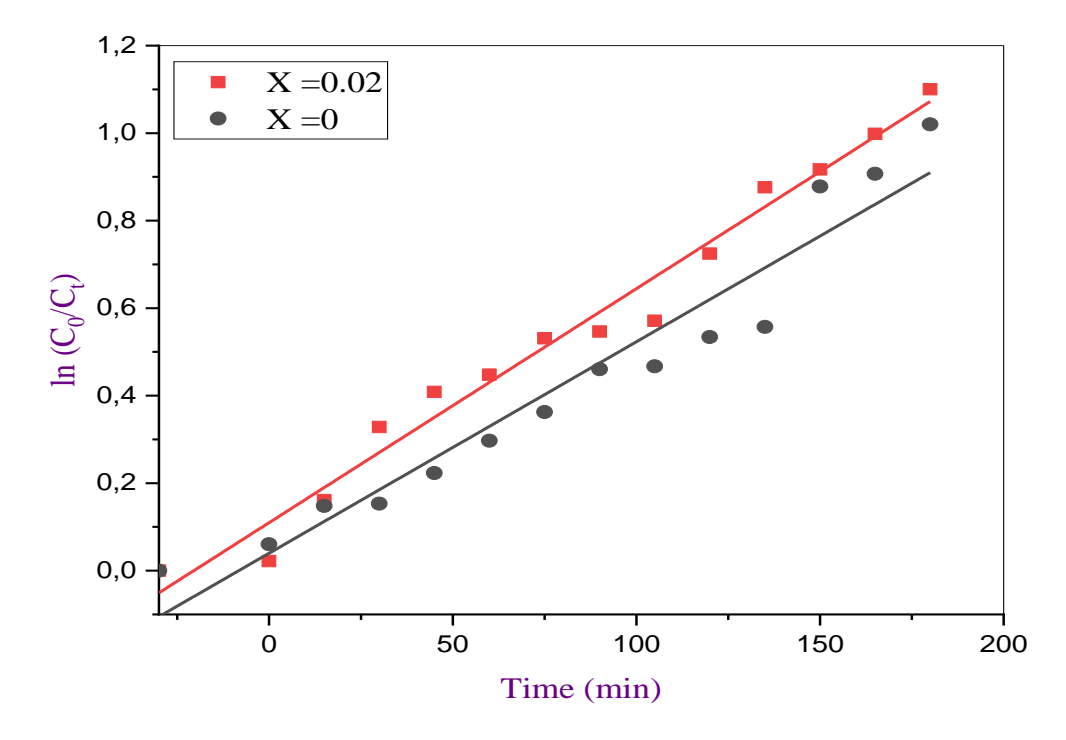


Figure III.19: Variation of ln(C₀/C) as a function of time for the degradation of methylene blue dye in the presence of BNT-X=0 and BNT-X=0.02 photocatalyst



The plot of Ln (C₀/Ct) versus time, presented in Figure III.19, reveals a quasi-linear relationship for all the catalysts studied. The high R² regression coefficients, greater than 0.92, confirm that the degradation kinetics of methylene blue follow a pseudo-first-order mode [8]. The apparent rate constants (Kapp), determined from the slope of the straight lines obtained, are reported in Table III.15.

Table III.15: Rate constants (K_{app}) estimated from the Langmuir model and linear regression coefficients (R^2) for BM degradation by the different photocatalysts.

	Photocatalytic degradation kinetics	
Samples	\mathbb{R}^2	K _{app} (min ⁻¹)
BNT-X=0	0,94	0,00483 ± 3,49581E-4
BNT-X=0.02	0,97	0,00535 ± 2,2872E-4

These results suggest that the BNT-X=0.02 catalyst exhibits superior reactivity, confirming its promising performance for the degradation of organic dyes and its relevance in water treatment applications.

III.6. Conclusion

In this chapter we have presented all the characterisations carried out:

- Ceramic morphology
- ♣ DRX method (geometric addition analysis)
- Photocatalysis

The crystal structure of BNT, validated by X-ray diffraction (XRD) studies, is rhombohedral. In addition, analysis of the microstructure of each sample using a scanning electron microscope (SEM) validated the presence of the desired elements in each composition. Above all, these in-depth studies are necessary to understand the intrinsic properties of materials and to assess their ability to act as photocatalysts. The results obtained are effectively the basis for research into making them more effective for use in photocatalysis, while also considering their use in the environmental pollution elimination and green energy generation sectors.





- [1] **Ksouri. A.** Synthèse et caractérisation d'un nouveau matériau de céramique de type Zirconat-Titanate de plomb (PZT), thèse de doctorat, univ Mohamed Khider Biskra-Algérie. (2024).
- [2] Abdelli. R.K. Synthèse et caractérisation d'un matériau de la structure pérovskites à base plomb, mémoire de master, univ Mohamed Khider-Biskra- Algérie. (2018).
- [3] Meklid. A. Elaboration, caractérisation et étude des propriétés diélectriques et électromécaniques d'un nouveau matériau de céramique de type Zirconate-Titanate de plomb (PZT), thèse de doctorat, univ Mohamed Khider-Biskra-Algérie. (2018).
- **Kharief. A.** Synthèse, caractérisations et étude structural des céramiques PZT de type pérovskite Pb_{1-x}La_zCa_x [(Zr_Y; Ti_{1-Y}) _{0.75}(Sb) _{0.25}] O₃, mémoire de magistère, univ de Constantine- Algérie. (2012).
- [5] Mendez-González. Y et al. Structural and microstructural features of lead-free BNT–BT thin films: Nanoscale electromechanical response analysis. *Journal of the American Ceramic Society*, 104(7), 3665-3681. (2021).
- Menasra. H et al. Structural and electrical characterization of La³⁺ substituted PMS-PZT (Zr/Ti: 60/40) ceramics. *Journal of Materials Science Poland*, 36(1), 1-6. (2018).
- [7] Wang. Q et al. Photocatalytic activity of hydrogen production from water over TiO₂ with different crystal structures. *Journal of Materials Science in Semiconductor Processing*, 40, 418-423. (2015).
- **Achour. A.** Élaboration et étude des propriétés structurales et photo catalytiques d'oxydes mixtes dérivés de pérovskites d'ortho ferrite de Lanthane (LFO) : La_{1-x}A_xFe_{1-y}B_yO₃, thèse de doctorat, univ Mohamed Khider-Biskra- Algérie. (2025).
- [9] Rahal. R et al. Synthesis of novel Bi_{0.5} Na_{0.5}Ti_{0.95} (Ni_{0.2}Fe_{0.2} Sb_{0.6}) _{0.05} O₃ perovskite material used as a photocatalyst for methylene blue degradation under sunlight



Chapitre III Experimental results and interpretation

- irradiation. Journal of Reaction Kinetics, Mechanisms and Catalysis, 137(4), 2377-2393. (2024).
- [10] Achour. A et al. Synthesis and characterization of mixed oxides derived from lanthanum orthoferrite perovskite: exploring morphological, spectroscopic, and photocatalytic properties. *Journal of Coordination Chemistry*, 77(5-6), 501-515. (2024).

General Conclusion



General Conclusion

This research focused on the development and characterisation of heterojunction photocatalysts, comprising the materials: $(Na_{0.5} Bi_{0.5})_{1-x} Sm_x (Ti_{0.8} Zr_{0.2})_{0.9}$ (Fe _{1/5} Zn_{1/5} In_{3/5})_{0.1} doped with samarium (Sm) in the A sites, where x takes different values.

Each material was precisely synthesised using the molten salt method and heat-treated at 900 °C to optimise its photocatalytic properties.

X-ray diffraction (XRD) analyses confirmed the tetragonal crystal structures of the materials with pyrochlores. This structural characterisation was complemented by observation of the morphologies using a scanning electron microscope (SEM), which validated the presence of the desired elements in each composition.

These structural and morphological properties directly influence the optical properties of the materials, as shown by the UV-Vis absorption measurements. These measurements revealed that all the materials act as semiconductors with bandgap energies well suited to activation under visible light. In particular, the band gaps for BNT X=0%, and BNT X=2% were 2.22 eV and 2.14 eV respectively. Sm³⁺ doping at the A site resulted in a reduction in these energies, suggesting an improvement in photocatalytic performance.

These results illustrate how Sm doping modifies the optical characteristics of the BNT matrix. In addition, the photocatalytic activity of BNT heterojunctions doped with 2% Sm was assessed by photodegradation of methylene blue dye (MB), revealing complex interactions between the components. The underlying mechanisms of photocatalysis were clarified through this study.

Photocatalytic tests showed remarkable efficiency in the degradation of organic pollutants under solar irradiation, underlining the potential of these materials for environmental applications. For example, BNT X=0 achieved a degradation rate of 58.25% for MB and BNT X=2% achieved 63.44%. The introduction of Sm³⁺ at the A site therefore resulted in better exploitation of visible light and a significant improvement in photocatalytic performance.

The photocatalytic mechanisms involved were mainly attributed to the activity of oxygen radicals (O2*-) and photo-generated holes (h⁺), facilitating the transformation of pollutants into less harmful compounds. This interpretation was reinforced by the hypsochromic shift observed in the absorption spectrum of MB after treatment, indicating a degradation of the dye.

General Conclusion

Taken together, these results open up encouraging prospects for the application of these substances in wastewater treatment. To further improve their effectiveness and applicability, it will be beneficial to continue optimising these materials and exploring their integration into more photocatalytic systems.

République Algérienne Démocratique et Populaire Ministère de l'Enseignement Supérieur et de la Recherche Scientifique Université Med Khider Biskra



الجمهورية الجزائرية الديموقراطية الشعبية وزارة التعليم العالى و البحث العلمي جامعة محمد خيضر بسكرة

كلية العلوم النقيقة

قسم علوم المادة شعبة الكيمياء



Faculté des Sciences Exactes Département des Sciences de la Matière

Filière de Chimie

تصريح شرفي

خاص بالالتزام بقواعد النزاهة العلمية لإنجاز بحث

(ملحق القرار 1082 المؤرخ في 2021/12/27)

أنا الممضي أسفله،
السيد(ة):
السيد(ة): السيد(ة): المستوحاني المستوحاني المستوحاني المستوحاني المستوحاني المستوحاني المستوكات
2024 - 80 الحامل(ة) لبطاقة التعريف الوطنية رقم:2 4 . $5.6.2$. الصادرة بتاريخ:2 9
المسجل بكلية: العلوم الد في في قسم: علوم الحدة
بانجاز أعمال بحث : مذكرة ماستر في الكيمياء
Influence of Sopina on the structural : isilisis
Influence of Soping on the structural : biloic Properties of a BAIT-type ceramics
أصرح بشرفي أني ألترزم بمراعات المعايير العلمية والمنهجية ومعايير الأخلاقيات المهنية والنزاهة الاكاديمية المطلوبة في انجاز البحث المذكور أعلاه وفق ما ينص عليه القرار رقم 1082 المؤرخ في 2021/12/27 المحدد للقواعد المتعلقة بالوقاية من السرقة العلمية ومكافحتها.

التاريخ: 3.6 3.6